Friedrich-Alexander University Erlangen-Nuremberg
Faculty of Engineering
M.Sc. International Production Management and Engineering (IP)
Specialization in Photonic Technologies

Master's Thesis

"Feasibility study on the automatic detection of faults in photovoltaic plants with unmanned aerial vehicles using low resolution thermographic cameras"

M.Sc. cand.
Vladimir Harwardt

September 21, 2020

Written at the Bayerisches Laserzentrum gemeinnützige Forschungsgesellschaft mbH (blz)
In collaboration with the German Aerospace Center (DLR)

Reviewer:	Prof. Dr.-Ing. Michael Schmidt (blz)
Second reviewer:	M.Sc. Kerstin Schaumberger (blz)

Advisor of issuing firm:	Dipl.-Ing. Niels Algner (DLR)
Advisor of issuing firm:	Dr.-Ing. Christoph Prahl (DLR)
Advisor at university:	Prof. Dr.-Ing. Michael Schmidt
	M.Sc. Kerstin Schaumberger
Employer:	DLR

Non-disclosure Notice

This master's thesis contains confidential data of DLR e. V. This work may only be made available to the first and second reviewers and authorized members of the board of examiners. Any publication and duplication of this master's thesis – even in part – is prohibited. An inspection of this work by third parties requires the expressed permission of the author and DLR e. V.

Die vorliegende Masterarbeit beinhaltet interne und vertrauliche Informationen der DLR e. V. Einsicht gestattet ist nur dem Erst- und Zweitgutachter sowie den berechtigten Mitgliedern des Prüfungsausschusses. Eine Vervielfältigung und Veröffentlichung der Masterarbeit ist auch auszugsweise nicht erlaubt. Die Weitergabe des Inhalts der Arbeit im Gesamten oder in Teilen sowie das Anfertigen von Kopien oder Abschriften – auch in digitaler Form – sind grundsätzlich untersagt. Ausnahmen bedürfen der ausdrücklichen Genehmigung des Verfassers und der DLR e. V.

Bayreuth, September 21, 2020

Vladimir Harwardt

Statutory Declaration

I hereby declare that the thesis submitted is my own unaided work. All direct or indirect sources used are acknowledged as references.
I am aware that the thesis in digital form can be examined for the use of unauthorized aid and in order to determine whether the thesis as a whole or parts incorporated in it may be deemed as plagiarism. For the comparison of my work with existing sources I agree that it shall be entered in a database where it shall also remain after examination, to enable comparison with future theses submitted. Further rights of reproduction and usage, however, are not granted here.
This thesis was not previously presented to another examination board and has not been published.

Ich erkläre hiermit ehrenwörtlich, dass ich die vorliegende Arbeit selbstständig angefertigt habe. Die aus fremden Quellen direkt und indirekt übernommenen Gedanken sind als solche kenntlich gemacht.
Ich weiß, dass die Arbeit in digitalisierter Form daraufhin überprüft werden kann, ob unerlaubte Hilfsmittel verwendet wurden und ob es sich – insgesamt oder in Teilen – um ein Plagiat handelt. Zum Vergleich meiner Arbeit mit existierenden Quellen darf sie in eine Datenbank eingestellt werden und nach der Überprüfung zum Vergleich mit künftig eingehenden Arbeiten dort verbleiben. Weitere Vervielfältigungs- und Verwertungsrechte werden dadurch nicht eingeräumt.
Die Arbeit wurde weder einer anderen Prüfungsbehörde vorgelegt noch veröffentlicht.

Bayreuth, September 21, 2020

Vladimir Harwardt

Vorwort

Die vorliegende Arbeit über automatische Fehlerdetektion von PV Anlagen, beschäftigt sich mit der Implementierung eines Prozesses, welcher es ermöglicht, Fehler in PV Anlagen durch den Einsatz von unbemannten Luftfahrzeugen, welche mit einer Thermografiekamera geringer Auflösung ausgestattet sind, zu detektieren. Die Thesis entstand während meiner Tätigkeit als Masterrand von Februar bis August 2020 bei DLR e. V. (Almería, Spanien) im Team QFly (Institut für Solarfoschung) und wird an der Fakultät für Maschinenbau an der FAU Erlangen eingereicht.

Das DLR entstand 1969 unter dem Namen Deutsche Forschungs- und Versuchsanstalt für Luft- und Raumfahrt (DFVLR) durch den Zusammenschluss mehrerer Einrichtungen: Neben der Aerodynamischen Versuchsanstalt waren dies die Deutsche Versuchsanstalt für Luftfahrt (DVL) und die Deutsche Forschungsanstalt für Luftfahrt (DFL) sowie 1972 die Gesellschaft für Weltraumforschung (GfW). Das DLR beschäftigt etwa 8.700 Mitarbeiter (Stand 2019) und besitzt an insgesamt 27 Standorten in Deutschland 40 verschiedene Institute und zahlreiche weitere Test- und Betriebseinrichtungen. Am Hauptstandort Köln sind etwa 1500 Mitarbeiter beschäftigt. Seit über 30 Jahren hat das Institut für Solarforschung neben seinen deutschen Standorten eine Niederlassung in Almería im Südosten Spaniens. Rund 25 Mitarbeiter arbeiten hier und haben Zugang zu den Testeinrichtungen der Plataforma Solar de Almería (PSA) des spanischen Zentrums für Energie, Umweltstudien und Technologie CIEMAT [1].

Die Anlage befindet sich am Rande der Wüste von Tabernas. Das dortige Klima bietet ideale Bedingungen für die Forschung und Entwicklung konzentrierender Solartechnologien. Die PSA ist das größte Forschungs-, Entwicklungs- und Testzentrum für konzentrierte Solartechnologie in Europa.

Danksagung

Ich bedanke mich recht herzlich bei

... Herrn Prof. Dr.-Ing. Michael Schmidt und Frau M.Sc. Kerstin Schaumberger von der Friedrich-Alexander-Universität Erlangen-Nürnberg (FAU), die mir ermöglicht haben, meine Abschlussarbeit beim Deutschen Zentrum für Luft- und Raumfahrt e.V. (DLR) in Almeria zu verfassen.

... Herrn Dipl.-Ing. Niels Algner (DLR) und Herrn Dr.-Ing. Christoph Prahl (DLR) für die fachliche und wissenschaftliche Betreuung.

... allen DLR-Mitarbeitern in Almería für die Unterstützung bezüglich organisatorischer und technischer Angelegenheiten, insbesondere bei Frau Anja Kruschinski und Herrn Lothar Keller sowie bei Herrn Wilko Jessen.

... meiner Familie und Freunden für das Verständnis und die Unterstützung während meiner Studienzeit.

... Michel Fischer für die technische Unterstützung bei allen Fragen bezüglich LaTeX.

Ein herzliches Vergelt's Gott!

Bayreuth, im September 2020
Vladimir Harwardt

Abstract

Due to the growing trend in renewable energy production, an ever increasing number of photovoltaic (PV) systems are being installed worldwide. To ensure their efficient operation, they must be inspected and maintained regularly. Since traditional inspection methods such as electrical tests are time-consuming and costly, new methods are being developed.

A promising inspection method is the so-called inspection by using unmanned aerial vehicles (UAVs) with dual camera systems (RGB and infrared). The inspection of PV modules using thermographic cameras has proven to be a suitable method for assessing the performance and condition of individual PV modules. The use of this technology offers a faster, autonomous and cost-effective inspection of large photovoltaic plants.

Although there is a trend towards higher resolutions and more expensive camera systems, this thesis aims to conduct a feasibility study for the automatic inspection of PV systems using low-cost, commercially available drones with lower camera resolution. The advantages are a high availability, easy handling, a flexible applicability and a huge price advantage compared to the expensive industrial drones.

The significantly lower camera resolution is a challenge in the detectability of defects by means of data accuracy. The aim of this study is thus to assess whether reliable statements about the quality and state of individual PV modules can be made employing thermography with low resolution camera systems. For this purpose, thermographic images are generated during the inspection process and subsequently verified by an automated algorithm.

For conducting this thesis the following is available:

- Dual camera system consumer drone (RGB and infrared)
- Photovoltaic test environment for data generation
- QFly postprocessing algorithm

Kurzzusammenfassung

Aufgrund der wachsenden Bedeutung erneuerbarer Energien wird weltweit eine immer größere Anzahl von Photovoltaik (PV)-Systemen installiert. Um ihren effizienten Betrieb zu gewährleisten, müssen sie regelmäßig inspiziert und gewartet werden. Da traditionelle Inspektionsmethoden wie elektrische Tests zeitaufwändig und kostspielig sind, werden neue Methoden entwickelt.

Eine vielversprechende Inspektionsmethode ist die so genannte Inspektion mittels unbemannter Luftfahrzeuge (Unmanned Aerial Vehicles, UAVs) mit Doppelkamerasystemen (RGB und Infrarot). Die Inspektion von PV-Modulen mit Thermografiekameras hat sich als geeignete Methode erwiesen, um die Leistung und den Zustand einzelner PV-Module zu beurteilen. Der Einsatz dieser Technologie bietet eine schnellere, autonome und kostengünstige Inspektion von großen PV-Anlagen.

Obwohl es eine Tendenz zu höheren Auflösungen und teureren Kamerasystemen gibt, soll in dieser Arbeit eine Machbarkeitsstudie für die automatische Inspektion von PV-Anlagen mit kostengünstigen, kommerziell erhältlichen Drohnen mit geringerer Kameraauflösung durchgeführt werden. Die Vorteile sind eine hohe Verfügbarkeit, einfache Handhabung, ein flexibler Einsatz und ein enormer Preisvorteil gegenüber den teuren Industriedrohnen.

Die deutlich geringere Kameraauflösung ist eine Herausforderung bei der Erkennung von Defekten hinsichtlich Datengenauigkeit. Ziel dieser Studie ist es daher zu beurteilen, ob mit niedrig auflösenden Thermografiekamerasystemen verlässliche Aussagen über die Qualität und den Zustand einzelner PV-Module gemacht werden können. Zu diesem Zweck werden während des Inspektionsprozesses thermografische Bilder erzeugt und anschließend durch einen automatisierten Algorithmus verarbeitet.

Für die Durchführung dieser Arbeit steht folgendes zur Verfügung:

- Zwei-Kamera-System Verbraucherdrohne (RGB und Infrarot)
- Photovoltaik-Testumgebung für die Datenerzeugung
- QFly-Nachbearbeitungsalgorithmus

Contents

List of Figures

List of Tables

Nomenclature

Abbreviations

Short	Description
2D	2-dimensional
3D	3-dimensional
CSP	Center for silicon photovoltaics
DEK	German Electrical Commission
EL	Electroluminescence
EOR	Exterior orientation: Camera positions obtained by photogrammetric evaluation [2]
FOV	Field of View
FPA	Focal Plane Array
fps	Frames per second
GPS	Global Positioning System
GSD	Ground sampling distance
IEC	International Electrotechnical Commission
IFOV	Instantaneous Field of View
IOR	interior orientation: Set of parameters describing the internal geometry and lens distortion of the camera [2]
IRT	Infrared thermography
NDT	Non-destructive technique
NETD	Noise-equivalent temperature
PID	Potential-induced degradation
PV	Photovoltaic
RMS	Root mean square
STC	Standard Test Conditions
UAV	Unmanned aerial vehicle
UV	Ultraviolet

Dimensionless Numbers

Abbr.	Description	Definition
X	2D geometric transformation X-coordinate	$a_0 + a_1 \cdot x - b_1 \cdot y$
Y	2D geometric transformation Y-coordinate	$b_0 + b_1 \cdot x - a_1 \cdot y$
μ	Mean Value	$\frac{1}{N} \sum_{i=1}^{N} A_i$
$\boldsymbol{M}_{DiffCheck}$	Check Difference Matrix	$\mathbf{A}_{\text{Calculated}} - \mathbf{B}_{ControlPoints}$
$\boldsymbol{R}$	Rotation matrix	$\begin{bmatrix} cos\,\alpha & sin\,\alpha \\ -sin\,\alpha & cos\,\alpha \end{bmatrix}$
RMS	Root mean square	$\sqrt{\frac{1}{n} \sum_{i=1}^{n} \left(X_{target} - X_{actual}\right)^2}$
$\boldsymbol{R}_{RMS}$	RMS Matrix of N_{vec}	$\frac{1}{N} \sum_{i=1}^{N} N_{vec_i}$

Greek Symbols

Symbol	Description	Dimensions	Units
α, β	Angle of view	–	°
Δs_{diff}	Synchronisation shift error	–	mm
Δt_{diff}	Synchronisation time error	–	s
η_{Module}	Efficiency	–	1
ε	Emissivity	–	–

Roman Symbols

Symbol	Description	Dimensions	Units
l	Length	–	m
A	Area of Module	–	m^2
d	Distance to measured object	–	mm
FF	Fill Factor	–	–
GSD	Ground sampling distance	–	$mm/pixel$
I	Intensity	–	1
I_{MPP}	Maximum Power Point Current	–	A
I_{SC}	Short circuit current	–	A
$IFOV(mm)$	Instantaneous Field of View/Spatial Resolution	–	mm
$IFOV$	Instantaneous Field of View/Spatial Resolution	–	mRad
I_{Ph}	Photocurrent	–	A
P_{OPT}	Optical power	–	kWp
P_{STC}	Supplied nominal electrical power	–	kWp
T	Temperature	–	$^{\circ}C$
U_{OC}	Open Circuit Voltage	–	V
U_{MPP}	Maximum Power Point Voltage	–	V

1 Introduction

1.1 Overview

Due to the growing trend in alternative energy production, an ever increasing number of photovoltaic (PV) systems are being installed worldwide.

IEA PVPS [3] reports that in 2019 an increase of 12 %, or approximately 115 GW of new installed PV capacity worldwide. The worldwide installed capacity is therefore above 620 GW, which represents about 3% of the total electricity generation worldwide.

China, USA, India and Japan represented the largest markets in 2019, with more than 50% of the additional installed capacity. China alone has around 30 GW of newly installed solar capacity in 2019.

For investors and PV plant operators, it is particularly important that the power generation of PV systems operates with maximal electrical output. Therefore it is necessary to inspect and maintain those regularly in order to maintain production at optimal level.

Since traditional inspection methods such as electrical tests are time-consuming and costly, new methods are being developed [4].

Especially advanced inspection based on optical methods becomes increasingly popular. A promising inspection method is the infrared thermography (IRT) imaging, which provides effective and powerful tools for the qualitative characterization of faults within a PV system and determine their exact position with high accuracy [4].

IRT is a non-destructive technique (NDT), which is used for quick and easy inspections of photovoltaic (PV) systems. IRT camera systems measure infrared radiation, which is emitted by the surface of any body, and its depiction, in the form of pseudocolor images of temperature distribution (i.e. thermal images) [5].

The majority of occurring faults on PV modules have a significant impact on the thermal behavior of the PV module. These lead to inhomogeneous temperature distribution on the surface of the defective PV module, which can be shown in the thermal image. Furthermore such thermal patterns can be used for quantitative diagnosis, by identifying the electrical power output losses of the impacted module, in the form of dissipated heat [4].

The IEA-PVPS [3] gives a detailed overview of specific failure modes of PV modules. Furthermore for well-known PV module failure modes, modelling approaches to forecast the power loss are summarized from the literature. In the rank order of impact, these failures are potential induced degradation, failure of bypass diodes, cell cracks, and discolouration of the encapsulant (or

pottant) material.

For a proper IR inspection, which determines the severity or significance of the detected findings, it is necessary to take into account various aspects, such as IR camera specification, environmental conditions including wind speed, irradiation and cloud coverage and the location of the equipment. Considering these aspects can lead to the reduction of measurement errors [6, 7, 8].

Especially the IRT investigation of larger plants using unmanned aerial vehicles (UAV) equipped with IRT cameras has become very common. Thus, larger areas can be inspected easily and comfortably from the air. Besides classical fault classification, aerial IRT inspection implements several additional challenges such as IRT mapping techniques and automated fault diagnostic algorithms.

Tsanakas et al. [4] give a detailed summary of the reported literature and research throughout the recent years, focusing on the classification of faults in operating c-Si PV modules and fault diagnosis by means of field IRT imaging and UAV-based IRT mapping of PV plants.

In summary, the following can be said, that the use of this technology offers a faster, autonomous and cost-effective inspection of large photovoltaic plants. At the same time there is an enormous need for research due to the complexity of this technology.

1.2 Problem definition and objectives

The main purpose of this thesis is to assess whether reliable statements about the quality and state of individual PV modules can be made employing UAV IRT inspection equipped with a low resolution IR camera. The significantly lower camera resolution is a challenge in the detectability of defects by means of data accuracy. The reason for this is that the quality of the measurement data, besides environmental influences and camera characteristics, also depends on the camera resolution [9].

There is a trend towards higher resolutions and more expensive IR camera systems [10]. However, this thesis aims to conduct a feasibility study for the automatic inspection of PV systems using low-cost, commercially available drones with lower IR camera resolution. The advantages are a high availability, easy handling, a flexible applicability and a huge price advantage compared to the expensive industrial IRT camera equipped UAVs.

The scope of this study is to introduce and test the UAV with low resolution IR camera system, obtaining a database of RGB and infrared videos. Relevant results are obtained through different defects. The systematic examination of the database can be used to implement an automated workflow, which enables the detection and the exact location of faults in larger PV systems.

The motivation for obtaining this knowledge lies in using cheaper consumer drones with low resolution cameras and thus fully exploiting the cost-effectiveness and efficiency of PV plant inspection.

Due to the fact that the inexpensive consumer drone has a low resolution, technical obstacles such as the lack of customer support from the drone manufacturer and the insufficient adjustment possibilities of the recording settings have to be compensated with self-developed software solutions, which were developed in the course of this work.

Some key points to analyze along the process of this thesis are:

- Using UAV-IRT-inspection during PV plant operation to test the reliability of detecting modules
- Implementing an automated workflow to post-process the raw data and localize individual modules geographically
- Analyzing the influence of low resolution and flight altitude
- Synchronizing IR and RGB raw data
- Transforming IR orthoimage to RGB orthoimage
- Adapting the QFly workflow to the new camera system

1.3 Thesis at a glance

This thesis is divided into 6 chapters.

- Chapter 1 explains the importance of IRT inspection method by using UAV with low resolution camera systems. This chapter also contains the main objective and an overall description of the various tasks to achieve the goal.
- Chapter 2 presents the most important terminology used in this work, as well as the basic principles of the construction of a PV system and its individual components. Also an overview of the most common and most frequently reported and investigated types of defects is introduced. Furthermore the effect of soiling is analyzed in separate subsection. In addition, defect detection using IRT in combination with UAV is described in detail. In the end of this chapter 2 the QFly software, developed internally by DLR, is presented.
- Chapter 3 represents the core-issue of this work. Here the challenges to be solved regarding automatic defect detection with low resolution IRT cameras are analyzed. Subsequently, the necessary steps are taken to solve them. These issues include the influence of low resolution, synchronisation of IR and RGB raw data, establishing a transformation matrix and considering the enviromental influences during IRT inspection with low resolution cameras.
- Chapter 4 presents the experimental setup and the used hardware, the basic experimental procedure. Furthermore two data sets are presented, one from the PV system and one for the calibration of the transformation matrix.
- Chapter 5 discusses the results and discussion of the challenges already presented in chapter 3. This chapter is divided into 4 sections. In the first section 5.1 the results concerning the flight altitude vs resolution are discussed. In the second part 5.2 the implementation

of the synchronisation timestamps is presented. In the third section 5.3 the results with respect to the implementation of the transformation matrix are presented. In the fourth and last part 5.4 the results concerning the automatic defect detection are shown.

- Chapter 6 summarizes the thesis by explaining how the objective is achieved, and the necessary steps taken to arrive at the goal. It also gives some recommendations for future research.

2 State of the art

In this chapter, the most important terminology used in this work is explained, as well as the basic principles of the construction of a PV system and its individual components.

2.1 PV systems basics

The term photovoltaic (PV) is composed of the Greek word phós, phōtós (light, of light), and the name of the Italian inventor of the electrochemical battery, Alessandro Volta (1745-1825). This term describes the direct conversion of sunlight into electrical energy [11].

The heart of every PV system is the solar cell (fig. 2.1) which consists of semiconductor material as the main component. The most common semiconductor systems in use today are based on silicon material. This technology is the basis of over 90% of the solar cells used today [12].

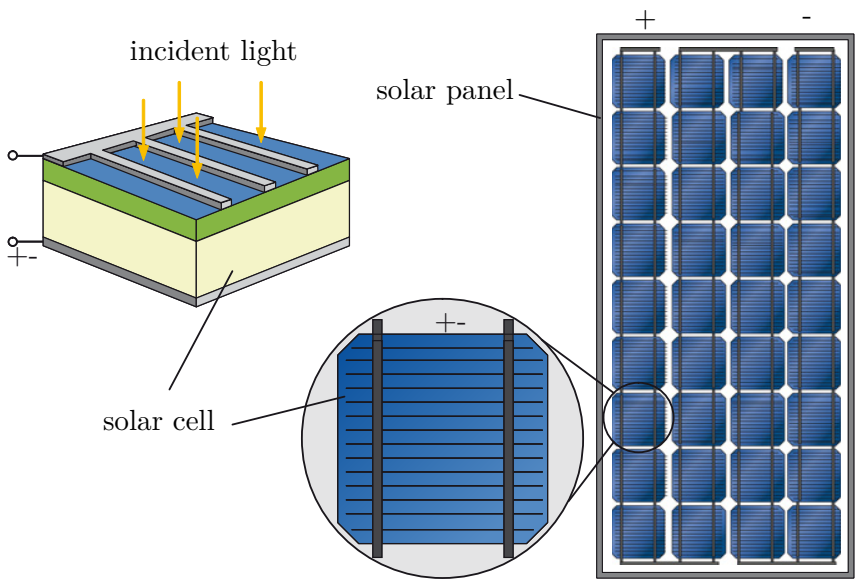

Figure 2.1: Solar cells and solar modules as basic components of photovoltaic systems [11]

To ensure that the positive and negative charge carriers are transported correctly, foreign atoms are added to the semiconductor, which creates a pn-junction. When photons in the form of light hit the solar cell, charge carriers are released from the crystal bonds and transported by the electric field to the external contacts. A voltage of approx. 0.5 Volt is generated. The current emitted depends on the irradiation and the cell area and is between 0 and 10 amperes.

To achieve higher voltages in the range of 20 to 50 volts, several cells are connected in series (cell

string) to form a complete module (fig. 2.1). Besides, the solar cells are sealed in the module to protect them mechanically and against environmental influences. The sealing usually consists of a glass front panel with very low absorption in the relevant spectral range between 380 and 1100 nm (solar glass quality) [13]. Another important component is the bypass diode. It is wired in parallel to individual solar cells to provide a current path around them in case a cell or panel becomes defective or is switched open.

If several solar modules are connected in series, this is called a string. In large PV systems, several strings can be connected to form a combiner using a combiner box.

For the operator of a solar power system, two characteristic values are of particular importance. The maximum power output of the system and the amount of energy that can be fed in over the whole year. The output of a solar module is measured under standard test conditions (STC) [14] and is stated in watt peak (Wp).

- Full solar radiation (irradiance $E = E_{\mathrm{STC}} = 1000\mathrm{W/m^2}$)
- Temperature of the solar module: $\vartheta_{\mathrm{Modul}} = 25^{\circ}\mathrm{C}$
- Standard light spectrum AM 1.5

This reflects the peak power of the module under optimal conditions. If the ratio of the supplied nominal electrical power P_{STC} is related to the incident optical power P_{OPT}, the efficiency η_{Module} of a solar module is obtained equ. (2.1).

$$\eta_{Module} = \frac{P_{STC}}{P_{OPT}} = \frac{P_{STC}}{E_{STC} \cdot A} \tag{2.1}$$

with A: Area of Module

The efficiency of silicon solar modules ranges from 15% to 22% depending on the crystal structure. In addition to silicon as a semiconductor material, cadmium telluride or copper indium selenide is also used. These are known as thin-film technologies and achieve an efficiency of 7% to 16%. The modules investigated in this thesis consist of silicon solar modules.

Thus the nominal capacity of a plant can be calculated as shown in equ. (2.2).

$$P_{STC} = P_{OPT} \cdot \eta_{Module} = 1000\frac{W}{m^2} \cdot 100m^2 \cdot 0.15 = 15kWp \tag{2.2}$$

With a specific yield w_{annual} of approx. 900 kWh/kWp (kilowatt-hours per kilowatt peak) per year the following annual yield W_{annual} results (equ. (2.3)).

$$W_{annual} = P_{STC} \cdot w_{annual} = 15kWp \cdot 900\frac{kWh}{kWp \cdot a} = 13.500kWh/a \tag{2.3}$$

2.1.1 I–V characteristic of PV cell

The solar cell can be analyzed using a simplified electrical circuit model with well-defined parameters (fig. 2.2). Using this model, a characteristic equation can be derived equ. (2.4). An ideal factor m was added to the exponent to better simulate the real solar cell curves. The ideality factor is typically in the range between 1 and 2 [11].

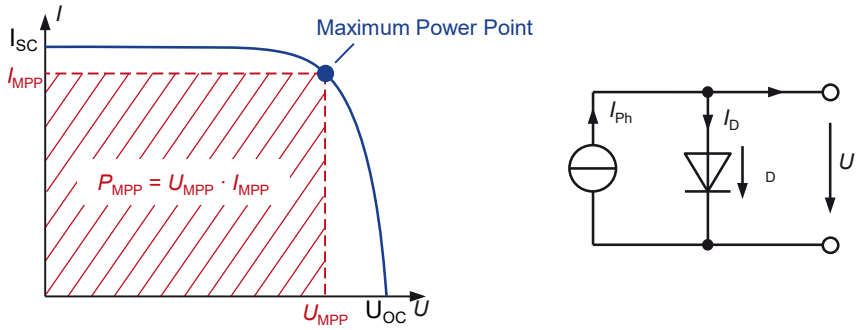

Figure 2.2: Solar cells characteristic curve (left) and simplified electrical circuit model (right) [11]

$$I = I_{Ph} - I_D = I_{Ph} - I_S \cdot \left(e^{\frac{U}{m \cdot U_T}} - 1 \right) \tag{2.4}$$

This diagram can be used to describe all the key parameters of a solar cell.

2.1.1.1 Short Circuit Current I_{SC}:

The short-circuit current I_{SC} of a solar cell is generated when the connections are short-circuited, i.e. the voltage U equals 0 Volt. Using equ. (2.4) results,

$$I_{SC} = I(U = 0) = I_{Ph} - I_S \cdot \left(e^0 - 1 \right) = I_{Ph} \tag{2.5}$$

that short circuit current I_{SC} is equal to photocurrent I_{Ph}.

Whereby the degree of the photocurrent I_{Ph} that can be achieved depends proportionally on the irradiance E, equ. (2.6).

$$I_{Ph} = const \cdot E \tag{2.6}$$

2.1.1.2 Open Circuit Voltage U_{OC}:

The second case occurs when the current becomes zero. To determine the open circuit voltage (U_{OC}), equ. (2.4) with, $I = 0$ and $I_{SC} = I_{Ph}$ is applied.

$$U_{OC} = U(I = 0) = m \cdot U_T \cdot ln\left(\frac{I_{SC}}{I_S} - 1\right) \tag{2.7}$$

The value 1 can already be neglected for very small disturbances, so that the result is simplified:

$$U_{OC} = m \cdot U_T \cdot ln\left(\frac{I_{SC}}{I_S}\right) \tag{2.8}$$

From the above it can be concluded that the dependency of the open-circuit voltage on the irradiance is significantly lower than that of the short-circuit current, it only changes with the natural logarithm of the irradiance E.

2.1.1.3 Maximum Power Point MPP:

The output power of a solar cell depends on the current operating point. The operating point at which the maximum power is delivered is called the Maximum Power Point (MPP).

MPP is calculated by multiplying the current and voltage values I_{MPP} and U_{MPP} with each other. In addition, fig. 2.3 shows the power curve $P = f(U)$, which reaches its maximum at MPP.

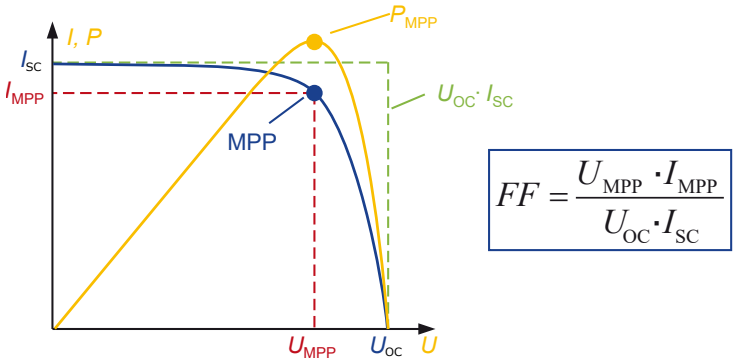

Figure 2.3: Solar cells characteristic curve with MPP (maximum power point) and FF. [11]

2.1.1.4 Fill Factor FF:

The Fill Factor FF describes the ratio between MPP power and the product of open-circuit voltage U_{SC} and short-circuit current I_{SC} and is a measure of the quality of a cell (fig. 2.3). The

value for silicon cells is between 0.75 and 0.85 and for thin-film materials between 0.6 and 0.75.

2.1.1.5 Efficiency η:

The efficiency of a solar cell indicates which part of the irradiated power P_{OPT} is emitted as electrical power P_{MPP}, equ. (2.9). The efficiency of silicon cells is between 15 and 22 %.

$$\eta = \frac{P_{MPP}}{P_{OPT}} = \frac{P_{MPP}}{E \cdot A} \tag{2.9}$$

with A: Area of cell

2.1.2 Series connection of cells

As already described in section 2.1, in practice several cells are connected in series to form a module to achieve significant performance.

The current I remains the same for a series connection, whereby the total voltage is the sum of the individual voltages. Figure 2.4 shows a module of 3 cells with the corresponding characteristics curve and the resulting total characteristic curve. The total characteristic curve is calculated by adding the individual voltages at constant current I_{SC}.

$$I = I_1 = I_2 = I_3 \tag{2.10}$$

$$U = U_1 + U_2 + U_3 \tag{2.11}$$

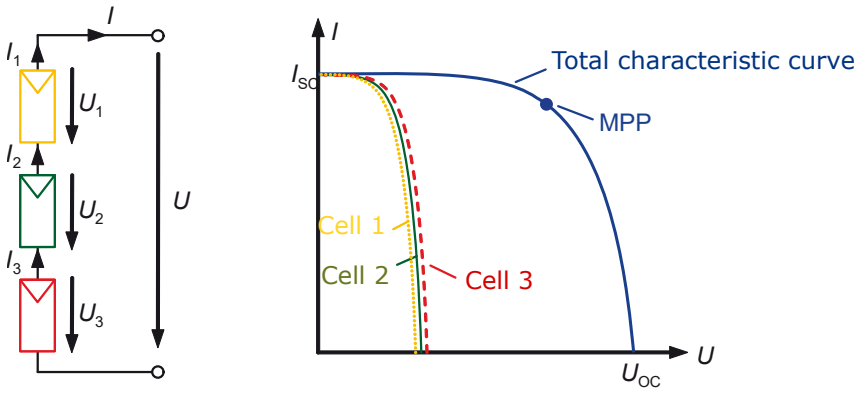

Figure 2.4: Series connection of solar cells: The voltages of the individual cells add up [11]

2.2 Hot-Spot Effect

Defects in PV systems can be detected by the use of thermography due to thermal heating of the affected area, this effect is also called the „Hot-Spot effect“ [15, 4].

The Hot-Spot effect occurs when the current produced in a cell is significantly lower than the string current in the module. This happens especially when the cell is completely or partially shaded, cracked or electrically mismatched [16].

Since the cell now produces a lower current, it is forced to pass a current higher than its generation. Therefore the cell becomes reversed biased, entering the breakdown regime, dissipating power, in the form of heat. This overheating of the cell leads to excessive efficiency degradation of the related photovoltaic module [17, 15].

The degree of degradation correlates directly with the heat dissipation under reverse bias. In the following fig. 2.5, the Hot-Spot effect is graphically displayed. A closer look at the graph on the left shows several cells connected in series, with cell Y hidden. The percentage of power lost in Y is equal to the module voltage and the reverse voltage generated in Y (fig. 2.5, right).

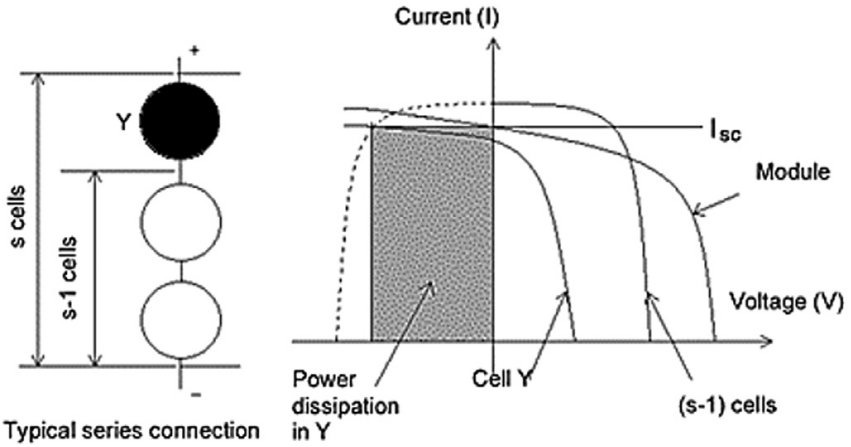

Figure 2.5: Hot-spot effect in a module of a series string: (a) typical series connection; (b) electrical power dissipation in the shaded cell [15].

Therefore using IRT enables one to indicate each discontinuity's signature based on the thermal pattern of an operating photovoltaic module.

The correct use of bypass diodes can prevent Hot-Spot damage from occurring.

The reversal characteristics of solar cells can either have a high shunt [1] resistance, whereby the reversal characteristics are voltage limited or have a low shunt resistance, where the reverse performance is current-limited. Depending on the type of affected cells each can be affected by hot-spot problems, but in different ways [19].

[1] Shunts refer to internal shortcircuits in solar cells made from multi-crystalline material, degrading the parameters of the cells and often even preventing their applicability [18].

In terms of low shunt resistance cells, the worst-case shadowing conditions occur when the whole cell (or a large fraction) is shadowed. One of the reasons for this phenomenon are localized shunts. In this case, Hot-Spot heating occurs because of a large amount of current flows in a small area. Because this is a localized phenomenon, there is a great deal of scattering in the performance of this type of cell. Cells with the lowest shunt resistance have a high likelihood of operating at excessively high temperatures at least in localized areas when being reversely biased. Because the heating is localized, Hot-Spot heating of low shunt resistance cells occurs quickly.

On the other hand, at high shunt resistance cells, the worst-case shadowing conditions occur when a small fraction of the cell is shadowed. The reason is that high shunt resistant cells limit the reverse current flow of the circuit and therefore heat up. The cell with the highest shunt resistance will have the highest power dissipation. Because the heating is uniform over the whole area of the cell, it can take a long time for the cell to heat to the point of causing damage [19].

2.3 Defects in PV power plants

This section provides an overview of the most common and most frequently reported and investigated types of defects, with a focus on the currently predominant technology of manufactured and installed/operating PV modules, the c-si wafers.

2.3.1 Defect vs. failure

In the literature, the terms „defect“ and „failure“ are defined differently. The definition of defect is very general and describes all possible characteristics that differ to a perfect PV module [20]. Therefore a defect can implement a PV module failure or not.

A PV module failure is rather specific and describes an effect that degrades the module power which is (1) not reversed by normal operation or creates a (2) safety issue [4]. A purely esthetic issue which does not have the consequences of (1) or (2) is not considered as a PV module failure. A defect that occurs due to environmental influences such as soiling of the module or due to lighting is not declared as a PV failure. The effect of soiling is analyzed in separate subsection 2.3.5.

The power generation of PV systems and the resulting payback period of investments in PV systems depend largely on the operational lifetime of the PV modules and their electrical output. This results in the strong need to reduce, isolate, and, if possible, eliminate each source of occurring or potential failure [21].

Already during installation and operation, there can be different types of anomalies in the PV system, which must be identified and avoided, as they can decrease the efficiency of the system.

Tasnakas et al. [4] summarizes all work related to the thermographic diagnosis of crystalline silicon photovoltaic modules and PV module defects and classifies them into three different

groups. Additionally he notes, defects that refer to purely esthetic issues or that are caused by the local environment are not considered as faults in this study, since they are not defined by considerable power output degradation and/or safety risk consequences.

- 1. Optical degradation: delamination and bubbles; discoloration of the encapsulant; glass (front cover) breakage.
- 2. Electrical mismatches and degradation: cell cracks/fracture and snail trails; broken interconnection ribbons; poor soldering; shunts and short-circuited cells; shading.
- 3. Non-classified Faults: PID; defective/short-circuited bypass diode; open-circuited sub-module.

2.3.2 Optical degradation

Optical degradation, such as bubbles, delamination (fig. 2.6,right) or glass breakage (fig. 2.6,left) are age-related and are mainly caused by environmental influences [4].

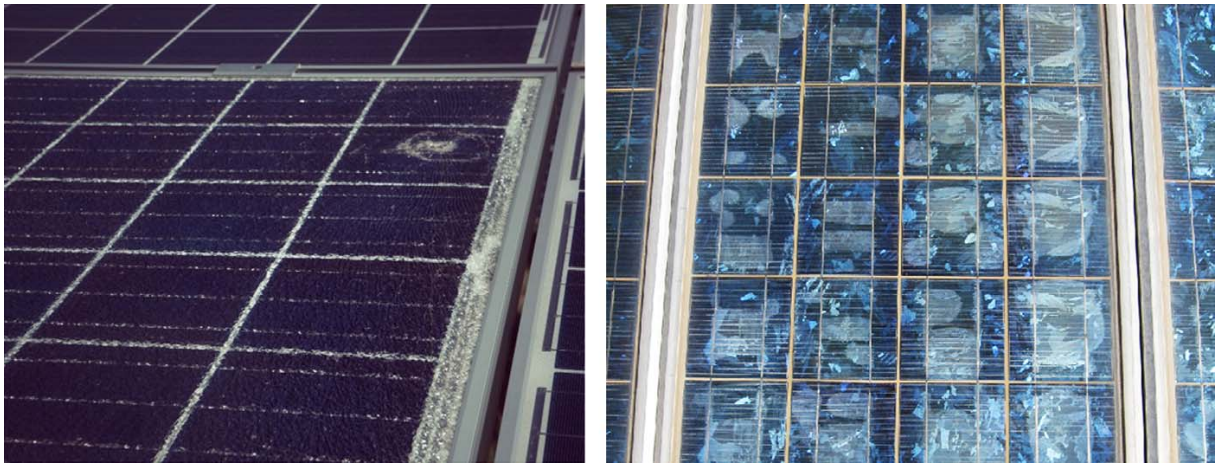

Figure 2.6: Optical degradation/failures in a PV module, in the form of glass breakage (left) and delamination (right). [4]

Djordjevic et al. [22] describes that such defects can be caused by internal or external factors. The internal factors include, for example, encapsulant quality or poor/incorrect lamination, and the external factors include high temperature or humidity.

This type of defect affects the optical properties of the module, which leads to increased reflections and reduced solar radiation on the PV module, which can lead to power loss if not resolved. By the application of optical/visual inspection, this type of defect can be detected [20].

Due to the reduced solar radiation, the short-circuit current I_{SC} drops and thus the output power (P_{max}) is reduced, fig. 2.7, left.

At the same time the reduced output voltage of the optically degraded modules leads to the so-called Hot-Spot effect, see subsection 2.2, (fig. 2.7, right). The temperature difference between the intact cells and the defective cells is $\Delta T < 5^{\circ}$C or higher [4].

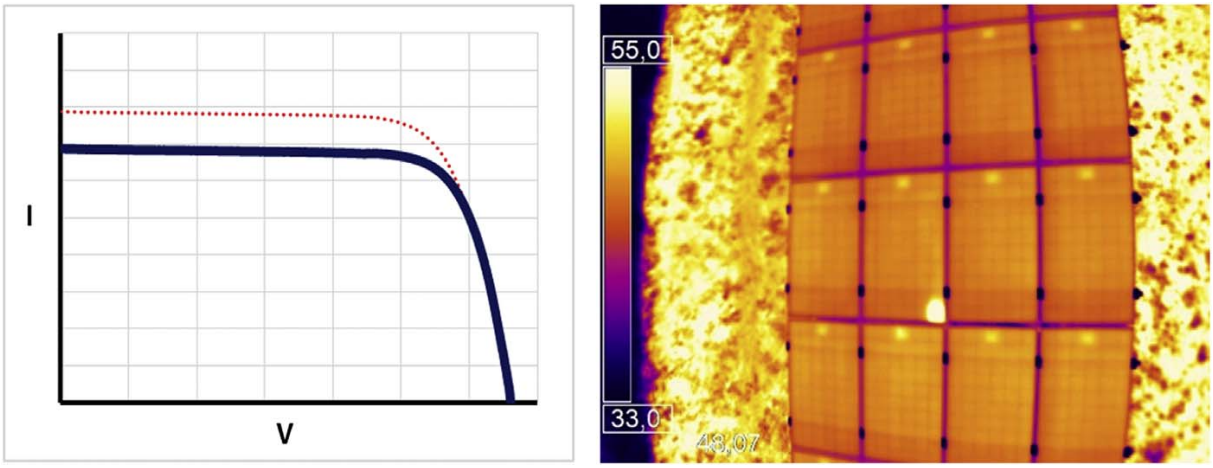

Figure 2.7: Typical I–V characteristic output (left) and thermal image (right) of a PV module with a defect. [4]

In [23], the history of degradation rates during the last 40 years has been summarized using field test reports. Nearly 2000 degradation rates, measured on individual modules or entire systems, have been assembled from the literature and show a mean degradation rate of 0.8%/year and a median value of 0.5%/year.

2.3.3 Electrical mismatches and degradation

The term „electrical mismatches“ can be associated with various faults. These include cell cracks, snail trails, broken interconnecting ribbons and busbars, shunts and poor soldering. These types of faults cannot always be found with a simple visual inspection, as is the case with optical degradation [4].

An „electrical mismatch“ is taking place when cells operating with different physical properties or operations under different conditions [24]. As a consequence cells do not operate at their individual power point but always under a combined maximum [25]. Mismatches in combination with a defective bypass diode may evolve Hot-Spots (fig. 2.11). This, in turn, can lead to browing, burnmarks or in the worst case, lead to fires [26, 25].

Cracks (s. fig. 2.8, left) are one of the most common defects in PV modules that differ in size, geometry, topology and orientation [26, 25]. The power loss due to cell cracks is highly dependent on the crack structure. This means that a crack in the cell does not necessarily lead to a power loss or an abnormal temperature distribution. However, smaller cracks can develop into larger cracks (propagates) due to environmental influences (thermomechanical stresses) [27]. These in turn can lead to isolation of the cracked parts and inactive cell areas and thus to power losses.

Discoloration effect (grey/black) of silver grid lines on the surface of crystalline silicon cells are often called snail trails (fig. 2.8, right). Snail traces usually occur at micro-cracks and/or along the cell edges [28]. Snail trails can easily be identified by vision. They typically occur three months to one year after the installation of the PV modules and spread depending on the environmental conditions [26]. Experimental tests showed a decrease in electrical PV power of

Figure 2.8: Cases of cell cracks (left) and consequent snail trails effect (right) in two different PV modules. [4]

more than 20% for modules affected by snail trails [29].

Experimental studies have shown that cracked PV modules can be identified by an I-V characteristic. This can lead to two different scenarios, either the I-V characteristic is stepped or has a significant drop in ISC (fig. 2.9). In both cases, there is a reduction in performance P_{max} and fill factor (FF).

In cases of cell cracks, thermal heating of the cracked cell, also known as a Hot-Spot may occur. The temperature increase ΔT depending on several factors, such as fracture topology and characteristic, the ambient conditions. etc.[21, 30].

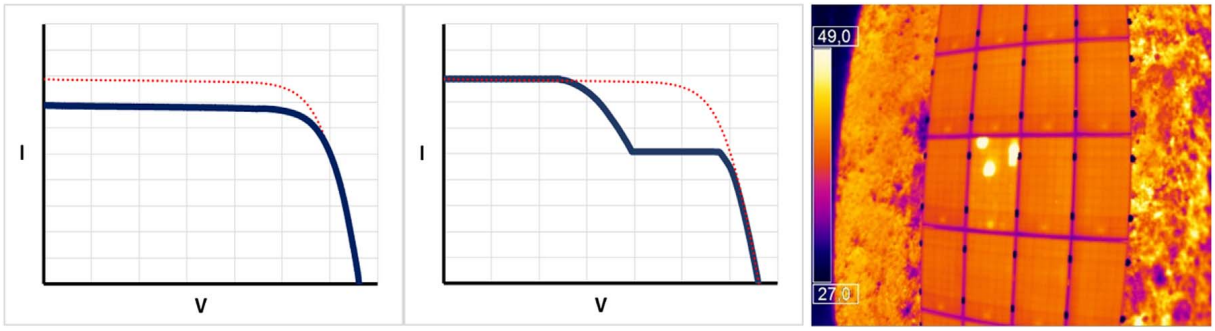

Figure 2.9: Typical I–V characteristic outputs (left/middle) and thermal image (right) of an electrically mismatched PV module, due to cell cracks/fracture [4]

.

Disconnected cells and broken or degraded string interconnect ribbons or busbars are typical for faults of the interconnecting materials in a cell or a string of cells and can be categorized as electrical mismatches (fig. 2.10). These types of faults can be caused by physical stress during transport or installation, thermomechanical stresses, poor soldering and/or hot spots, or long term operation of PV equipment [31, 32].

Electrically mismatched PV module, due to broken interconnection ribbons and defective sol-

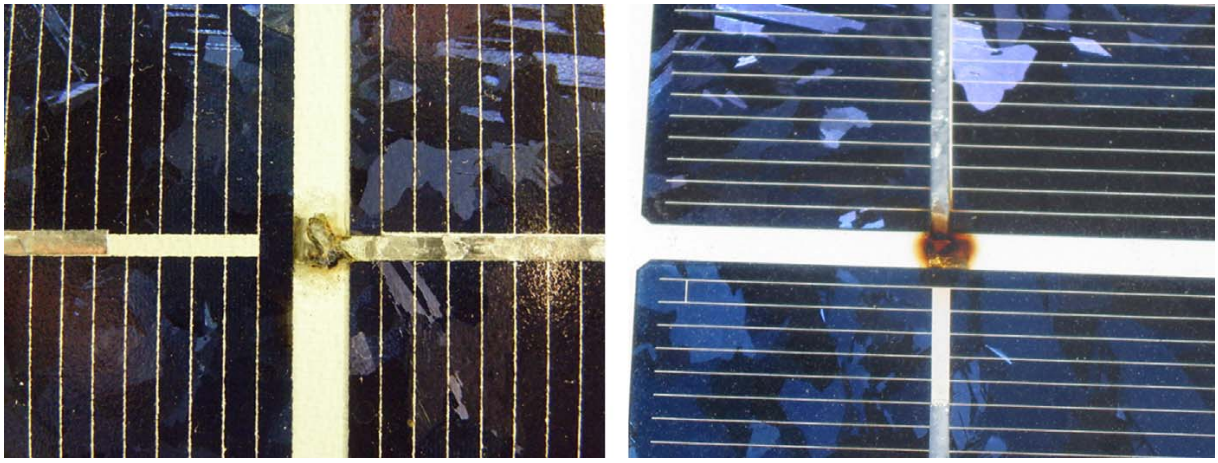

Figure 2.10: Cases of modules with degraded soldering and/or broken interconnecting ribbons (disconnected cells) [4]

.

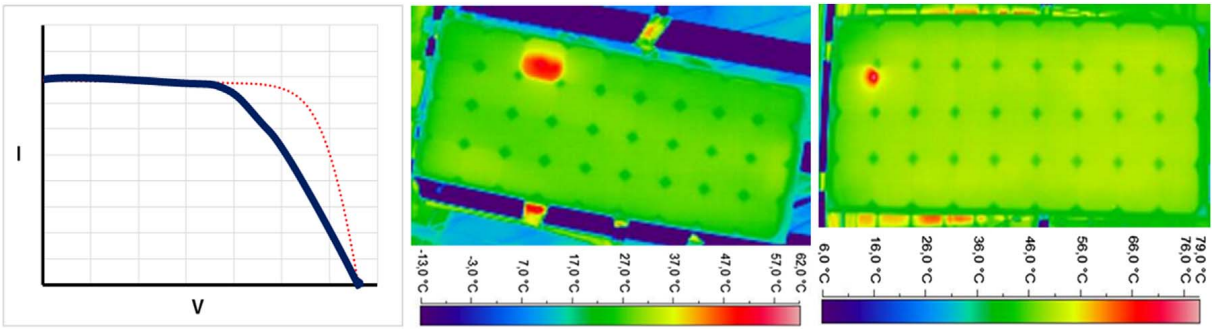

Figure 2.11: Typical I–V characteristic output (left) and thermal images of an electrically mismatched PV module, due to broken interconnection ribbons (middle) and defective soldering/busbar (right) [4]

.

dering/busbar can be identified by optical methods such as electroluminescence (EL) , infrared thermography (IRT) and ultraviolet (UV) imaging, as well as by I-V characterization, seefig. 2.11. For this type of error, two different cases can occur.

If only one of the two existing interconnections ribbons in a cell is separated, the cell appears as a heat source in the IR image or as a bright area in the EL image. In this case, the current flows through all strings and submodules of the defective PV module.

According to Buerhop et al. [33] for a specific cell type with two separate grids on the surface, a P_{max} loss of 6 W/cell, and a change of $\Delta\mathrm{FF} = -2.7\%/\mathrm{cell}$ resulting in a temperature increase of about $(12.5 \pm 3.6)^{\circ}\mathrm{C}$ was observed.

Depending on the resultant ΔT, even a single disconnection (one of the two ribbons) of a cell can result in a power loss of 35 % [34].

In this case, the security risk is not particularly high (severity stage 1) as long as the temperature of the resulting Hot-Spot does not exceed 100°C.

In the case that both ribbons of a cell are electrically disconnected, the current flow is interrupted

and goes through a bypass diode. As a result, the affected sub-module will no longer generate power. In this case, there is a power loss (severity stage 2) of up to 50% and the safety risk increases depending on the lifetime of the bypass diode. If the bypass diode fails, the final severity stage 3 may occur, where severe failure and extreme localized heating occur ($\Delta T > 500^{\circ}$C) at the disconnected part, with high safety risks (fire). The power loss of this kind of failure occurs stepwise [34].

In summary, it can be concluded that the above-mentioned types of faults, and in particular electrical mismatching, lead in their majority to hot-spot heating effects, which in turn worsen the electrical performance of the defective modules. As discussed in detail in section 2.3, hot spots that occur on operational PV modules can be effectively detected and quantified using IRT imaging [4].

2.3.4 Non-classified faults

These types of failures cannot be directly attributed to the I-V characteristic or a thermal pattern. This error type includes errors such as potential-induced degradation (PID) or defective (short-circuited) bypass diodes.

The PID effect is considered one of the most important degradation mechanisms in high-voltage photovoltaic (up to 1000V dc) PV systems. Laboratory tests at the Fraunhofer-Center for silicon photovoltaics (CSP) [35] have shown that more than 67% of PV modules tested are susceptible to PID effects. At the same time, the trend towards higher operating voltages of 1500V increases the PID risk.

In c-Si modules, PID can be considered as an irreversible polarization effect, for p- and n-type cells, at negative and positive potential respectively. PID effect particularly results in cell shunts and, thus, the degradation of V_{OC} and FF.

Although there are measures to prevent PID on the level of solar cell and module manufacturing as well as the design of the grounding scheme of the PV system, there are still new installations of PV systems affected by PID. The related solar modules can be identified in the PV system under operation using infrared thermography, provided that the weather conditions are appropriate [4].

Defective bypass diodes also belong to the category which has no direct influence on the performance of the PV module. The bypass diode is designed to minimize power loss due to shading. Additionally, the bypass diode protects against reverse biasing of solar cells higher than the allowed reverse bias voltage level [16].

It is very difficult to detect a defective bypass diode at an early stage, as it is only detected when a severe failure (e.g. disconnections, shading, crack, etc) occurs [4].

Depending on the number of defective/short-circuited or high-ohmic bypass diodes in a connected module, such a fault results in a typical thermal pattern where one or more cell rows, e.g.

sub-string(s) or submodule(s), are warmer (typically a temperature difference of $\Delta T = 3 - 5^{\circ}\mathrm{C}$) than other rows in the same module (fig. 2.12, right).

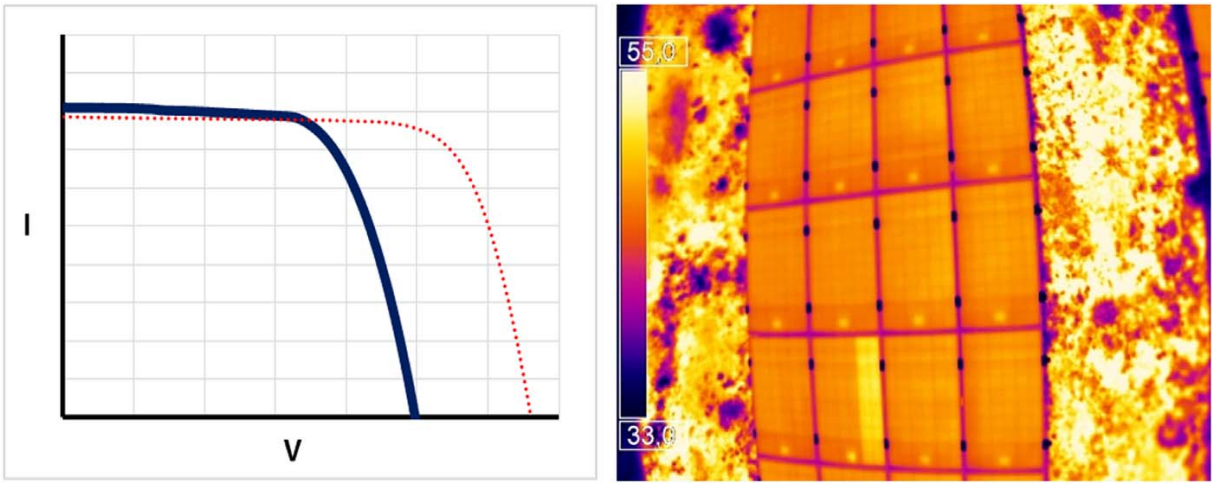

Figure 2.12: Typical I–V characteristic output (left) and thermal image (right) of a PV module with one inactive (open-circuited) submodule, due to a bypass diode failure [4].

On closer inspection of the I-V curve (fig. 2.12, left), a defective bypass diode in combination with of a failure (e.g. disconnections, shading, cracks, etc.) leads to a decreasing voltage V_{OC}, and thus to a lower power oput P_{max}. For example, if one of 3 bypass diodes in a module is defective, the result is a 33 % drop in V_{OC} and thus P_{max} [4].

2.3.5 Soiling

The term „soiling“ refers to the accumulation of dirt of the optical surfaces of solar energy conversion systems such as PV modules and solar mirrors. Soiling includes besides dust accumulation further surface contamination by plant products, soot, salt, bird droppings, and growth of organic species (fig. 2.13). Dust properties can be categorized in size and charge distribution, material composition, shape, surface energy, and biological properties [36, 37].

Soiling leads to yield loss due to the absorption and scattering losses of the incident light and can under certain circumstances lead to damage or complete failure of a PV module [37].

A significant number of studies have already been conducted on the subject of soling with regard to PV systems.

According to Mani et al. [39] deposition on solar collector surfaces depends upon two major factors: (1) location of the solar plants and (2) site's local environmental conditions (i.e. climate).

In the literature, an annual yield loss of 1-7 % in regions such as Spain, over 10% in arid zones such as Cyprus and Kuwait due to soling accumulation is reported [40]. Nevertheless, an accurate power loss prediction is difficult to make, as many correlated parameters have an influence, including environmental and weather conditions, tilt angle of the PV modules, the

Figure 2.13: Heavily soiled modules on the Gran Canaria Island. A manually cleaned module is visible at the top right corner. [38]

type of soiling agent, and also the texture of cells' front glass [41].

Furthermore, soiling can empower the effects of current mismatch due to uneven soiling regions of the PV module, this in turn leads to internal heating of the shaded solar cell (fig. 2.14). As an example, dust builds up on the bottom frame of the module and bird droppings cause uneven soiling on solar cells, which results in either partial or full shading on the cells [42].

As already mentioned in section 2.3.3, cell mismatch occurs when a shaded (or defective) cell in a substring underperforms and generates less current than the other cells in the substring. This forces the cell to operate in reverse bias, dissipating excess substring power as heat, thus limiting the substring's generated current and, in turn creating a current mismatch with other substrings operating normally (Crozier et al. 2015).

C. Schill et. al. [38] mentioned that a minor rainfall event can cause partial shading of the modules by the accumulation of dirt on the lower cell rows. The measured IV-curve fig. 2.15 shows a similar behavior as that for partial shading that is well-known from Hot-Spot investigations according to the module type approval test standard IEC 61215. Therefore he concludes that partial cleaning of soiled modules might face the same problems as partially shaded modules including the risk of Hot-Spots.

Consequently, contamination on the surface of the PV panel during the thermographic inspection can lead to a false positive by misidentifying this irregularity as electrical anomalies. One possible solution is pairing thermal cameras with RGB cameras in a drone sensor to provide both the required visible awareness and context to effectively and accurately spot anomalies in the field.

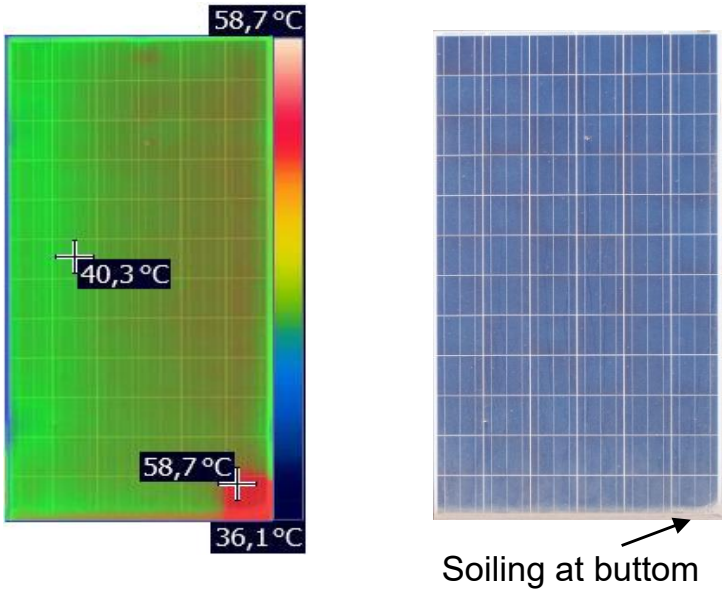

Figure 2.14: Thermal (a) and optical (b) images of a partially soiled module in string [42].

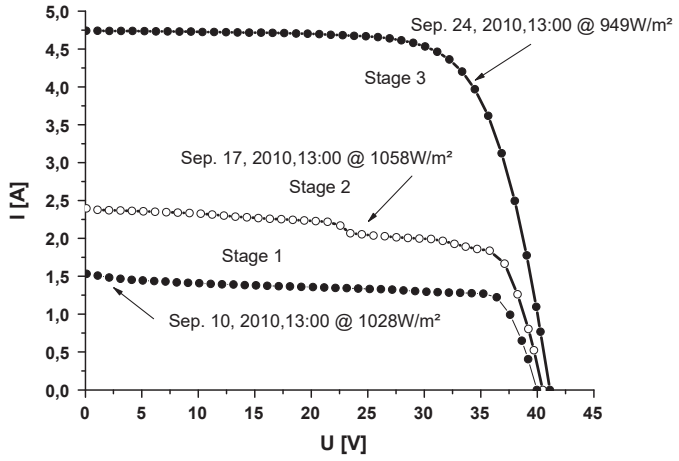

Figure 2.15: Typical IV curve showing effects of soiling (September 10), partial shading after a minor rainfall event (open circles, September 17) and removing of the soil (September 24) [38].

2.4 Defect detection using IRT in combination with UAV

2.4.1 Thermographic camera for PV inspection

The main component that has to be considered during a PV inspection is the thermographic camera (payload) and UAV (platform).

Using IR thermography has many advantages; such as noncontact, fast data acquisition, and large-scale use on PV plants at maximum power production state [43].

At the temperature higher than 0K (absolute temp) each body emits heat radiation in the form of electromagnetic waves. Emitted radiation, which spread with the speed of light is proportional to the body temperature [44].

Using a thermographic camera, the emitted heat radiation can be converted into an electrical signal using a detector and then displayed as a raster image (thermogram).

The most important component of a thermographic camera is the detector array. There are two types of detectors [45].

Thermal detectors based on heating by incident infrared radiation and photon (or quantum) detectors, where incident infrared radiation interacts on an atomic (molecular) level with the material of the detector, creating a voltage or electrical resistance.

A further classification of IR cameras into cooled and uncooled detectors is possible [44]. In uncooled thermography cameras, the sensor operates at ambient temperature whereas, in cooled detectors, the sensor is located in a vacuum-sealed housing, which prevents the detector from being affected by the ambient temperature.

The advantage is a higher thermal sensitivity (0.05K) of cooled camera systems compared to uncooled ones (0.01K).

Nevertheless, due to compact design and lower weight, uncooled thermography cameras are used for aerial thermography inspection [10].

The measurement can be performed in two ways. One is a quantitative one, in which exact temperatures are generated by the object (radiometric). In the second, the qualitative one, temperatures relative to the surrounding temperatures are compared (nonradiometric).

The camera version used in this work is a non-radiometric version from the company Flir Lepton 3.5. [46].

The IR measurement can be influenced by various factors, which can be divided into [47]:

1. Environmental Conditions
2. Hardware Considerations
3. Data accuracy

Environmental conditions such as humidity, wind, distance to the object of interest, air temper-

ature can affect the thermal sensor performance, and the accuracy of the temperature measurement. A detailed analysis regarding the distance to the object and environmental conditions is given in chapter 3.

The Hardware Considerations include the technical specifications of the camera and its calibration.

Defects can be identified by their shape and position of the thermal patterns, see subsection 2.4.2. For example, a whole module that appears warmer indicates that it is a short circuit.

One of the most important parameters of a thermographic camera is the resolution of the detector. The resolution requirements are determined by the size of the object to be inspected, distance to the camera, and the level of detail needed in the images, see section 3.1. Also, the price of the IR camera is strongly dependent on its resolution [10]

Another important parameter is the noise-equivalent temperature (NETD). Thermal sensitivity, or NETD, measures the smallest temperature difference that a thermal imaging camera can detect in the presence of electronic circuit noise. Cameras with a low NETD will detect smaller temperature differences and provide higher resolution images with increased accuracy. Thermal sensitivity is measured in milliKelvins (mK) [43].

In the case of a radiometric camera, the so-called camera accuracy is an important parameter. The reason is, that the minimum temperature difference (ΔT) between the faulty cell and the healthy area of a module is usually around 5° or higher. Therefore in terms of accuracy, it is important to understand that the accuracy of available commercial cameras is around $\pm\ 2^{\circ}$ or $\pm\ 5^{\circ}$, so the accuracy of this difference will be twice that of the accuracy of each single temperature point [10].

Furthermore, the framerate of the camera also has to be considered. The framerate is the rate at which the infrared detector creates images. Flight speed and framerate are strongly dependent on each other. High flight speeds with low framerates < 30Hz can lead to image blur and reduced quality of data.

An important aspect of the IR camera is its lens. The lens is essential to calculate FOV, IFOV, and IFOV Measurement, see section 3.1. Usually, lenses are not interchangeable and need to be specified.

In terms of data accuracy, a standard ground sampling distance (GSD) was determined by IEC standards [6], which is the benchmark for preparing flight operations. Comprehensive inspections require a 3 cm thermal GSD while a high-level overview can be done at a 15 cm thermal GSD tab. 2.1 [6].

The comprehensive level of aerial inspections is important because it provides the level of detail to support warranty issues. These include delamination, cracked modules and other anomalies that require very close examination of the modules [48].

Standard level aerial inspections are the most common choice globally for PV systems, providing

infrared thermal imagery at a 5-6 cm/px resolution. IT delivering an in-depth understanding of a site's current operating condition with less time compared to comprehensive inspection. The disadvantage is that no absolute temperatures can be measured [49].

Overview aerial thermography, as the most economical inspections, should be used to identify larger-scale anomalies (20 MW or more) with a significant impact on PV system performance. The main disadvantage of this inspection level is the limited image resolution and the limitation of identify module and sub-module level anomalies correctly [50].

Table 2.1: Overview of ground sampling distance

INSPECTION TYPE	OVERVIEW	STANDARD	COMPREHENSIVE
Description	Ideal for rapid drone flights and string-level outages	Ideal for annual preventative maintenance	Meets IEC TS 62446-3 thermography standards
Smallest visible features	Module	Diode, Hot-Spot, and Cell	Absolute Temperature Accuracy
Thermal ground sample distance (GSD)	15.0 ± 5.0 cm/pixel	5.5 ± 0.5 cm/pixel	3.0 ± 0.5 cm/pixel

In thermography, emissivity is the single most important attribute necessary for accurate thermal measurement. It's influenced by material, surface structure, geometry, angle, and temperature.

Emissivity represents a material's ability to emit thermal radiation and is an optical property of matter. It is the ratio of the amount of electromagnetic radiation emitted by an object to the amount emitted by an ideal blackbody at the same temperature. Solar panels tend to be highly reflective, which means a lower emissivity and an increased challenge in measuring highly accurate temperatures.

2.4.2 Defect identification using IR

Several studies have certainly proven that IRT is a cost-effective and efficient method for the fault diagnosis of PV modules [4]. The need of reliable measurements and accurate interpretation of

the inspected thermal signatures becomes increasingly important, especially when dealing with large-scale PV plants.

For that reason, in April 2018, the German Electrical Commission (DEK) published the pre-standard DIN IEC/TS 62446-3 [6].

There, the requirements for testing, documentation and maintenance and specific specifications for thermographic (infrared) testing of PV modules and solar systems in operation are mentioned. This type of testing is intended to improve preventive maintenance with regard to fire protection, the availability of the power generation system and the quality testing of PV modules.

A matrix for thermal abnormalities of PV modules is presented, see fig. 2.16 [4].

Fault Type	IR Thermal Pattern	I-V Pattern	Electrical degradation	Comments
○ Optical degradation	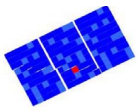	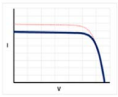	I_{sc} , I_{mpp} ↓ P_{out} ↓ (<0.5%/year)	o Generally slow degradation. o Total P_{out} losses limited up to ~5% for delamination and up to ~10% for severe discolouration, except for localized and very severe cases (that can lead to strong ΔT and other failures). o Stress factors: temperature, UV.
○ Cell cracks ○ Microcracks ○ Snail trails	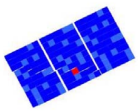	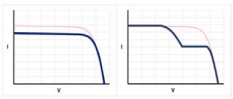	I_{sc} , I_{mpp} ↓ FF ↓ P_{out} ↓	o P_{out} loss ↔ number of cracks, ΔT, crack orientation / pattern o Inactive areas (due to cracks) >8% → severe, unacceptable P_{out} loss o > 50% → Bypass diode activation o Stress factors: thermal cycling, mechanical load.
○ Cell breakage – Missing material in cell matrix	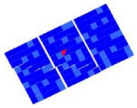	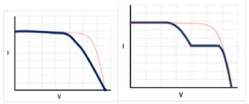	FF ↓ R_s ↑ P_{out} ↓	o Similar characteristics, between cell cracks and broken ribbons mechanisms o Increase of series resistance R_S o P_{out} loss ↔ size and topology of the inactive/missing area, ΔT o Stress factors: thermal cycling, mechanical load.
○ Potential induced degradation (PID)		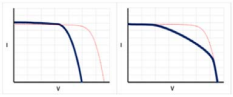	V_{oc} , V_{mpp} ↓ FF ↓ P_{out} ↓	o More severe at low irradiance than at STC o ΔT higher for medium degraded cells. than for severely degraded ones. o P_{out} loss up to 100% but majorly recoverable by applying reverse voltage o P_{out} loss ↔ module configuration o Stress factors: temperature, relative humidity, electrochemical
○ Short-circuited / Shunted cells ○ Shadowing	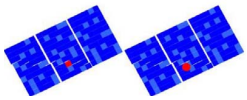	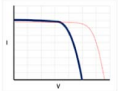	R_{sh} ↓ , R_s ↑ FF ↓ V_{oc} , V_{mpp} ↓ P_{out} ↓	o ΔT much lower than in other cases of faults. o At STC, the impact on current *I* is nearly negligible; the losses in voltage *V* and power *P* are more considerable o P_{out} loss ↔ number of shunts. o Shadowing not necessarily permanent o Stress factors: thermal cycling, mechanical load

Fault Type	IR Thermal Pattern	I-V Pattern	Electrical degradation	Comments
○ Broken interconnecting ribbon(s) ○ Faulty or displaced soldering	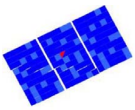	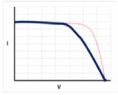	FF, P_{out} ↓	o Strong, even extreme, ΔT in a part or a whole cell, depending on the number of broken ribbons. o If all (usually two) ribbons fail at the same cell, the submodule goes off and current flows through a bypass diode → sever P_{out} loss (up to 30-50%) o Drastic P_{out} and FF loss per cell or broken ribbon. o Stress factors: thermal cycling, mechanical load
○ Substring open-circuited Defective bypass diode ○ Internal short-circuit	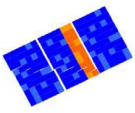	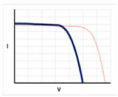	V_{oc} , V_{mpp} ↓ P_{out} ↓	o Usually moderate uniform ΔT across the faulty substring/submodule but drastic V and P losses. o If N the total number of the strings-bypass diodes of the module, and M the faulty ones, then the resultant power and voltage losses are (M/N)×100% o Stress factors: electrical
○ All bypass diodes short-circuited ○ Erroneous connection		Non-applicable (N/A)	V_{oc} , V_{mpp} ↓↓ P_{out} ↓↓↓	o "Patchwork" (non-specific) thermal pattern is indicative of a short-circuited module due to either failure/short-circuit in all bypass diodes or wrong connection of the module. o Drastic voltage and power losses, nearly 100%. No actual I-V characteristic obtainable. o Stress factors: electrical
○ Open-circuited module ○ Failed system connection	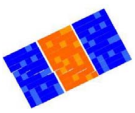	N/A	N/A	o The resultant ΔT is low-moderate and uniform for all the module surface. o The module is just open-circuited and normally fully operational. o Possible causes: bad open-circuited wiring between modules in the array or in the junction-box. o Failure in system scale.

Figure 2.16: Fault classification table in terms of IRT thermal and I–V pattern and impact of faults on the expected degradation of electrical performance of PV modules [4].

2.5 QFly Workflow

The QFly software, developed internally by DLR, is used for quality control of entire solar fields from the air. QFly provides information about the geometrical as well as the optical and thermal properties of the solar field by airborne image acquisition and the associated software [51, 52]. First developed for the quality inspection of parabolic trough solar fields, the software has now been adapted to perform quality inspection of PV solar fields.

Due to the new camera system and the new application, the adaptation of the software has several technology-specific challenges, which have to be overcome within the scope of this work.

In the following graphic the basic QFly workflow is presented fig. 2.17.

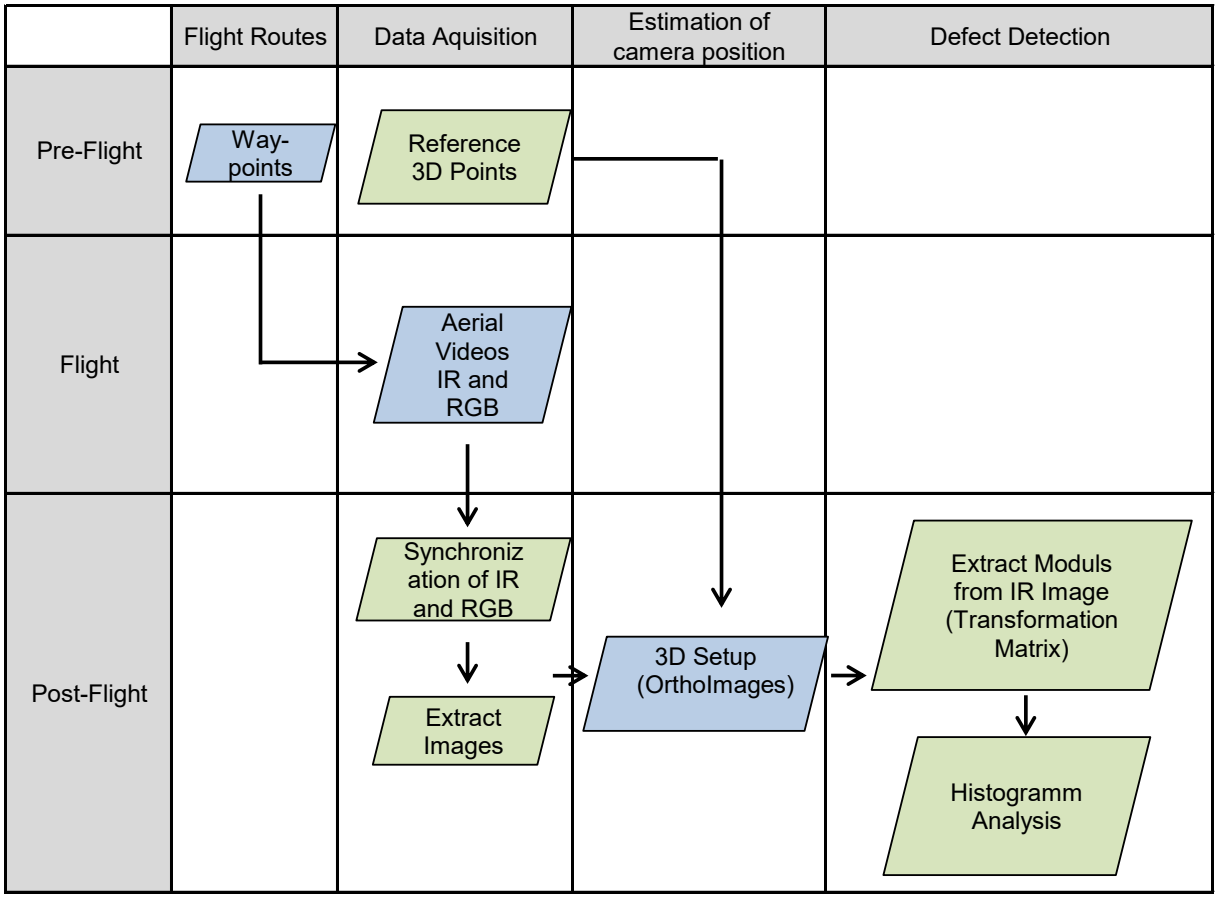

Figure 2.17: QFly Workflow on a vertical level consists of three steps: pre-flight, during the flight and post-flight. On a horizontal scale the process can be divided into determination of flight routes, data acquisition, estimation of camera position and defect detection

On a vertical level, the QFly PV process can be divided into the three process steps pre-flight, during the flight and post-flight. On the horizontal scale, the process is divided into the determination of flight routes, data acquisition, estimation of camera position, and defect detection.

In the very first step of the process, the flight routes must first be determined using waypoints. These can be generated manually with the supplied software from the drone manufacturer or automatically within the QFly software. In parallel, a 3D model of the investigated PV system has to be created, which is later necessary for the estimation of the camera position and the resulting orthoimages.

Once the above steps have been completed, the actual data acquisition can be initiated. Since the used drone is equipped with an dual-camera system (IR and RGB), both IR thermography and RGB videos are recorded. These recordings form the basis for further post-processing, which includes the automatic detection of defects in PV systems. In this process chain, the selected flight altitude, flight speed, and environmental conditions play a significant part since these influences determine the quality of the raw data, Chapter 3.

In the third and last process step, which is the core of the QFly software, the main data evaluation takes place.

To evaluate the recorded IR and RGB videos in the further process, these must first be segmented into separate images and saved in a suitable format.

The format used in this workflow is the widely spread JPG [2] format. Since the IR camera and the RGB camera run at different frequency rates, they must be synchronized accordingly, so that the RGB and IR images match (see Chapter Timestep). In the same process step, information on the position and orientation of both cameras is stored for each image sequence.

In the following step, the orthoimages are created. Orthoimages or also called orthophotos are geometrically corrected raw images by considering topographic relief, lens distortion, and camera tilt [54].

Because of the low resolution and the poor visibility of features (corner points of the modules) in the IR images, the orthoimages are created by using the RGB images.

The spatial information of the 3D-setup (exterior orientation (EOR) relative to PV Module) is used, to calculate the 2D transformation from the raw image to the orthoimage.

In the first approximation, this is a projective transformation and in the second approximation a pixel-wise transformation considering lens distortion (Interior orientation (IOR)) and real features of the PV module.

The pixel-wise transformation is described by a look-up table assigning to every pixel in the raw image exactly one pixel in the target matrix (the orthoimage).

By using the pixel-wise transformation, each pixel in the orthoimage matrix can be assigned to a specific location in the ideal module geometry, defined by the horizontal distance from the vertex (X-axis), the position along the vertex (Y-axis), and the height (Z-axis) [52].

[2] JPG is the abbreviation of JPEG; reduced to three letters, as is usual for filename extensions. JPEG is an association of companies and research institutes that established this standard for storing digital images in 1992 [53]

Also, each identified module is noted with an ID tag. This is necessary so that in the further analysis process, each module on the image can be uniquely identified with the same module in the real PV system.

Once the individual modules in the image sequences have been identified, a transformation matrix can be used to superimpose the modules from the RGB onto the IR image. This step is characterized by its challenges, which are addressed accordingly in subchapter 3.2 and 3.3.

Finally, the identified modules can be analyzed for defects using a suitable algorithm.

3 Analysis of limitations

3.1 Influence of low resolution

This work aims to successfully detect defects in PV systems using low-cost consumer drones equipped with low-resolution IR camera systems. At this point, the effects of this approach on the process shall be determined.

One of the most important characteristics of a thermal camera is the resolution of the detector also known as Focal Plane Array (FPA). The resolution describes the number of pixels in the horizontal direction multiplied by the number of pixels in the vertical direction. Infrared camera systems available on the market vary from 80 x 60 pixels (4.8 kilopixels) up to 640 x 5120 pixels (0.327 megapixels), depending on the sensor size.

A high resolution allows the acquisition of smaller objects from a greater distance. In fig. 3.1 two different cameras with different resolutions are compared. On the left side of the figure an object was taken from a height of 30.5m with a resolution of 160 x 120 pixel and on the right side with a resolution of 640 x 510 pixel. Here it becomes clear that the picture on the right provides much more details than the left picture.

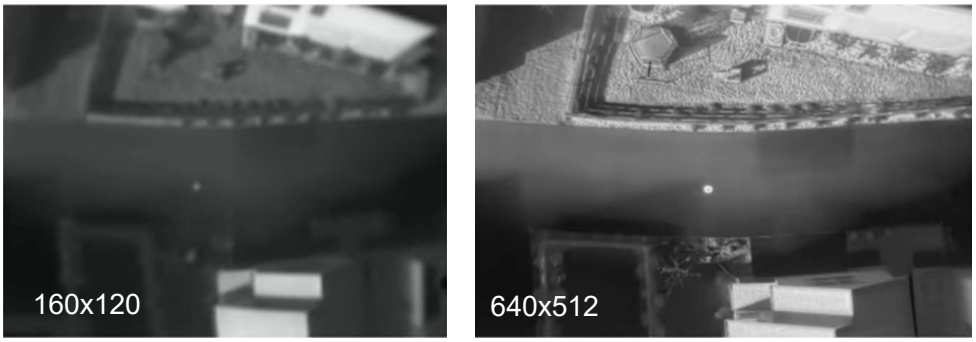

Figure 3.1: Compare 160 x 120 resolution of the FLIR Duo (left) and the 640 x 512 resolution of the Zenmuse XT (right) at 30.5 m height [55]

The resolution of the camera is directly related to the flight altitude, taking into account that the same lens is used. To calculate the necessary flight altitude it is important to know the size of the smallest object, which should be successfully identified. The lens, together with the altitude and the camera sensor, determine the size of the area that can display the image, also known as the Field of View (FOV). FOV is defined by 3 angles, horizontal, vertical, and diagonal, depending on the lens and the sensor used. Most of the camera manufacturers offer an online calculator to calculate FOV in dependence of the IR camera specifications [56, 57].

If the value for FOV is set, the field of view of a single detector element in the entire detector array of the camera must be calculated, see fig. 3.2.

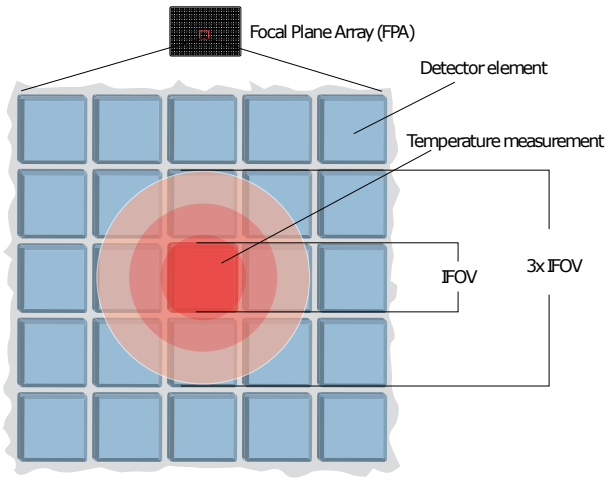

Figure 3.2: Detector Array with FPA, Detector element, Temperature measurment, IFOV and 3x IFOV [58]

Instantaneous Field of View (IFOV) or Spatial Resolution is the smallest detail in the FOV that is successfully detected or visible at a given distance. IFOV is typically measured in units called milliradians (mRad). Since the viewing angle of a single detector element is small, we can assume that the tangent of this angle is approximately equal to its value in radians, see equ. (3.1).

$$IFOV = \left(\frac{FOV}{number\ of\ pixels^{1}}\right) \times \frac{\pi \times 1.000}{180} \tag{3.1}$$

The IFOV measurement or measurement resolution is the smallest detail that can be measured to obtain an accurate temperature measurement at a certain distance, typically expressed in milliradians, which should be 3 to 5 times greater than the Spatial Resolution (IFOV) value.

The IR camera [2] used in this work has a resolution of 160×120 pixels and a FOV - horizontal of 57°. If these values are used in equ. (3.1), a spatial resolution of IFOV = 6.21 mRad is obtained. Considering the viewing angle of a single detector element is small, we can calculate IFOV in mm depending on the distance from the object, see equ. (3.2):

$$IFOV(mm) = \left(\frac{IFOV(rad)}{1.000}\right) \times D_{distance} \tag{3.2}$$

[1] Use the number of pixels that matches the (horizontal/vertical) orientation of your field of view (FOV)
[2] FLIR: Lepton 3.5, 160×120, 57° with shutter

In the following fig. 3.3 the value for IFOV (mm) is calculated for three different resolutions, taking formula (3.1) and (3.2) into account, depending on the object distance $D_{distance}$.

Assuming that the size of a solar cell is 180 mm x 180 mm, which represents the smallest detail in the FOV that should be successfully detected, the measurement resolution is 36 mm for the 3-fold and 60 mm for the 5-fold IFOV value, see equ. (3.3) and equ. (3.4).

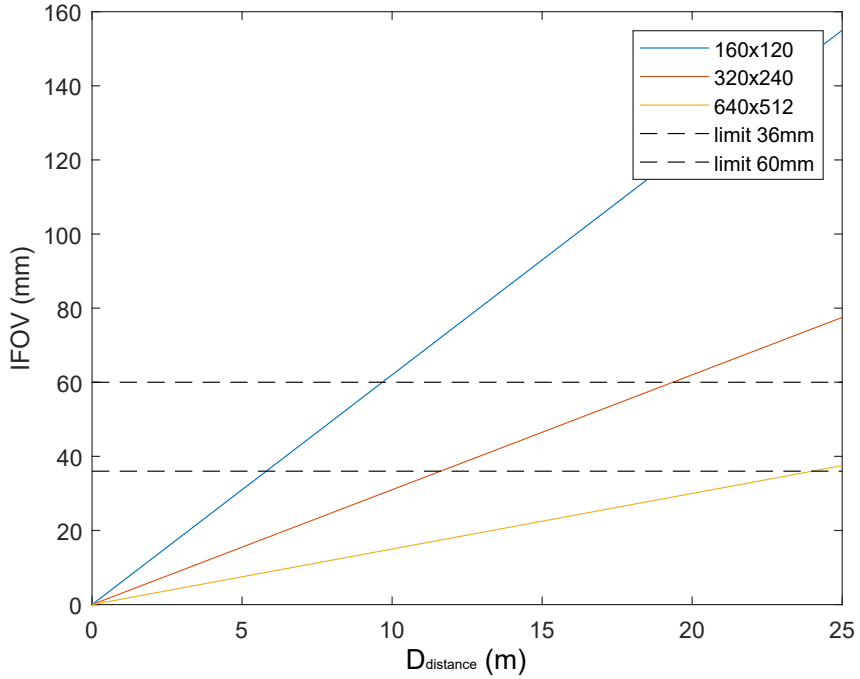

Figure 3.3: IFOV depend on flight height for 160 x 120, 320 x 240 and 640 x 512 pixel resolution; maximum object distance $D_{distance}$ for IFOV = 36 mm and 60 mm

$$IFOV_{max} = \frac{IFOV\,Measurement}{3} = \frac{180}{3} = 60\,mm \tag{3.3}$$

$$IFOV_{max} = \frac{IFOV\,Measurement}{5} = \frac{180}{5} = 36\,mm \tag{3.4}$$

From fig. 3.3 it is immediately clear that with increasing resolution the distance to the object increases while the IFOV value remains the same. Looking at the curve for the resolution of 160x120 pixels, a maximum distance to the object of about $D_{distance} = 6m$ is acceptable with a limit of $IFOV = 37mm$ and with a limit of about $IFOV = 60mm$ a maximum distance of $D_{distance} = 11m$.

This allows to derive following:

- A lower resolution leads to a lower flight altitude.
- A lower resolution influences the flight time since the FOV is smaller and therefore a smaller area is recorded.
- Flight altitude and resolution are linear dependent.

3.2 Synchronisation of IR and RGB raw data

As already mentioned in section 2.5, an important step of the QFly process is the processing of the raw video data into individual image sequences.

The frame rate of both cameras plays a key role in this step. The frame rate refers to the number of frames that are captured or replayed per time period and is usually expressed in frames per second (fps).

To achieve a perfect match from RGB to IR image, the basic requirement is that both images were taken at the same time. If the frame rates are different, synchronisation errors may occur. This problem is shown graphically in fig. 3.4. The RGB camera used in this work has a frame rate of 30 HZ and the IR camera 8.7 HZ.

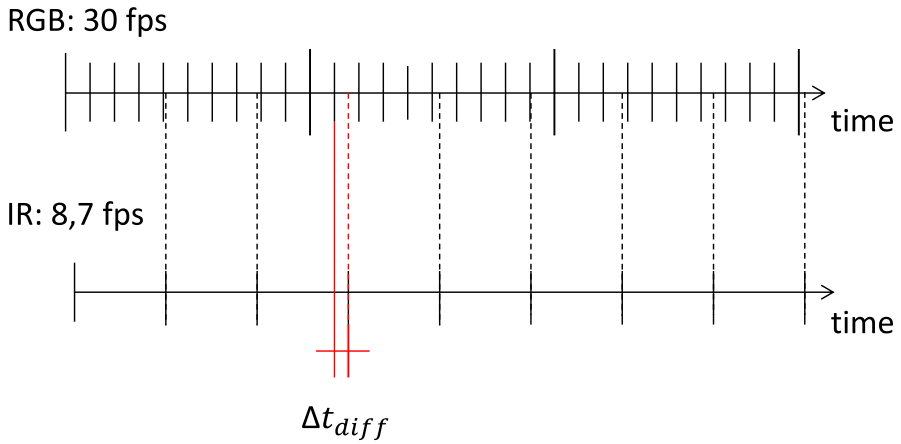

Figure 3.4: Compare two different framerates of IR with 8,7 fps and RGB with 30 fps camera and illustrating the resulting timedifference Δt_{diff} .

If the synchronisation does not fit, a synchronisation error Δt_{diff} occurs. This synchronisation error Δt_{diff} in turn leads to an shift Δs_{diff} in the imageplane, depending on the flight speed of the drone fig. 3.5, equ. (3.5).

$$\Delta s_{\text{diff}} = \Delta t_{\text{diff}} \cdot v_{\text{UAV}} \tag{3.5}$$

For this reason, Δt_{diff} must remain as minimal as possible so that a correct superimposition of

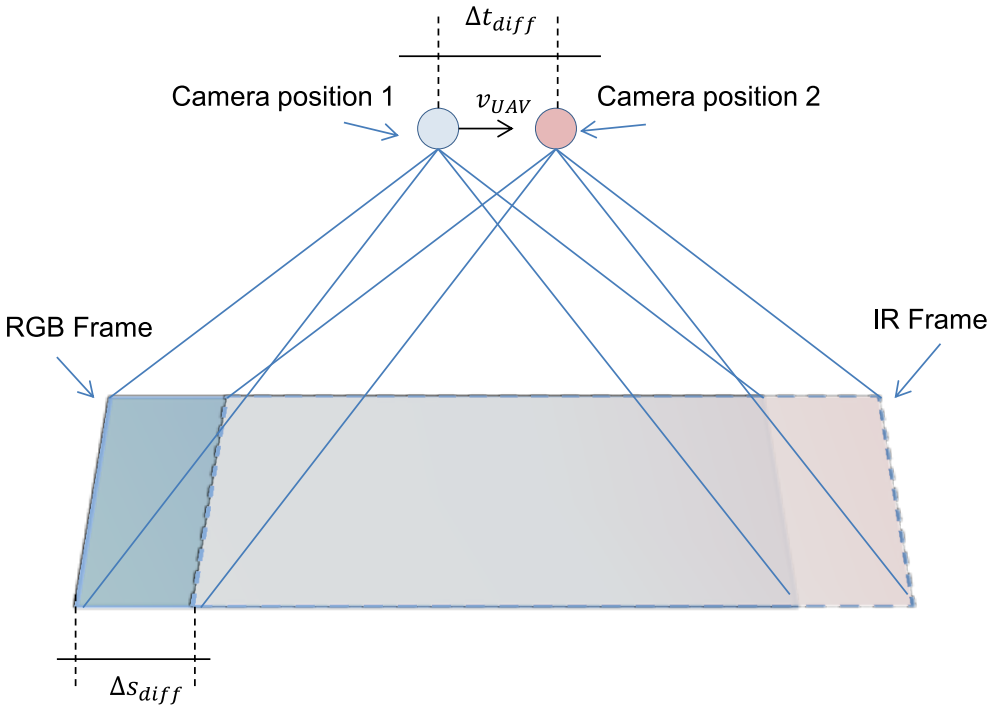

Figure 3.5: Dependency of Δt_{diff}, Δs_{diff} and flight speed of the drone v_{UAV}.

the orthoimages (from RGB to IR) is obtained.

As an illustrative example, if the flight speed of the drone is 3 m/s and $\Delta t_{\text{diff}} = 0.01s$ so there is a shift $\Delta s_{\text{diff}} = 3mm$ and correspondingly with $\Delta t_{\text{diff}} = 0.1s$, results in $\Delta s_{\text{diff}} = 30mm$.

The exact results in this work are discussed in detail in section 5.2.

3.3 Transformation matrix

In addition to the synchronisation of the individual time steps, the calculation of a 2-dimensional (2D) geometric transformation matrix is necessary, which transforms the orthoimages from the RGB image into the corresponding IR image due to their different image size.

A 2D geometric transformation is a mapping that associates each point in an euclidean plane with another point in an euclidean plane.

There are different transformation types, which are used according to the application fig. 3.6.

The transformation type needed for this application is the similarity transformation. This describes the usual 4-parameter transformation which includes two displacements, one rotation, and one scale factor between the two systems. Angle and distance ratios are not affected fig. 3.7.

For a point P given in the xy-system (initial system) the XY-coordinates are in the transformed system (target system):

Transformation Type	Description	Minimum Number of Control Point Pairs	Example
`'nonreflective similarity'`	Use this transformation when shapes in the moving image are unchanged, but the image is distorted by some combination of translation, rotation, and scaling. Straight lines remain straight, and parallel lines are still parallel.	2	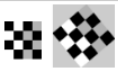
`'similarity'`	Same as `'nonreflective similarity'` with the addition of optional reflection.	3	
`'affine'`	Use this transformation when shapes in the moving image exhibit shearing. Straight lines remain straight, and parallel lines remain parallel, but rectangles become parallelograms.	3	
`'projective'`	Use this transformation when the scene appears tilted. Straight lines remain straight, but parallel lines converge toward a vanishing point.	4	
`'polynomial'`	Use this transformation when objects in the image are curved. The higher the order of the polynomial, the better the fit, but the result can contain more curves than the fixed image.	6 (order 2) 10 (order 3) 15 (order 4)	
`'pwl'`	Use this transformation (piecewise linear) when parts of the image appear distorted differently.	4	
`'lwm'`	Use this transformation (local weighted mean) when the distortion varies locally and piecewise linear is not sufficient.	6 (12 recommended)	

Figure 3.6: Different 2D transformation types [59]

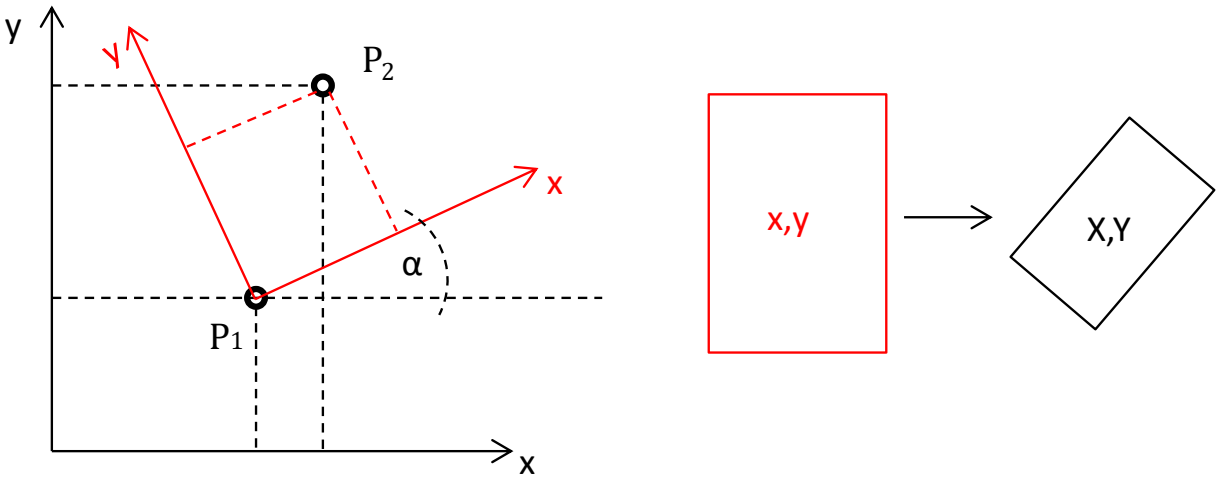

Figure 3.7: Similarity Transformation

$$\begin{aligned} X &= a_0 + a_1 \cdot x - b_1 \cdot y \\ Y &= b_0 + b_1 \cdot x - a_1 \cdot y \end{aligned} \tag{3.6}$$

or,

$$\begin{aligned} X &= a_0 + m \cdot (x \cdot cos\,\alpha - y \cdot sin\,\alpha) \\ Y &= b_0 + m \cdot (x \cdot sin\,\alpha + y \cdot cos\,\alpha) \end{aligned} \tag{3.7}$$

where a_0 and b_0 describe the translation of the origin, alpha the rotation angle, and m the uniform scale factor.

To calculate the four coefficients, at least two identical points are required in both systems. If there are more than two identical points, the transformation parameters are determined by adjusting the overdetermined equation system.

In matrix notation equ. (3.6) can be written as follows:

$$\boldsymbol{X} = \boldsymbol{A} \cdot \boldsymbol{x} + \boldsymbol{a}$$

$$\begin{bmatrix} X \\ Y \end{bmatrix} = \begin{bmatrix} a_1 & -b_1 \\ b_1 & a_1 \end{bmatrix} \cdot \begin{bmatrix} x \\ y \end{bmatrix} + \begin{bmatrix} a \\ b \end{bmatrix} \tag{3.8}$$

or as non-linear form with $a_0 = x_0$ and $b_0 = y_0$

$$\boldsymbol{X} = m \cdot \boldsymbol{R} \cdot \boldsymbol{x} \cdot \boldsymbol{X_0}$$

$$\begin{bmatrix} X \\ Y \end{bmatrix} = \begin{bmatrix} cos\,\alpha & -sin\,\alpha \\ sin\,\alpha & cos\,\alpha \end{bmatrix} \cdot \begin{bmatrix} x \\ y \end{bmatrix} + \begin{bmatrix} X_0 \\ Y_0 \end{bmatrix} \tag{3.9}$$

$\boldsymbol{R}$ is the rotation matrix of the rotation angle α with the orthonormal properties

$$\mathbf{R^{-1}} = \mathbf{R}^{\boldsymbol{T}} \;\; and \;\; \mathbf{R}^{\boldsymbol{T}} \cdot \boldsymbol{R} = \boldsymbol{E} \tag{3.10}$$

The inverse transformation of coordinates of the target system into the original system is done by transforming the image equations equ. (3.9).

$$\boldsymbol{x} = \frac{1}{m} \cdot \boldsymbol{R^{-1}} \cdot (\boldsymbol{X} - \boldsymbol{X_0})$$

$$\begin{bmatrix} x \\ y \end{bmatrix} = \frac{1}{m} \begin{bmatrix} cos\,\alpha & sin\,\alpha \\ -sin\,\alpha & cos\,\alpha \end{bmatrix} \cdot \begin{bmatrix} X - X_0 \\ Y - Y_0 \end{bmatrix} \tag{3.11}$$

In order to evaluate the quality of the transformation matrix, the root mean square (RMS) deviation is calculated.

The RMS value is the mean square deviation between the given target values X and the compensated results X ist:

$$RMS = \sqrt{\frac{1}{n}\sum_{i=1}^{n}\left(X_{target} - X_{actual}\right)^2} \tag{3.12}$$

In the context of this research, a tool (TransMatrixTool) was developed, which allows us to generate a suitable transformation matrix independently from the QFly workflow, which is subsequently integrated into the QFly workflow to transform RGB orthoimages into IR orthoimages. In fig. 3.8 the program structure is illustrated.

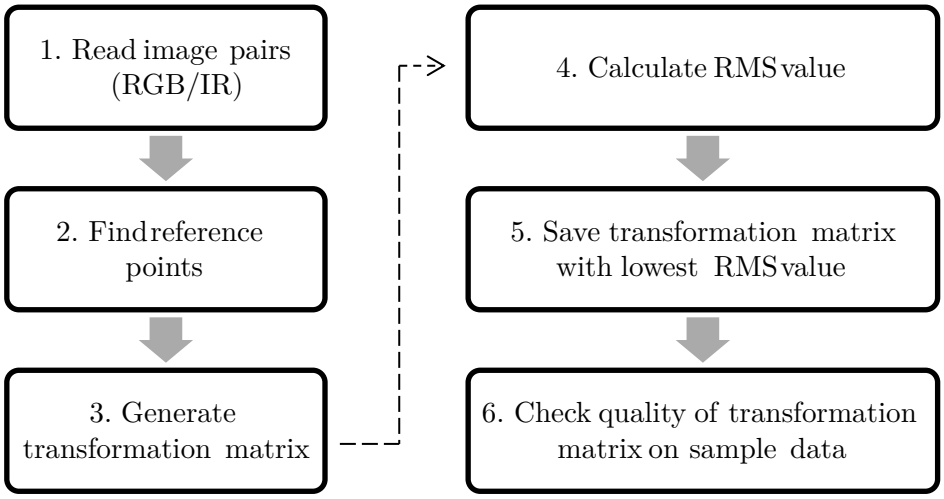

Figure 3.8: Program structure of transformation matrix tool

In the first step (Step 1.), the image pairs (RGB/IR) are loaded. Then reference points are selected based on features (Step 2.). This process is done either manually or automatically using suitable algorithms, both options have been implemented in this workflow.

A 2D geometric transformation matrix is then calculated (Step 3.) for the given image pairs using the selected features and the desired transformation type.

To evaluate the quality of the generated transformation matrix, RMS values are calculated accordingly equ. (3.12), (Step 4.). Afterward, the transformation matrix with the lowest RMS value is stored (Step 5.).

In the last step (Step 6.) the transformation matrix is validated by applying the resulting matrix to all other image pairs.

The detailed analysis and application to real PV systems are presented in chapter 5.

3.4 Enviromental influences (soiling, reflection, sunposition)

Another important aspect that needs to be taken into account when inspecting PV systems with UAVs is the environmental influence.

To ensure good comparability of PV systems reports, the International Electrotechnical Commission (IEC) has published a standard work which describes the concrete procedure for PV system inspections [6].

IEC TS 62446-3 describes that in addition to the IR camera, it is important to consider the environmental conditions at the time of recording. These include irradiance, temperature, and the operation condition of the plant.

According to IEC the inspection should be performed under the conditions specified in tab. 3.1, [6]:

Table 3.1: Required inspection conditions [6]

	Parameter	LimitContinuations
a	Irradiance	• Minimum 600 W/m^2 in the plane of the PV module for PV module inspection • Measured operating current shall be a minimum of 30 % of rated system current within the inspected current path (typically > 30 % of PV module name plate I_{SC} at STC (equals typically > 300 W/m^2 in the plane of the PV modules) for inspection of other electrical components (e.g. cables, connectors, connections). Recommended for inspection are > 600 W/m^2. **NOTE:** Example for single string with no parallel connection: 30 % of STC I_{SC} current. I_{SC} to be taken from PV module name plate and not to be measured on PV plants.
b	Wind speed	Maximum 4 Bft or 28 km/h
c	Cloud coverage	Maximum 2 okta of sky covered by cumulus clouds
d	Soiling	No or low. Cleaning recommend, e.g. if bird droppings exist.

In addition to the environmental conditions, correct positioning is necessary not only in the context of resolution but also due to other physical conditions.

As already described in subsection 2.4.1, the emitted heat radiation of an object depends on the

surface condition and the angle.

In the following fig. 3.9, the emissivity is shown in dependence on the viewing angle of the IR camera. Whereby T_{refl} represents the black body equivalent temperature of the sky (ambient temperature). The graph shows that the emissivity decreases with a decreasing view angle. For this reason, it is important to take the images in a PV system at a constant angle to ensure good comparability of the individual IR images.

On non-ferrous glass the emissivity decreases with the angle of view, so at around 45° the emissivity will be around ε = 0.8 and at 30° it can be around ε = 0.75 or lower.

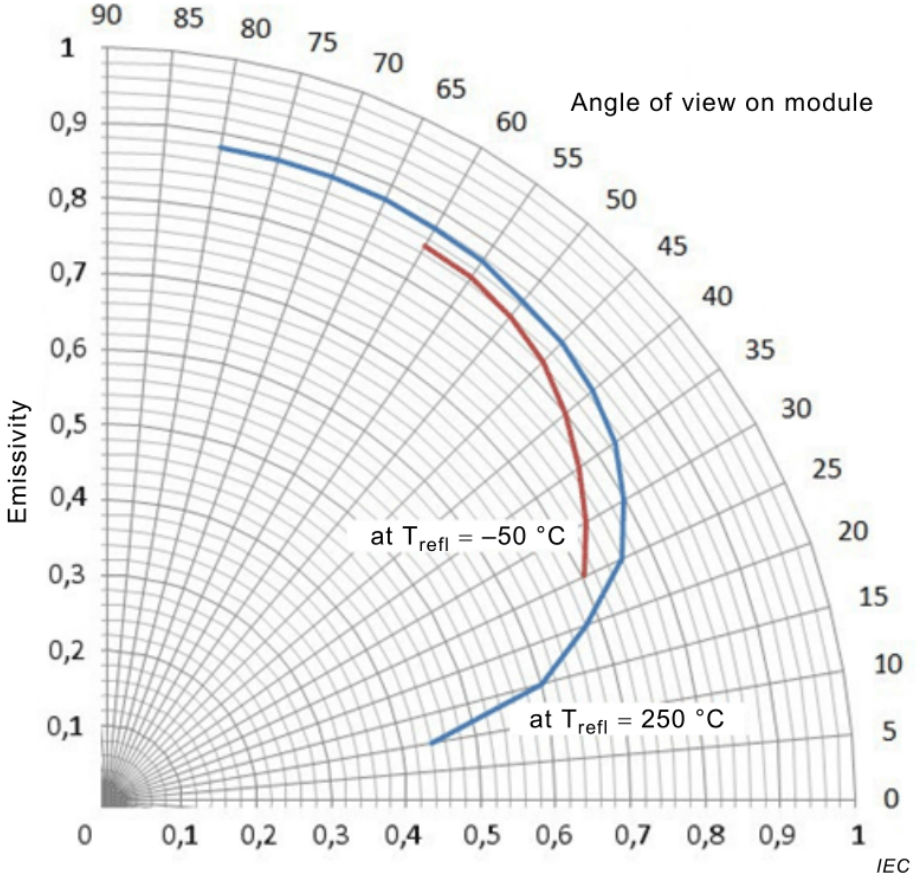

Figure 3.9: Dependence of the emissivity of glass on the angle of view [60]

Figure 3.10 illustrates a typical setup while taking an IR image of a PV Modul. The view angle α and β of the camera between module and camera detector vary. Depending on the angles (α and β) and the size of the object l the effect of recorded temperature in a IR image can be significant.

The reason is that an IR camera is always receiving radiation from at least two sources. Within IR thermograms of PV modules that are the black body radiation from the module (red arrows) and the from the PV module reflected background radiation (green dashed arrows) [60].

The black body equivalent temperature of the sky is typically below $0^{\circ}C$ and is an average of all traversed partly transparent parts of the atmosphere and space temperature [60].

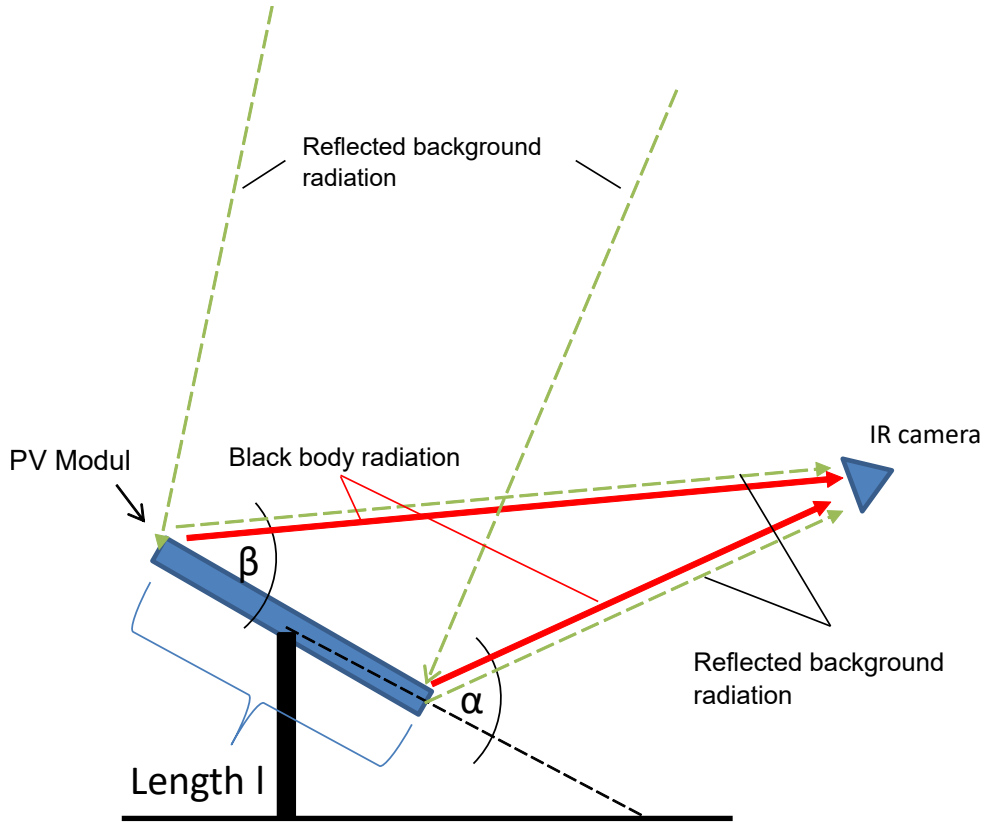

Figure 3.10: Angle of view, depending on the angles (α and β) and the size of the object l the effect of recoded temperature in a IR image can be significant.

At the same time, self-reflection of measuring personnel and IR-camera apparatus/UAV, and reflection of heated objects like sun, near-by buildings and trees shall be avoided. In cases where the image cannot be taken perpendicular to the PV module surface, e.g. a small installation with limited ability to raise the camera, the angle between the camera and the PV module plane should still be greater than 30°.

Furthermore, the position of the sun and the reflection of the sun must be taken into account. A detailed analysis of the proper location in order to minimize reflections of the sun and the sky can be found in [61]. Here a favorable position should be selected so that later in the picture no reflections are present.

Last but not least it is important to constantly monitor the status of the PV generator itself. In the study [60] it turned out that the temperature result of two identical IR images differed due to different operating states of the PV generator. The temperature difference of a PV generator in MPP and in open circuit at 1000 W/m² was 4K for the tested thin-film modules, under identical environmental conditions like irradiance, air temperature, and wind speed.

4 Data acquisition

In this chapter, the used hardware, the basic experimental procedure, and the corresponding hardware parameters are presented. Two data sets were generated, one from the PV system and one for the calibration of the transformation matrix.

4.1 Hardware

The drone used in this work is manufactured and distributed by the company DJI and is called Mavic 2 Enterprise Dual Camera.

The Mavic 2 Enterprise Dual features a gimbal camera fully stabilized on three axes, with a long-wave FLIR infrared thermal (IR) camera and a visual camera (RGB), displaying both long-wave invisible infrared radiation and images in the visible spectral range. The infrared thermal camera records 160 × 120 videos. The view camera records 4K videos with 30 fps and 12 MP photos.

DJI's OcuSyncTM 2.0 long-range transmission technology integrated into the remote control offers a maximum transmission range of 10 km and video transmission from the airborne device to the DJI pilot with up to 1080P. The remote control operates at both 2.4 GHz and 5.8 GHz and can automatically select the best transmission channel without latency delay. The drone and camera can be controlled with the built-in joysticks. The DJI Pilot is connected to the mobile device and provides real-time information and data about the airborne device. The Mavic 2 Enterprise series has a maximum flight speed[1] of 72 km/h and a maximum flight time[2] of 31 minutes.

The integrated IR camera manufactured by FLIR, has the following specifications [62].

Table 4.1: Thermal imaging camera specification: Mavic 2 Enterprise Dual [62]

thermal imaging camera	
Sensor	uncooled VOx microbolometer

continued on next page

[1] The maximum flight speed was tested at sea level with no wind. These values are for reference only.
[2] The maximum flight time was tested in a non-wind environment while flying at a constant speed of 25 km/h.

Thermal imaging camera specification: Mavic 2 Enterprise Dual

thermal imaging camera	
Lens	horizontal field of view: 57° aperture: f1.1
Array format	160 x 120
Spectral range	Longwave infrared, 8 μm to 14 μm
Fotomode	single shot serial image recording: 3/5/7 images intervall (2/3/5/7/10/15/20/30/60 s)
Videomode	160 x 120 with 8.7 fps

It is important to mention once again that this version of the camera is a non-radiometric camera.

4.2 Dataset 1: PV system

In the first series of measurements, a real PV system was examined which was in operating mode.

The investigated PV system fig. 4.1 is based on silicon modules. The illustration in fig. 4.1 demonstrates the experimental setup of the IR analysis. In total a module string with 2 x 24 modules was examined. The size of each module is 990 x 1645 mm. However, only a section of these 2 x 24 modules was analyzed in the further process, see section 5.4. Each module consists of 60 cells measuring 165 x 165 mm. Each module has an inclination of about 57°. The drone is located at a distance of about 5.3 m which varies slightly during the test flight.

In this test series, the system was flown manually without planning specific flight routes.

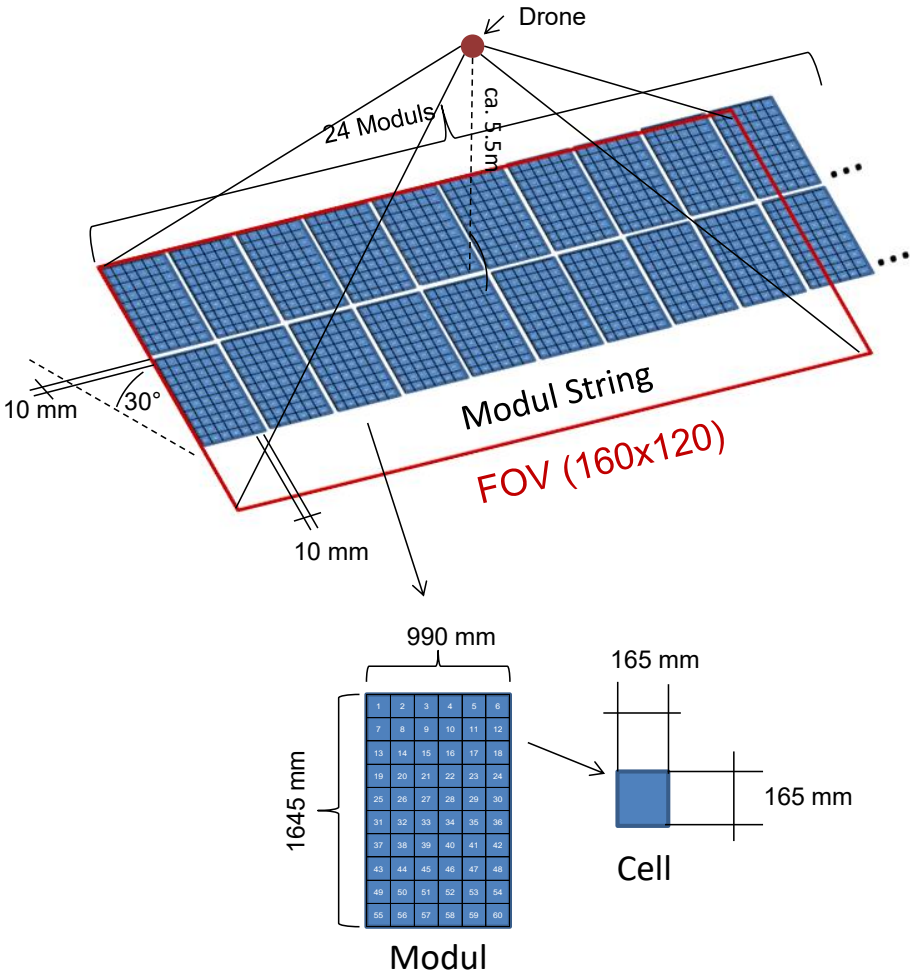

Figure 4.1: Experimental setup of PV plant inspection with IRT and UAV.

The process can be broadly classified as follows.

- 1. Place drone
- 2. Start flight mode
- 3. Move the drone to the desired position using the joystick
- 4. Start recording mode
- 5. Fly as constantly as possible over the PV panels
- 6. Quit recording mode
- 7. Safe landing of drone

A well-trained drone operator is required to perform these steps properly.

Subsequently, the drone stores the recorded video material as mp4. file. In addition to the video recordings, the Global Positioning System (GPS) coordinates and timestamps are also written automatically into a separate .srt [3]. The .srt file contains the following Dinformation.

- FrameCnt : 1

[3] .srt is a subtitle format file extension and is a widely supported file format [63]

- DiffTime : 114ms
- Timestamp: Date and Time
- GPS Data: latitude, longitude, altitude
- Drone orientation: Yaw, Pitch, Roll

Besides the video mode, the drone also offers a serial image function. Since this mode has a significantly lower frame rate, the video mode was used for data acquisition.

This information is used in the QFly workflow for orientation of the camera, see section 2.5.

4.3 Dataset 2: calibration of IR and RGB camera

This data set is used to generate the transformation matrix from RGB to IR image, see section 3.3.

For this purpose, an area measuring 2.20 x 1.40 m was recorded from different distances fig. 4.2. A total of 4 videos were selected for evaluation, in which the distance from the camera to the measurement object was varied. Besides, the images were taken perpendicular to the measured object.

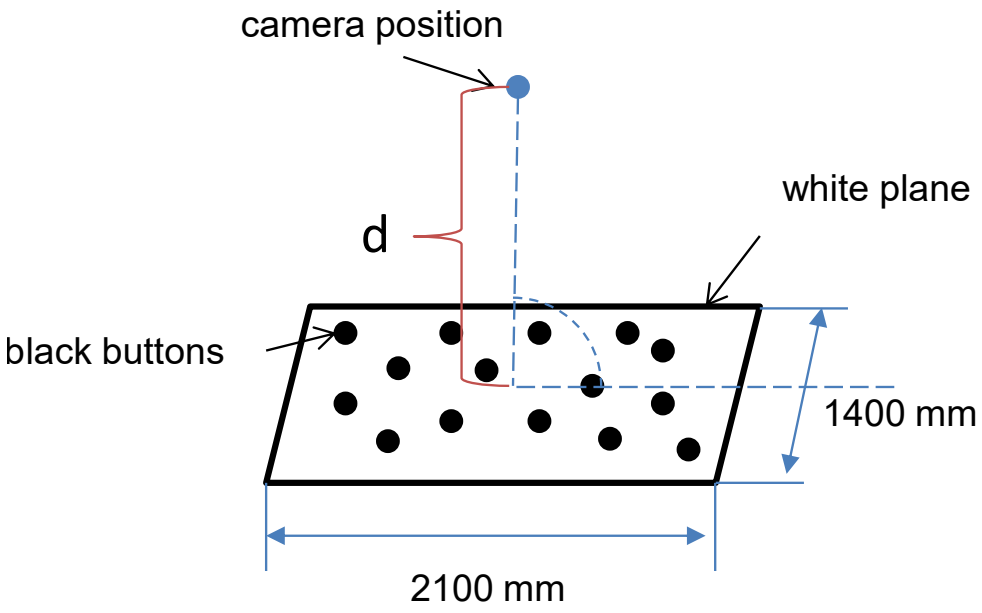

Figure 4.2: Measurement setup of dataset 2

Table fig. 4.2 shows the respective distances d from the measured object.

Table 4.2: Sample distance to the measurement object

Video Nr.	Distance d	Resolution per pixel
Video 1	1631 mm	15,68 mm/pixel
Video 2	1474 mm	14,18 mm/pixel
Video 3	2090 mm	20,10 mm/pixel
Video 4	1190 mm	11,44 mm/pixel

For the necessary contras which later represent the feature points, 17 black buttons in different sizes (1 - 4cm) were attached to the white surface.

The black button used, enable a good contrast in the IR images. Due to the higher emission coefficient they appear warmer in the IR image.

This provides a suitable basis to click similar positions in the IR and RGB image (see section 3.3) when selecting a feature.

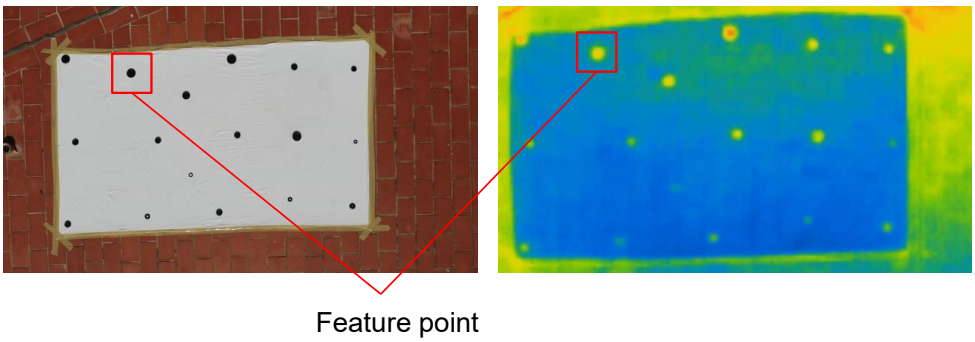

Figure 4.3: RGB Image (left), IR image (right) at a Distance d = 2090mm

5 Results and Discussion

This chapter focuses on the results of the challenges already presented in chapter 3. This chapter is divided into 4 sections. In the first section 5.1 the results concerning the flight altitude vs resolution are discussed. In the second part 5.2 the implementation of the synchronisation timestamps is presented. In the third section 5.3 the results with respect to the implementation of the transformation matrix are presented. In the fourth and last part 5.4 the results concerning the automatic defect detection are shown.

5.1 Flight altitude vs. resolution

As already discussed in section 3.1, the distance of the camera to the measuring object plays an important role.

The 5.3 m distance to the measuring object selected in this test series results in a resolution of 32.94 mm/ pixel. Considering the size of the individual cells of 165 x 165 mm, this corresponds to a resolution of approximately 5 x 5 pixels per cell.

According to the GSD of 30 $\pm$ 0.5 mm/pixel specified by IEC TS for a comprehensive inspection (see subsection 2.4.1), the resolution in this test series only minimally misses the given requirement (ΔGSD = 2.94 $\pm$ 0.5 mm/pixel).

Since the IR camera used does not generate radiometric images, no absolute temperatures are recorded. Therefore theoretically a resolution of 55 $\pm$ 0.5 mm/ pixel would be sufficient, which would correspond to a distance to the measuring object of approx. 9m. This degree of resolution is classified as inspection type „standard“, which enables the successful detection of defective diodes, hot spots, and cells, see tab. 2.1.

The following figure fig. 5.1 shows an example of image pairs generated in this test series (RGB image on top and IR image at the bottom).

From the two images, it can be seen immediately that the field of view of the RGB camera is significantly larger than that of the IR image. The reason for this is the different resolutions and the different lens parameters.

The RGB image above has a high resolution (3840 $\times$ 2160 pixels), so that individual cells in the respective modules are visible. This provides a good foundation for the feature detection tools used in post-processing.

Due to the much lower resolution of the IR camera, the IR image has a much lower degree of detail. In most cases, the exact edges of the individual modules cannot be seen with the naked

eye. To better analyze the intensity distribution of the thermal radiation, a section was drawn through the center (red dotted line), and the corresponding intensity distribution (unitless) was plotted over the distance y (mm), fig. 5.2.

Additionally one can see that the aluminum frames of the modules appear colder in the picture than the cells themselves. The main reason is the smaller emission coefficient (anodized aluminum epsilon = 0,55) of aluminum and because they reflect the heat radiation of the sky (typically below $0^{\circ}C$), see section 3.4. In practice, this would mean that a radiometric thermal imaging camera would show the frame temperature as below 0°C [64, 65]

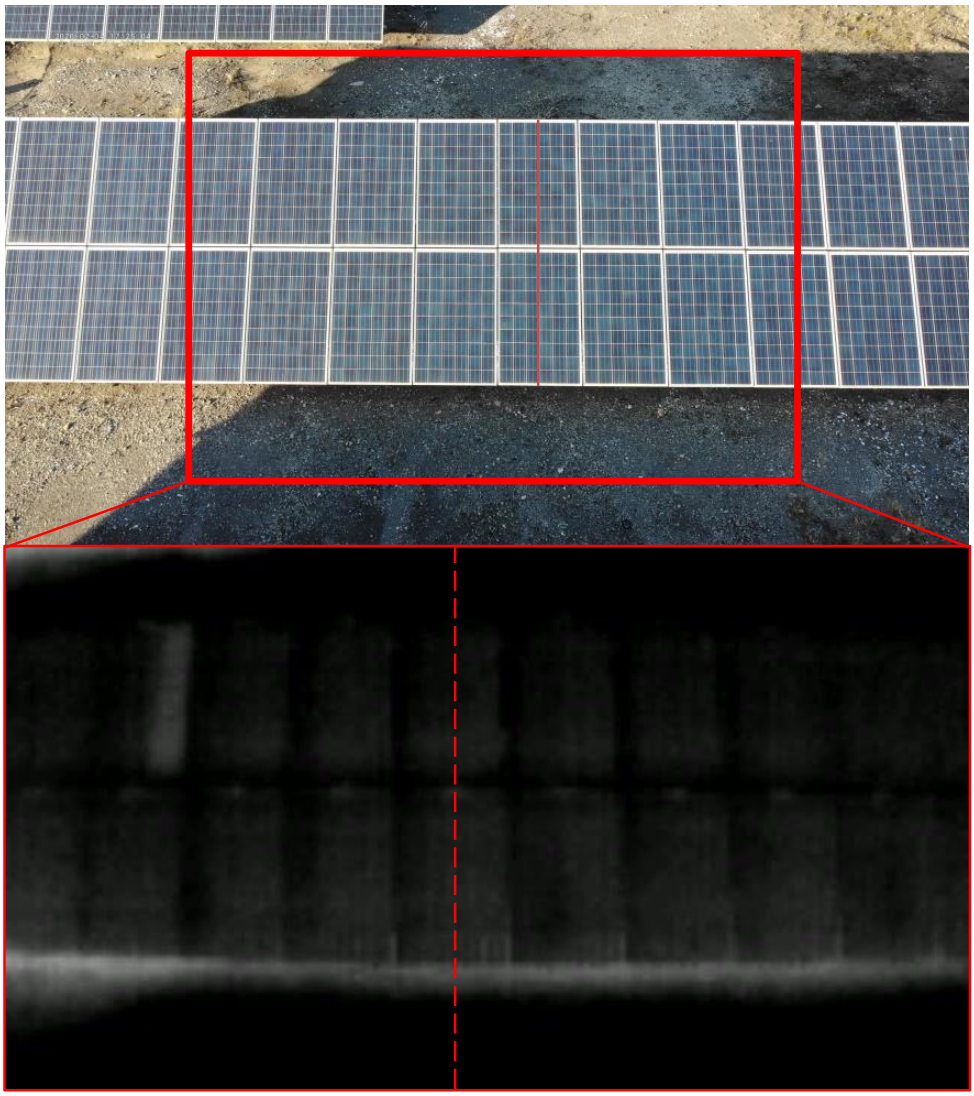

Figure 5.1: RGB Image (up), IR image (down) at 5,3 m distance from PV Modules height

A closer look at the intensity values immediately reveals that the intensity values in the upper module are significantly lower than those in the lower module.

A possible reason for this fact is that the camera is not exactly 90 grad to the measured object, and thus the emission coefficient changes with the change of the angle, see section 3.4.

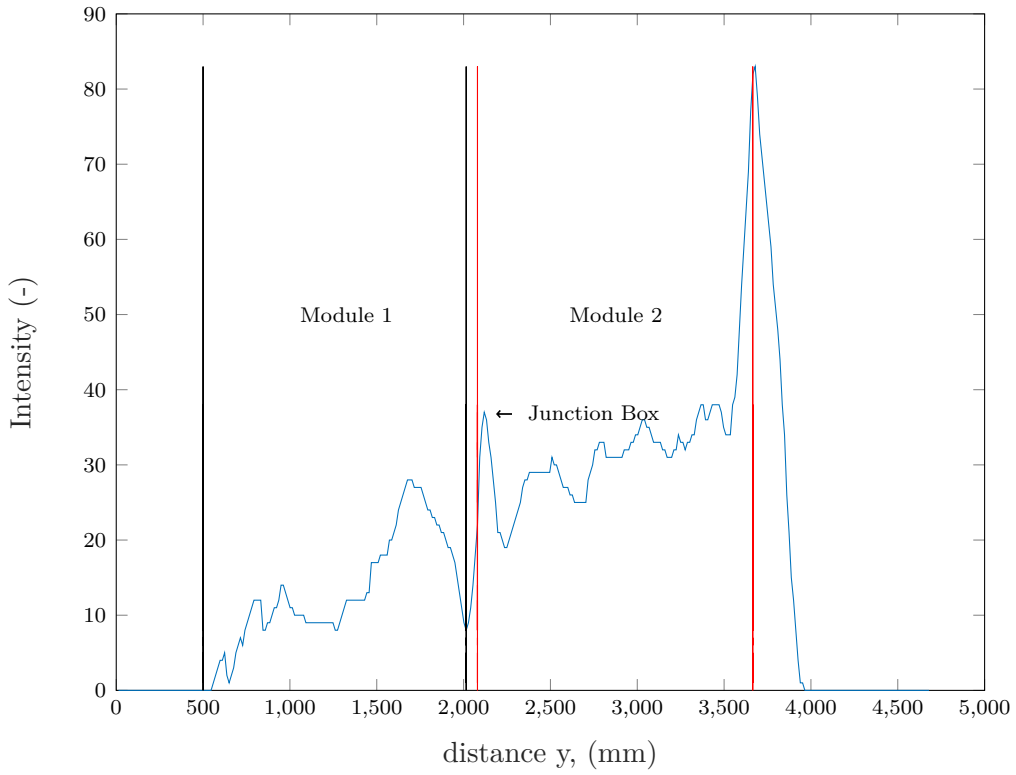

Figure 5.2: Intensity distribution over distance y (mm)

The same phenomena has already been investigated by G. Álvarez-Tey et. al. [61]. There the linear temperature rise is based on the reflection of the sky at the top of the PV module due to gradual change of the emissivity. Another reason for the temperature gradient from bottom to top is the higher air circulation at the top.

A second reason could be that the lower panels, which are closer to the ground, heat up more due to the heat radiation from the earth than the modules, which are higher to the ground.

A third explanation could be that the linear increase is due to the celestial reflex. The modules on the upper string look more towards the zenith, where the sky is colder, whereas the modules further down (lower string) look towards the horizon. However, the exact cause could not be determined in the course of this study, and therefore requires further investigation.

Also, the increased temperature on the surface of the PV module at the respective position of the attached junction boxes can be identified. The heating inside junction boxes mainly appears due to electrical losses caused by the ohmic resistance of electrically conductive components [66].

Below the lower module 2, a bright line can be seen, this can also be identified by the strong increase in intensity from about 35 to over 80 units in the intensity plot. A possible reason could be that the sunrays are reflected at the radius of the aluminum profile.

In summary, the generated RGB and IR images at the given altitude contain enough information to detect defective diodes, hot spots, and defective cells.

5.2 Synchronisation timestamps

As already described in chapter 3.2, the different frame rates of the IR and RGB cameras result in a synchronisation error $\Delta t_{Diff}(s)$.

To solve this problem a function was implemented in the QFly workflow, see 2.5, which allows us to extract image pairs with the smallest possible time difference from the raw video material.

The results of the implemented function are explained below.

The following figure fig. 5.3 shows the synchronisation errors $\Delta t_{Diff}(s)$ between RGB and IR image for individual frames.

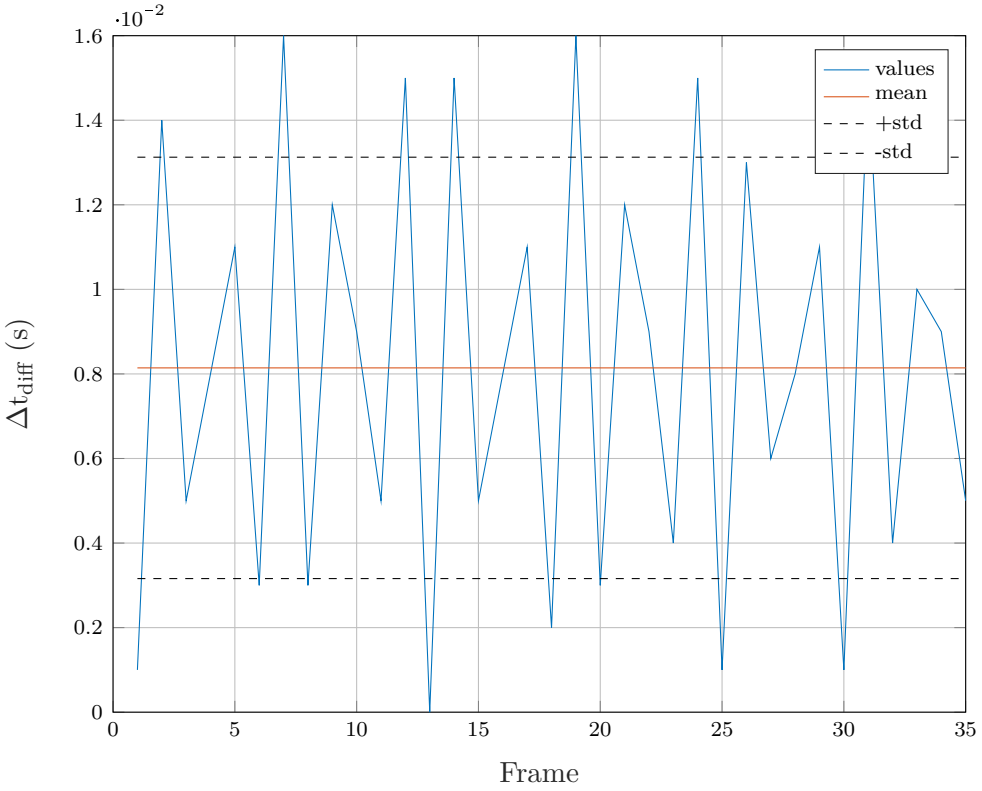

Figure 5.3: Absolute time difference $\Delta t_{Diff}(s)$ between IR and RGB Frames

The mean time error is $\mu_{Time} = 0.81e-02s$ with the standard deviation $S_{Time} = 0.49e-02s$. The mean time deviation was calculated using equ. (5.1) and the standard deviation using equ. (5.2).

$$\mu = \frac{1}{N}\sum_{i=1}^{N} A_i \tag{5.1}$$

$$S = \sqrt{\frac{1}{N-1}\sum_{i=1}^{N}\left|t_{Diff} - \mu\right|^2} \tag{5.2}$$

The maximum synchronisation error is 1.6e-02 s at frame 7 and 19, and the smallest is 0, indicating a perfect match of RGB and IR image.

With an average flight speed of 3 m/s and a maximum time difference of delta t = 1.6e-02 s, the spatial deviation $\Delta s_{diff_{max}} = 48mm$.

The average error is accordingly $24.3mm \pm 14.7mm$.

Considering that a pixel has a resolution of approx. 32.9 mm/pixel, the absolute error is 4/3 of a pixel.

This accuracy is sufficient to get a good synchronisation of IR and RGB. Note that the resulting error Δs_{diff} depends on the flight speed.

5.3 Transformation matrix

In this section, the results concerning the creation of a suitable transformation matrix are discussed. As already mentioned in chapter 2.5, this step is necessary to transfer orthoimages from the RGB to the IR image.

In the beginning, a suitable transform type has to be determined. As already presented in section 3.3, fig. 3.6, there are several types to choose from.

For the validation of a suitable transformation type, several validations have been carried out. It was found that the transformation types „similarity“ and „lwm“ give the best results, whereas the transformation types „pwl“ and „polynomial“ distort the image.

All further results are based on the transformation type „similarity“. The big advantage of the transformation type „similiarity“ is that only a few reference points ≥ 3 are needed, whereas „lwm“ needs more than ≥ 12 points. At the same time, the image of „lwm“ is slightly distorted due to the individual weighting factors.

For the generation and validation of a matrix, the „TransMatrixTool“ was developed, which was already presented in the section 3.3.

For the generation of a suitable transformation matrix, a total of 4 videos with 3-4 images each were used, see section 4.3.

In the first step, the feature points are clicked manually (guessed points) and then automatically selected with software developed by DLR. This involves projecting an ellipse onto the image area based on the existing contour differences and selecting the center point, see fig. 5.4.

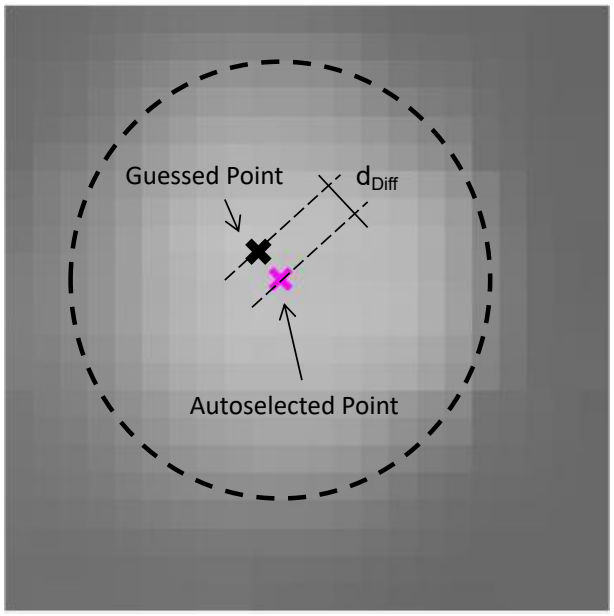

Figure 5.4: Manual-selected (Guessed Point) and auto-selected Point

In the following the differences measured in RMS of the manually selected points and the automatically found points are validated.

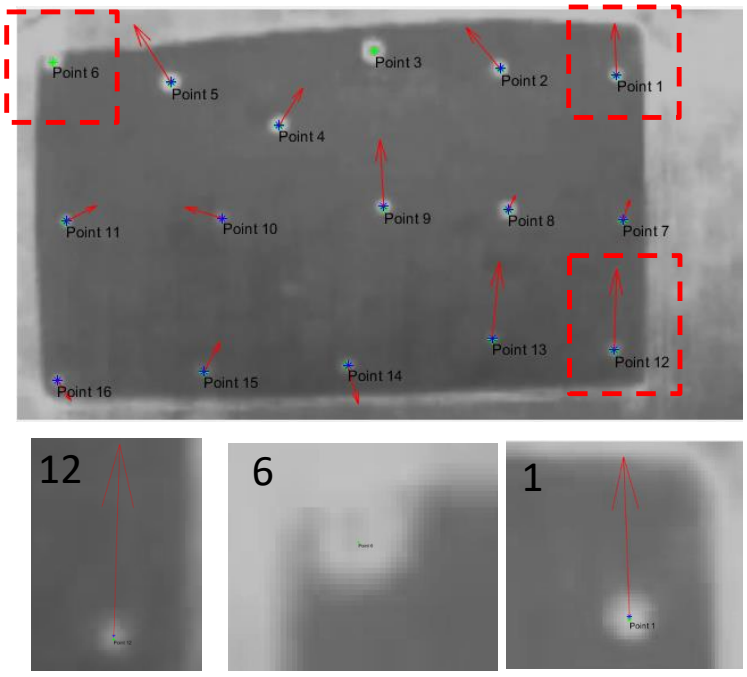

Point Nr.	d_{Diff} (pixel)	d_{Diff} (mm)
Point 1	0,29	4,59
Point 2	0,28	4,33
Point 3	NaN	NaN
Point 4	0,23	3,67
Point 5	0,36	5,68
Point 6	NaN	NaN
Point 7	0,12	1,88
Point 8	0,09	1,42
Point 9	0,38	5,95
Point 10	0,17	2,67
Point 11	0,16	2,48
Point 12	0,46	7,18
Point 13	0,43	6,73
Point 14	0,22	3,47
Point 15	0,18	2,82
Point 16	0,13	2,00

Figure 5.5: Guessed points on the surface with corresponding normal vectors d_{diff} (left), table with difference values between manual clicked and auto-selected points (right)

Figure fig. 5.5 shows that out of a total of 14 points 16 points could be detected automatically. This value varies across all image pairs.

The maximum divergence is in point 12 with d_{Diff} = 0.46 pixel which would correspond to a

discrepancy of d_{Diff} = 7.18 mm. Point no. 6 and no. 3 could not be detected successfully. If one looks closer at point 6, it can be seen that the contrast difference is not completely closed, so that the algorithm could not produce an ellipse on the 2D surface and therefore no point could be detected.

The average deviation over all points is d_{Diff} = 0.25 pixel or 3.91 mm.

As mentioned above, not all auto-detected points can always be generated using the corresponding manually clicked feature points. For the type „similar“ this is not a problem, because theoretically, n≥ 3 points are sufficient to calculate a transformation matrix.

However, it is different from the other types of transformation matrices, which usually require a significantly higher number of points.

If the feature points are successfully detected, the next step follows, see section 3.3.

In this step (Step 3. and 4.), the transformation matrix and the resulting RMS values are calculated for the individual image pairs of the respective video sequences. Afterward, the transformation matrix with the smallest value is saved (Step 5.).

In the following table, the transformation matrix of type „similarity“ is calculated for a total of 15 image pairs (RGB/IR).

Table 5.1: In this table the transformation matrix of type „similarity“ is calculated for a total of 15 image pairs (RGB/IR). In the third column the RMS values of individual transformation matrices are given. First the RMS values were converted into pixel according to equ. (5.5), then the scaling ratio was taken into account equ. (5.6). In the last column the RMS values were converted from pixel to mm.

Video	Image pair	RMS_Similarity [Pixel]	RMS_Similarity (4:3) [Pixel]	RMS_Similarity (4:3) [mm]
Video1	1	3.81	0.86	13.51
Video1	2	4.05	0.92	14.46
Video1	3	4.18	0.95	14.95
Video1	4	4.23	0.98	15.38
Video2	1	4.50	1.15	16.37
Video2	2	4.37	1.14	16.13
Video2	3	4.18	1.07	15.20
Video2	4	4.34	1.13	15.98
Video3	1	1.66	0.43	8.57
Video3	2	1.41	0.37	7.53
Video3	3	1.41	0.37	7.53
Video4	1	3.52	0.93	10.64
Video4	2	5.17	1.14	13.01
Video4	3	3.40	0.90	10.28

In the first column, the individual videos no. 1 to 4 are counted from which each of the videos

contains 3 - 4 images pairs. The RMS value in the third column refers to the pixel deviation on the existing image format which is artificially upscaled by the video format in a ratio of 4:3, i.e. instead of 160x120 pixels to 640x360 pixels. The last column of the table is displayed as a bar chart in fig. 5.7.

The RMS values are calculated as follows.

In equ. (5.3), $A_{\text{Calculated}}$ represents the calculated points by applying the inverse transformation matrix to the individual clicked feature points of the IR image and subtracting each point by $B_{ControlPoints}$ which represent the manual clicked points in the RGB image. This results in $M_{DiffCheck}$. Then in equ. (5.4) the normal vector of the individual x and y coordinates of $M_{DiffCheck}$ is calculated. Finally, the mean value over all normal vectors is determined and reported in tab. 5.1, see equ. (5.5). To calculate the actual pixel deviation and the corresponding deviation in mm, the x and y coordinates of DiffCheck were divided by factor 4 and 3, see equ. (5.6).

$$\mathbf{M}_{\text{DiffCheck}} = \mathbf{A}_{\text{Calculated}} - \mathbf{B}_{ControlPoints}$$
$$\begin{bmatrix} m_{x1}m_{y1} \\ \dots \\ m_{xn}m_{yn} \end{bmatrix} = \begin{bmatrix} a_{x1}a_{y1} \\ \dots \\ a_{xn}a_{yn} \end{bmatrix} - \begin{bmatrix} b_{x1}b_{y1} \\ .. \\ b_{xn}b_{yn} \end{bmatrix} \tag{5.3}$$

$$\mathbf{N}_{vec} = vectorNorm\,(\mathbf{M}_{\text{DiffCheck}})$$
$$\begin{bmatrix} n_1 \\ \dots \\ n_y \end{bmatrix} = vectorNorm\Big(\begin{bmatrix} m_{x1}\,m_{y1} \\ \dots \\ m_{xn}\,m_{yn} \end{bmatrix}\Big)\ \ with,$$
$$\|n_i\| = \sqrt{\sum_{k=1}^{N} |m_{xk} - m_{yk}|^2} \tag{5.4}$$

$$\mathbf{R}_{RMS} = \text{mean}\,(\mathbf{N}_{vec})\ \ with,$$
$$\mathbf{R}_{RMS} = \frac{1}{N}\sum_{i=1}^{N} N_{vec_i} \tag{5.5}$$

$$\mathbf{N}_{vec} = vectorNorm\,(\mathbf{M}_{\text{DiffCheck}})$$
$$\begin{bmatrix} n_1 \\ \dots \\ n_y \end{bmatrix} = vectorNorm(\begin{bmatrix} \frac{m_{x1}}{4} & \frac{m_{y1}}{3} \\ \dots & \\ \frac{m_{xn}}{4} & \frac{m_{yn}}{3} \end{bmatrix})\ with, \tag{5.6}$$
$$\|n_i\| = \sqrt{\sum_{k=1}^{N} \left| \frac{m_{xk}}{4} - \frac{m_{yk}}{3} \right|^2}$$

On closer inspection of the individual values, it is immediately apparent that Video 3, image pair 2, and 3 show the best RMS values of 0.37 pixels, which would correspond to an RMS value of 7.53 mm.

The reason for this behavior is the relative central allocation of the clicked feature points, see fig. 5.6, c). The more points are located at the edge, the greater the deviation between the calculated points and the auto-detected feature points.

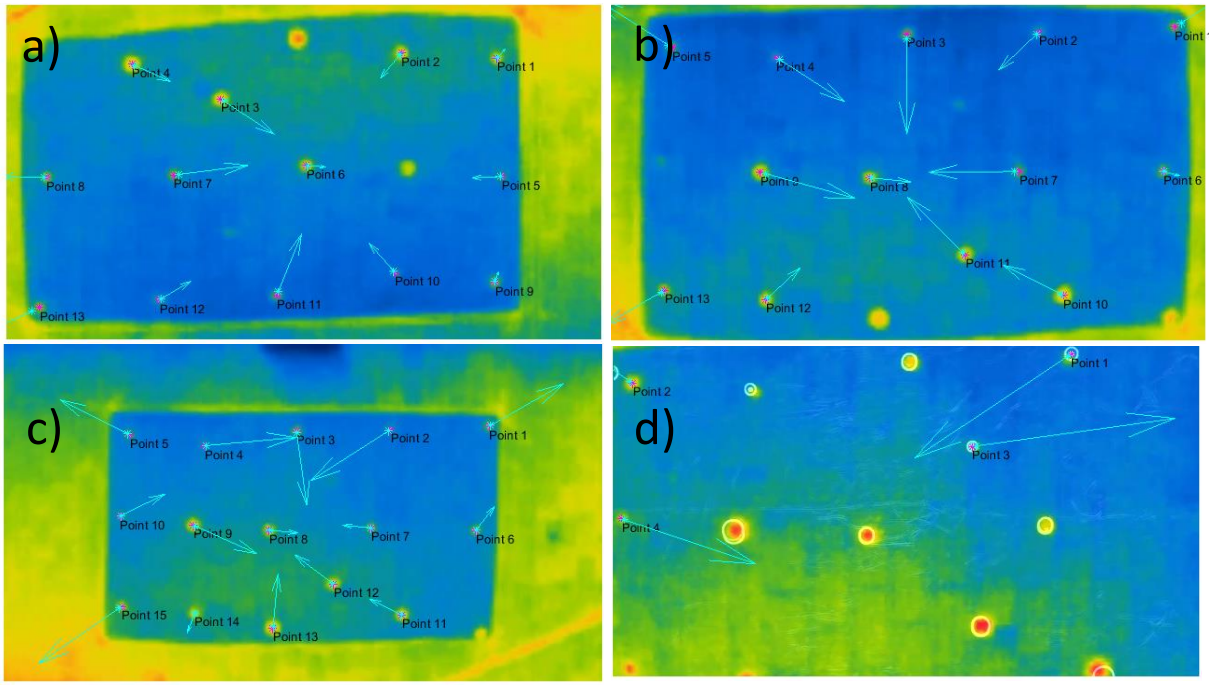

Figure 5.6:]
Overview a) Video 1 Image Pair 2 b) Video 2 Image pair 1 c) Video 3 Image pair 1 d) Video 4 image pair 1

The reason is the radial-symmetric distortion, which has not been taken into account at this point so far. Radial-symmetric distortion is an aberration caused by changes in refraction of the lens and is dependent on the current focus and the object distance at constant focusing [2].

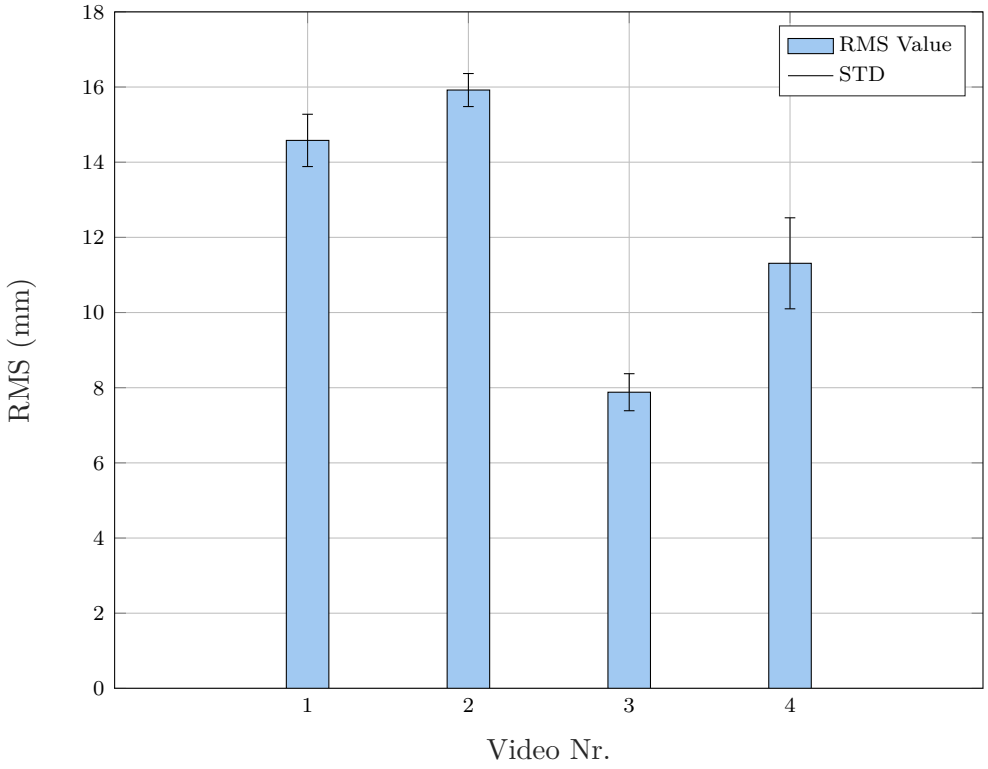

Figure 5.7: Mean RMS with corresponding STD in video 1 - 4 according to tab. 5.1, here the transformation matrix is calculated for each image pair individually

In order to develop a suitable correction function, a camera calibration of the IR camera must be carried out. Unfortunately, this step is not yet implemented.

In the next step, the quality of the transformation matrix will be compared with the lowest RMS value (Step 5.). Therefore the matrix with the smallest RMS value is saved and applied to all image pairs.

The following tab. 5.2 shows the results of this quality check (Step 6.). Also in this step, the RMS values are calculated using equ. (5.3) to equ. (5.6), only with the difference that the same transformation matrix (transformation matrix with the smallest RMS value which was saved in Step 5.) is applied to all image pairs.

Table 5.2: In this table the main transformation matrix with the smallest RMS value which was saved in Step 5. is applied to Video 1 to 4. The third column represents the RMS values applying the main transformation matrix. First the RMS values were converted into pixel according to equ. (5.5), then the scaling ratio was taken into account equ. (5.6). In the last column the RMS values were converted from pixel to mm.

Video	Image pair	RMS_Similarity (Pixel)	RMS_Similarity (4:3)(Pixel)	RMS_Similarity (4:3) (mm)
Video1	1	7.20	1.43	22.36
Video1	2	7.60	1.49	23.43
Video1	3	7.59	1.44	22.63
Video1	4	7.01	1.24	19.45
Video2	1	15.27	3.99	56.55
Video2	2	11.55	2.96	42.01
Video2	3	8.18	1.72	24.45
Video2	4	9.19	2.05	29.01
Video3	1	1.77	0.45	8.95
Video3	2	1.41	0.37	7.53
Video3	3	1.41	0.37	7.54
Video4	1	12.80	2.61	29.89
Video4	2	11.90	2.26	25.90
Video4	3	13.27	2.70	30.88

Again, video 1, 2, and 4 show relatively high RMS values, see tab. 5.2. Comparing these values with the original values from the diagram, fig. 5.8, it is noticeable that the deviations are much larger. The reason for this is that in the previous process step a transformation matrix was calculated individually for each image pair and then the RMS value was determined through formulas equ. (5.3) to equ. (5.6), whereas now only one transformation matrix (main transformation matrix) from video 3 image pair 2 is used for all other image pairs.

The reason for this is that the more points are at the outer edge of the image, the greater the deviation, and the higher the resulting RMS value fig. 5.9. This means that e.g. video 2 will have a greater difference from video no. 1 or video no. 4. Because video 2 contains the highest number of points, which are located at the edge of the image, see fig. 5.9.

This transformation matrix is now used for the video recordings of the real PV system, see section 4.2.

The following can be derived from the above-described relationships for the application of the transformation matrix to real PV systems. As long as the examined modules are located in the center of the image, the superposition of RGB to IR orthoimages should be with an accuracy of 0.37 pixels. And the further the PV modules are located at the edge of the IR image, the greater the deviation. The maximum deviation in video 2 image pair 1 is 3.99 pixels, see tab. 5.2. The

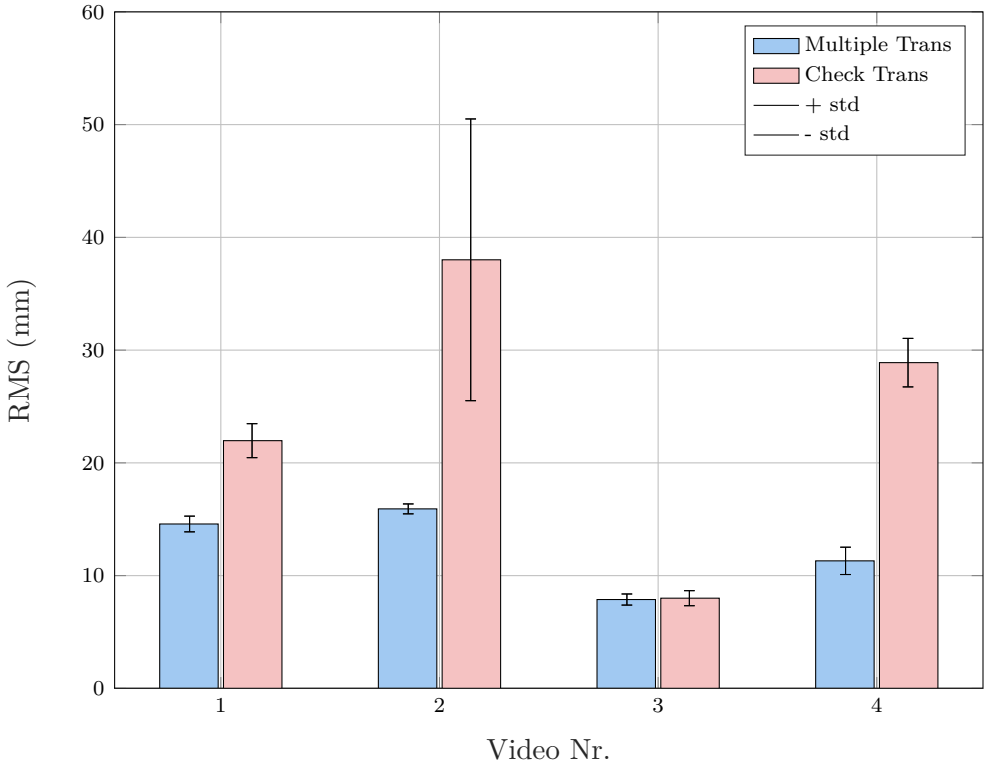

Figure 5.8: Compare RMS vlaues of Group 1: Multiple trans matrix vs. Group 2: Main Transformation matrix with corresponding error in video 1 - 4

further away the modules are from the center of the image, the greater the deviation due to radial-symmetric distortion.

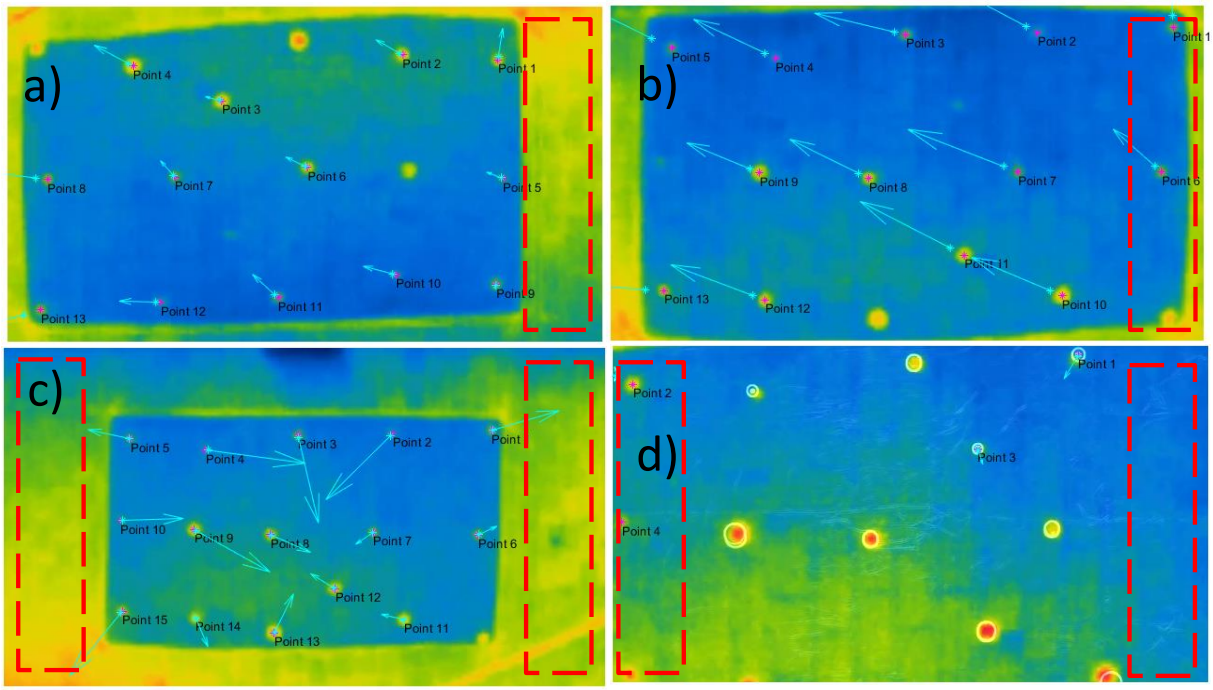

Figure 5.9: Overview a) Video 1 Image Pair 2 b) Video 2 Image pair 1 c) Video 3 Image pair 1 d) Video 4 image pair 1, Video 2 contains the highest number of points, which are located at the edge of the image, this leads to higher RMS values

5.4 Defect detection

5.4.1 Defect detection on module level

In this subsection, the limits and possibilities of automatic defect detection using IR imaging are presented.

A time interval from 00:59:01 to 01:01:02 was selected from the data set presented in section 4.2, from which a total of 18 image pairs (IR/RGB) were extracted considering the minimum time difference, see section 3.2.

Subsequently, the 3-dimensional (3D) model, the camera position, and the feature points in the RGB image were used to create orthoimages in the RGB image, see 2.5.

The orthoimages from the RGB image are then transferred to the IR image using the generated transformation matrix, see section 3.3.

The following illustration fig. 5.10 shows an example of an orthoimage generated from the RGB image.

It can be seen in fig. 5.10, that in Image 01 the QFly algorithm has successfully detected a module from the RGB Image. Below this image, the corresponding IR image taken with the IR camera can be observed.

As mentioned above, the orthoimage can be transformed from the RGB image to the IR image

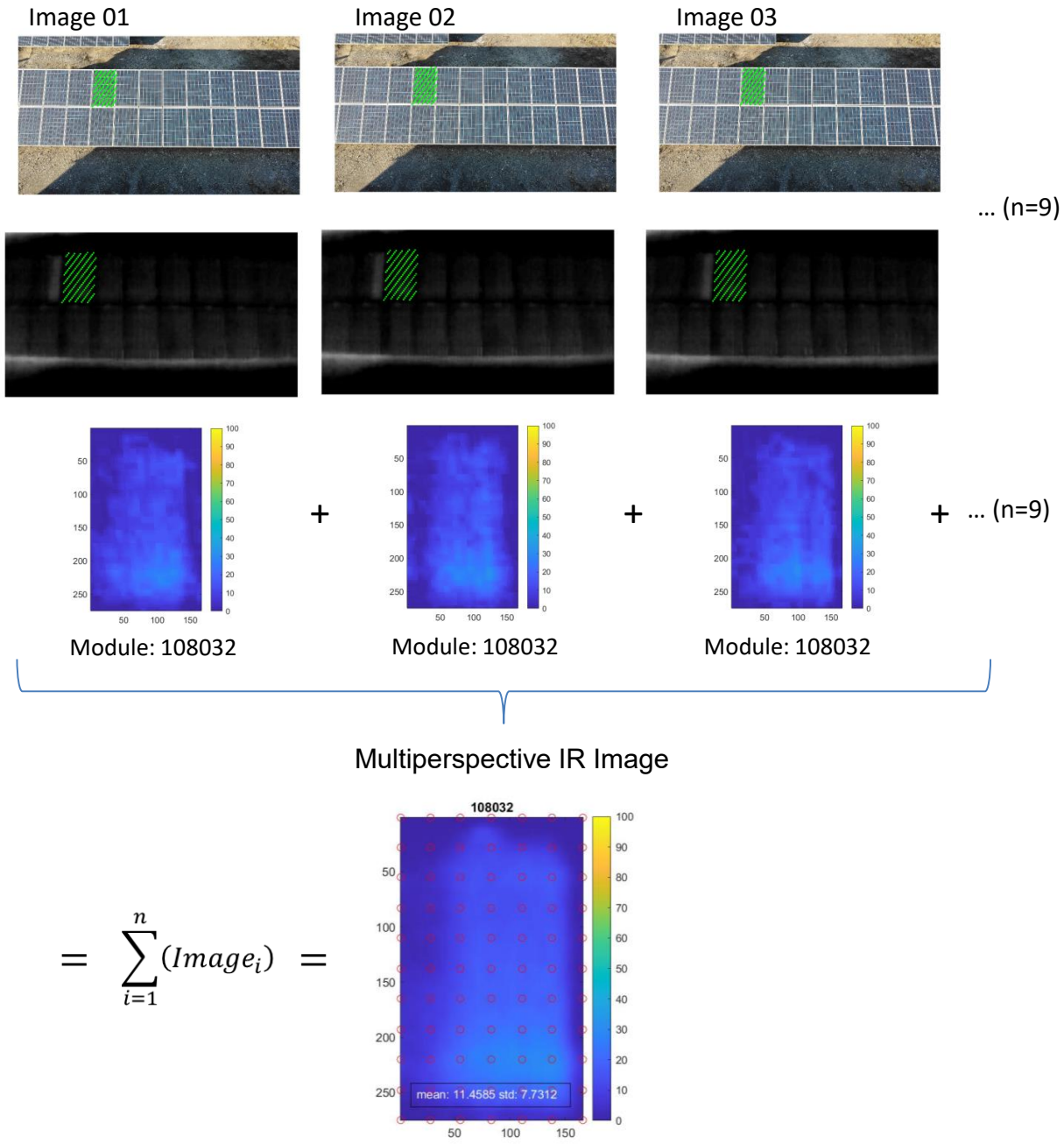

Figure 5.10: Automatic defect detection workflow presenting RGB orthoimage, IR orthoimage, extracted intensity profile and corresponding multiperspective IR image

using the transformation matrix.

The extracted orthoimage from the IR image is then displayed in a false-color scale from 1 to 100. These values correspond quantitatively to the heat radiated from the module surface.

As the same module is located in multiple image sections, it can be extracted from several images and combined to a multiperspective IR Image (fig. 5.10, below).

The big advantage of a multiperspective IR image is that the intensity profile is homogenized and thus measurement errors due to local image errors such as overexposure, sun reflex, etc. can

be avoided.

In other words, multiple measurement data are available for statistical evaluation.

In this example, the same module (ID=108032) was found in a total of n=9 images and merged into a multiperspective orthoimage.

The resulting multiperspective IR image is the basis for further statistical evaluations.

Afterward, the mean value of the intensity distribution within a module can be calculated.

Besides, two different types of standard deviations can be calculated. One is related to the mean values of the individual orthoimages (STD_{mean}) and the second is related to the standard deviation of the intensity values of a multiperspective IR image ($STD_{intensity}$).

Figure fig. 5.11 schematically shows all successfully detected modules with the corresponding module ID, starting with 108021 and ending with ID number 108046 with the corresponding intensity distribution. A total of 26 modules were successfully detected in this data set.

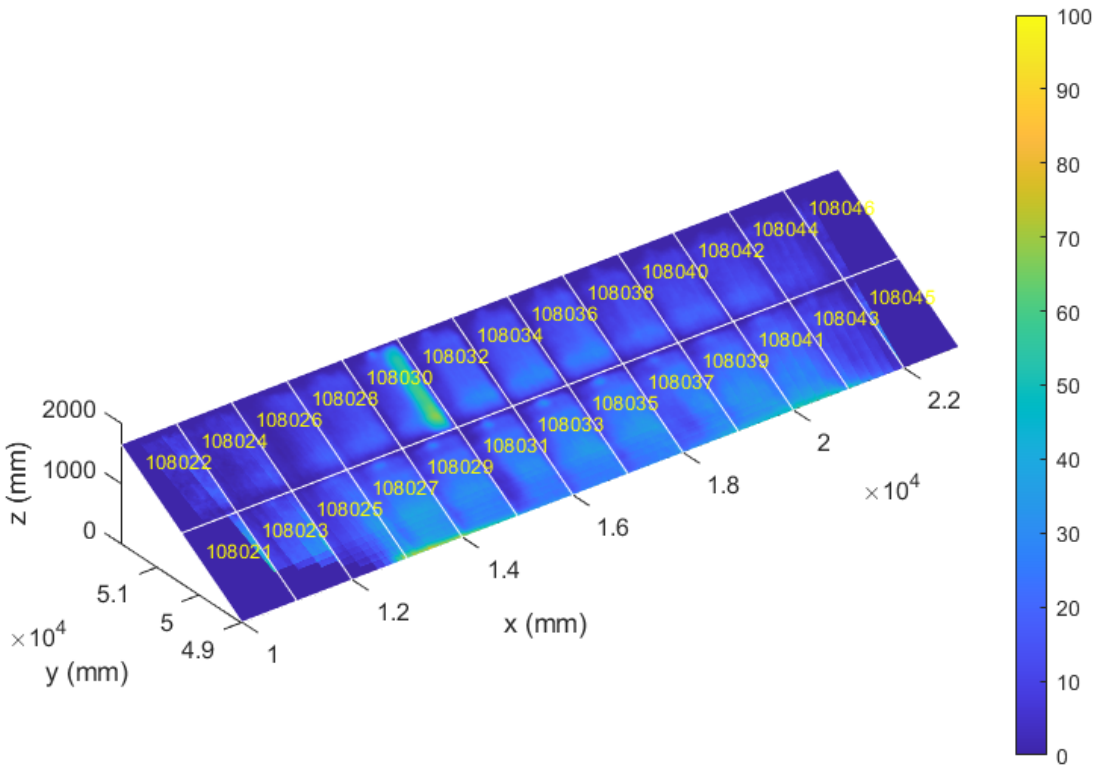

Figure 5.11: Overview of successful detected modules, starting with 108021 and ending with ID number 108046

Since the IR image has a lower resolution, not all detected IR orthoimages are usable for evaluation. The reason is shown in the following figure fig. 5.12.

From fig. 5.12 it can be observed that due to the lower resolution of the IR image and the resulting FOV, sometimes orthoimages that are transformed from RGB to IR are only partially displayed or not displayed at all. The sections that have been cut off are displayed with zeros in the intensity profile.

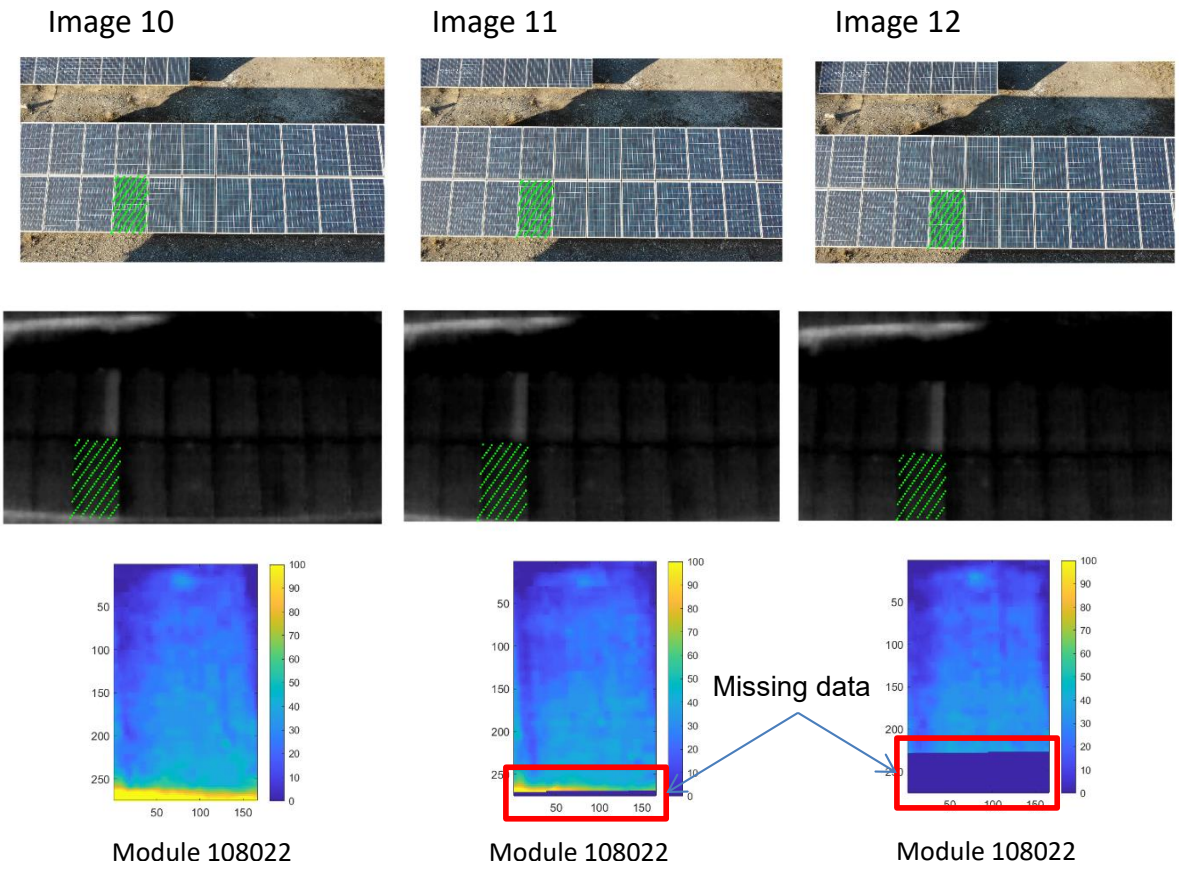

Figure 5.12: Partially generated IR orthoimages due to smaller FOV of the IR camera in comparison to the RGB camera. The sections that have been cut off are displayed with zeros in the intensity profile.

This circumstance leads to a distortion of the results of the resulting multiperspective IR orthoimages.

To avoid this problem, a filter function has been implemented, which filters out individual orthoimages where the proportion of existing 0 values exceeds 10 %.

After the successful implementation of the filter function, there are now far fewer modules available for further evaluation. At the same time, the measurement data generated is much more reliable, as they are no longer distorted by zero values due to partially cut modules.

In the following figure fig. 5.13 it can be observed that only 16 of the previously 26 detected modules provide usable data.

Based on these results, the average values of the individual multiperspective IR orthoimages can now be derived fig. 5.14.

In this diagram, the individual mean values and the associated standard deviation based on the

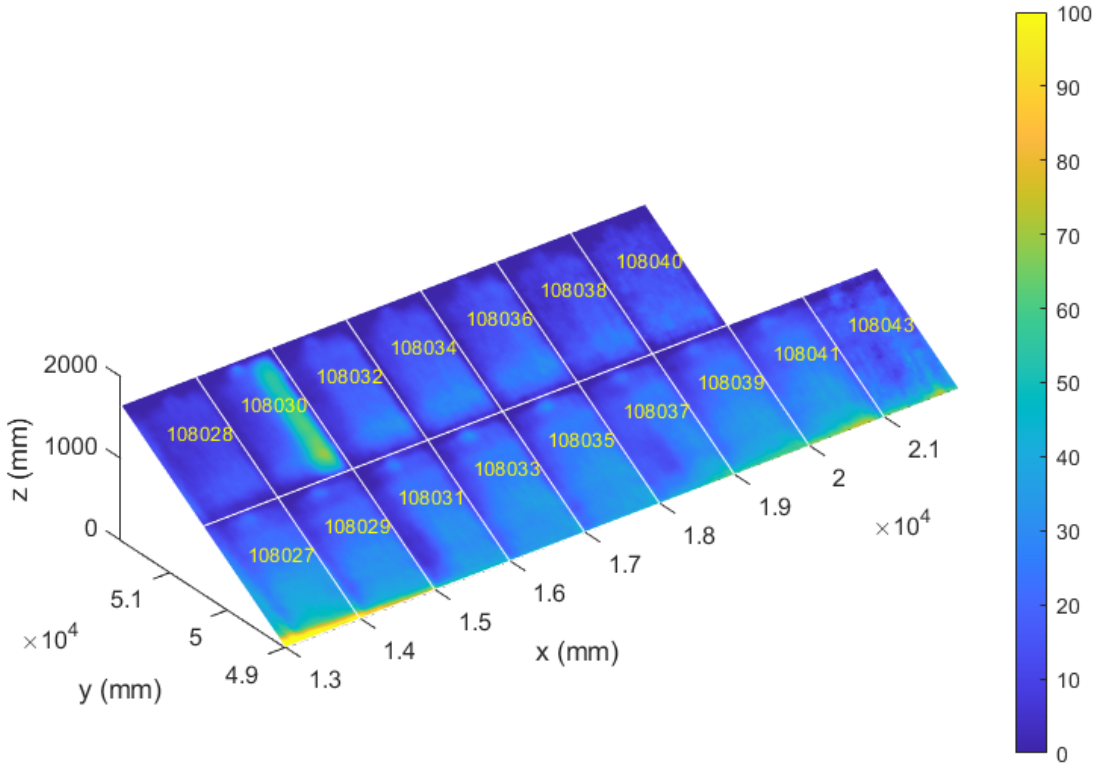

Figure 5.13: Overview of successful detected modules after filtering IR orthoimages with > 10 percent 0 values

mean values of the individual IR orthoimages were calculated and graphically displayed.

On closer inspection, it is immediately noticeable that the upper module string (red bars) has significantly lower average values $I_{upperString}$ = 11.93 ± 1.67 (n=6) of the intensity distribution than the lower module string $I_{lowerString}$ = 23.30 ± 1.98 (n=8). The intensity difference of the upper module string regards the lower string considering only the modules with homogeneous intensity distribution is $I_{lowerString} - I_{upperString} = \Delta I_{Diff}$ = 11.93 ± 2.82. This phenomenon has already been discussed in detail in section 5.1.

A comparison of the mean values of the upper string (red bars) shows that module no. 108030 has a significantly higher mean value $I_{mean_{108030}}$ = 21.95 than the modules in the same module string I_{mean} = 11.37 ± 1.67 (n=6). This results in a intensity difference of ΔI_{Diff} = 10.58 ± 1.67.

A closer inspection of the intensity profile of module 108030 (fig. 5.16, left) clearly shows that the cells in the right cell string have higher intensities than the surrounding cells.

According to IEC/TS 62446-3 the reason for this IR thermal pattern is, that one substring is operating in open circuit conditions due to a defective bypass diode. A loss of the connection of the bypass diode within module junction box or cell connector could be also the reason [6, 4].

Therefore, it can be concluded that module 108030 is a defective module for which a defect was

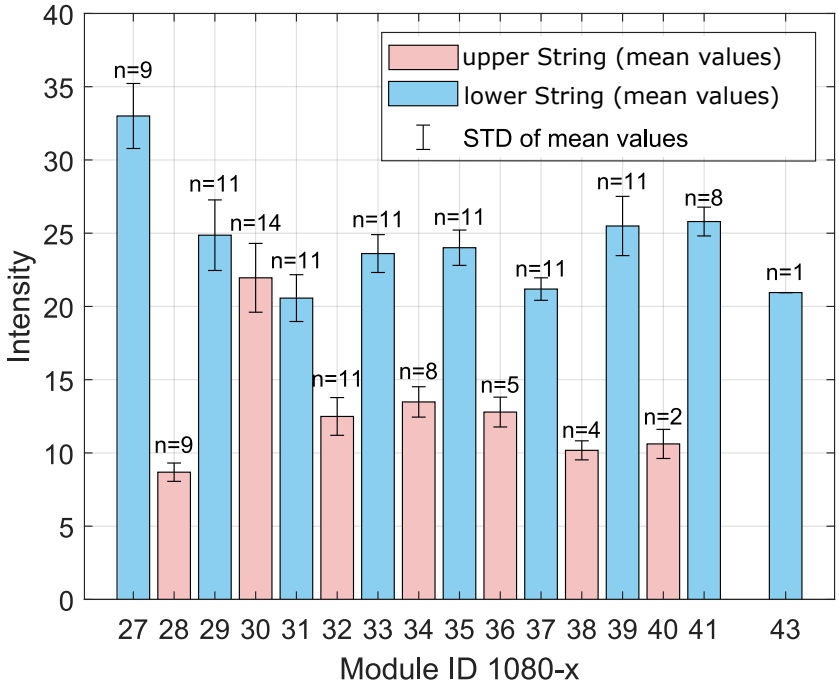

Figure 5.14: Average mean intensities of the individual multiperspective IR orthoimages, upper module-string illustrated by red bars and lower module-string illustrated by blue bars. The calculated STD_{mean} value is derived from the mean values of the individual orthoimages.

successfully detected.

In the lower module row fig. 5.14, there are higher average values than in the upper row. At this point, it is noticeable that module no. 108027 has a higher intensity value of $I_{mean_{108027}}$ = 33 compared to the other modules in the same row I_{mean} = 23.30 ± 1.98 (n=8) which results in a intensity difference of ΔI_{Diff} = 9.69 ± 1.98. On closer examination (fig. 5.16, right), the lower edge of this module shows high intensity values. This phenomenon was also discussed in section 5.1.

Unlike in module 108030, this is not a defect of the module but rather an image distortion due to reflection of sun rays at the aluminum edge of the PV module, although this is only an assumption and the actual reason has not yet been clarified. However, certainly, the increased intensities were not caused by module damage but rather by image processing.

In this case, there would be a false positive result regarding error detection. To avoid such errors it is therefore important to limit intensity values in which actual defects can occur. If the values are very high as in this case, one can then immediately conclude that it is an imaging error and not increased temperatures due to defects in the PV module.

As a possible solution, a filter function can be implemented, which filters out unrealistically high-intensity profiles. To calibrate this filter correctly, it is necessary to measure larger amounts of data and, ideally, absolute temperatures.

In addition to the standard deviations of the individual mean value of the individual orthoim-

ages, the standard deviations of the intensity values $STD_{intensity}$ of one multiperspective IR orthoimage can also be determined fig. 5.15.

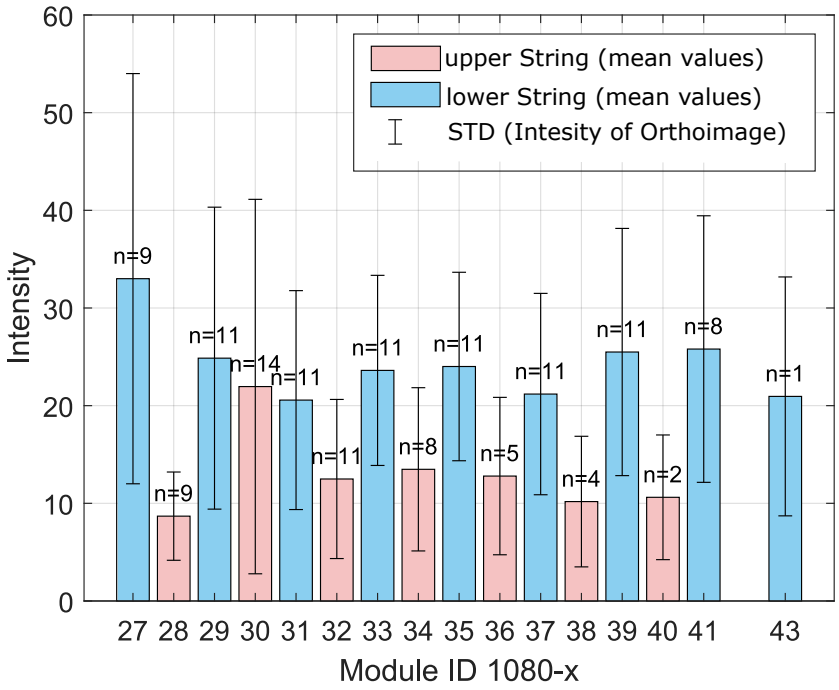

Figure 5.15: Average mean intensities of the individual multiperspective IR orthoimages, upper module-string illustrated by red bars and lower module-string illustrated by blue bars. The calculated $STD_{intensity}$ value is derived from the intensity values of the multiperspective IR orthoimage

In fig. 5.15, it can be seen that the $STD_{intensity}$ in the upper string of modules is significantly larger for the defective module no. 108030 than for the other modules in the same string.

The reason for this is the non-homogeneous distribution of the intensity values, due to the existing defect (fig. 5.16, right).

This information can be a further indication that the analyzed PV module is defective.

Another point to consider when evaluating is the following. As already presented in section 3.3, the lens curvature of the infrared camera causes so-called radial symmetric distortion. The radial symmetric distortion is especially apparent at the edges of the IR image.

The influence of this phenomenon is shown graphically in fig. 5.17. If examining the modules located at the boundary of the IR image, the module no. 108028, 108027, and 108043, one can see that the module edges are not parallel but diagonally in the image plane (fig. 5.17, bottom). To prevent this behavior, a radial-symmetric correction function should be established in addition to the normal transformation matrix.

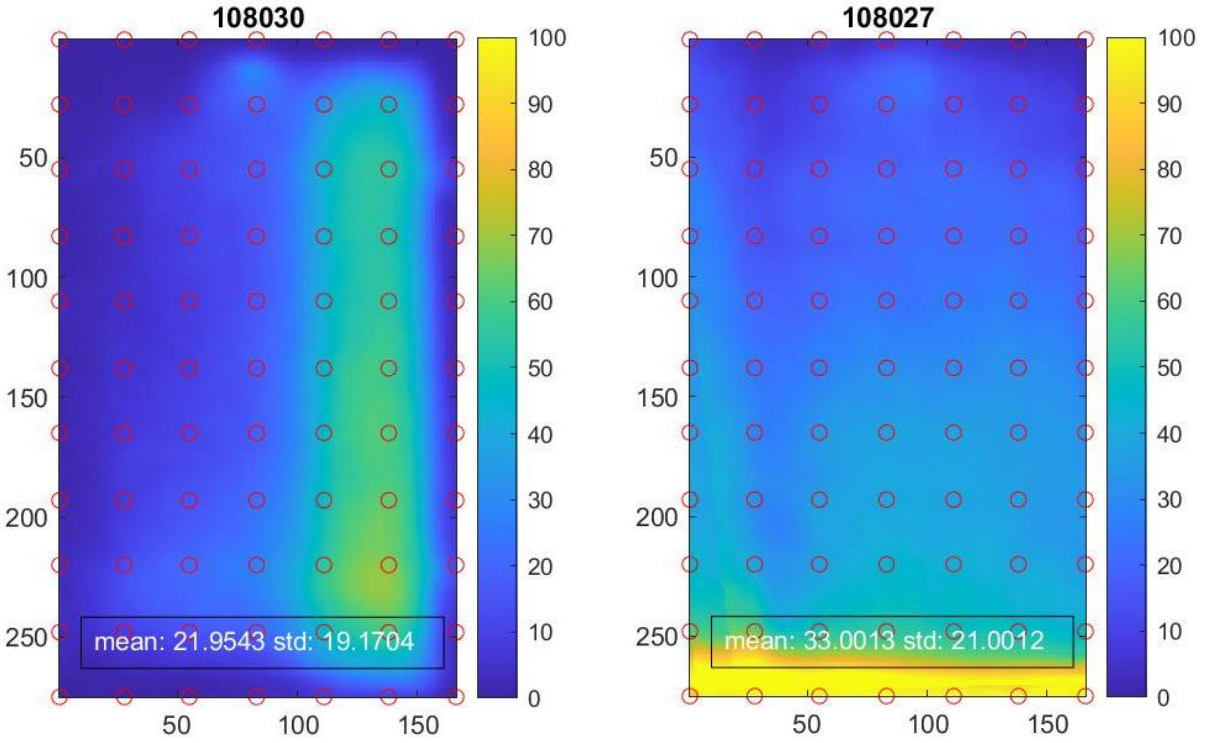

Figure 5.16: Defective Module 108030 (left) and Module 108027 (right) with overexposure at the bottom edge

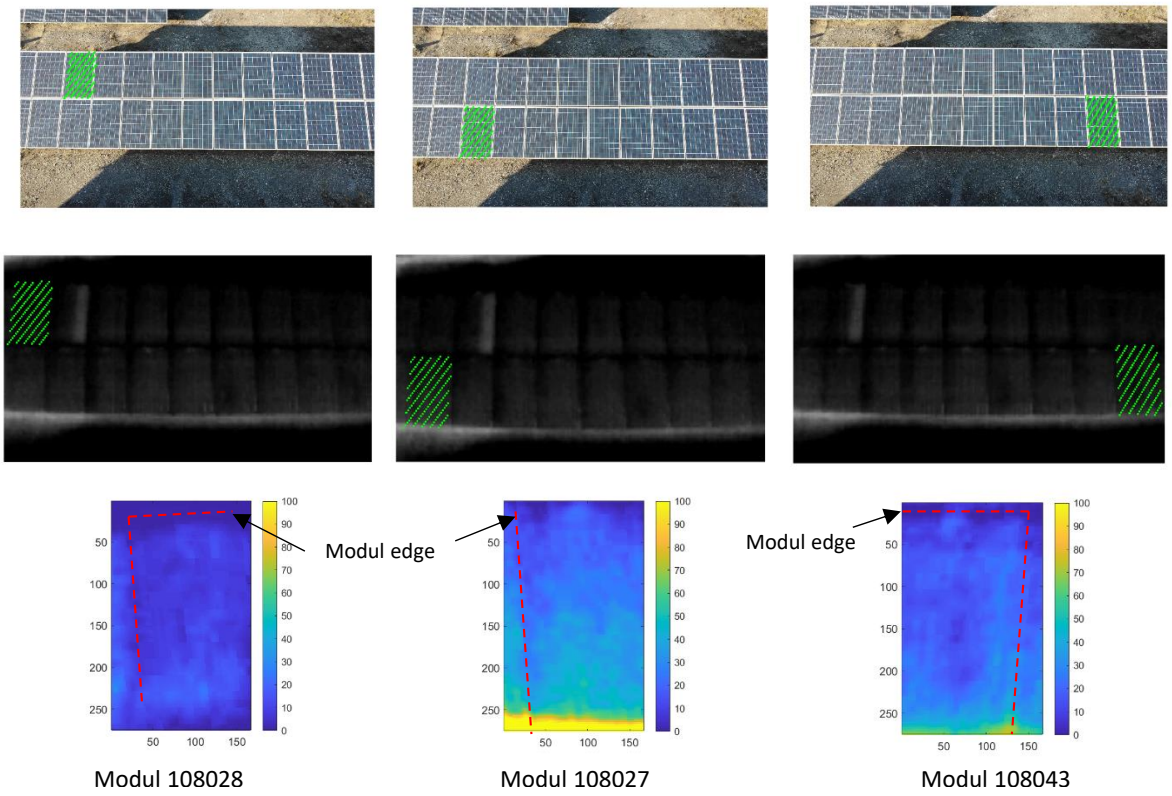

Figure 5.17: Modules no. 108028, 108027, and 108043, at the edges of the IR image are not parallel but diagonally due to radial-symmetric distortion

5.4.2 Defect detection on cell level

Besides, the individual modules can be examined at the cell level. This information can be used to classify specific defects based on certain thermal patterns, see subsection 2.4.2.

As in fig. 5.16, a fault type can be inferred from the existing thermographic pattern.

For better illustration, a 6 x 10 grid was placed into the orthoimages, which corresponds to the pattern of the cells in the module, see fig. 5.18.

If we take a closer look at module no. 108030 (left), it is noticeable that the module is not extracted 100 percent correctly. If a comparison is made between the original image (fig. 5.19, upper image) and the actual IR orthoimage (fig. 5.18, left), it can be seen that the cells with increased temperature should be located on the very right edge. Again, the main reason is the radial symmetric distortion as mentioned earlier. On the other hand, if we look at module 108036, it is much better extracted from the IR image, (fig. 5.18 , right).

Considering a single orthoimage where the module 108030 is located in the center of the camera, the right edge moves further to the right of the image frame (fig. 5.19, bottom).

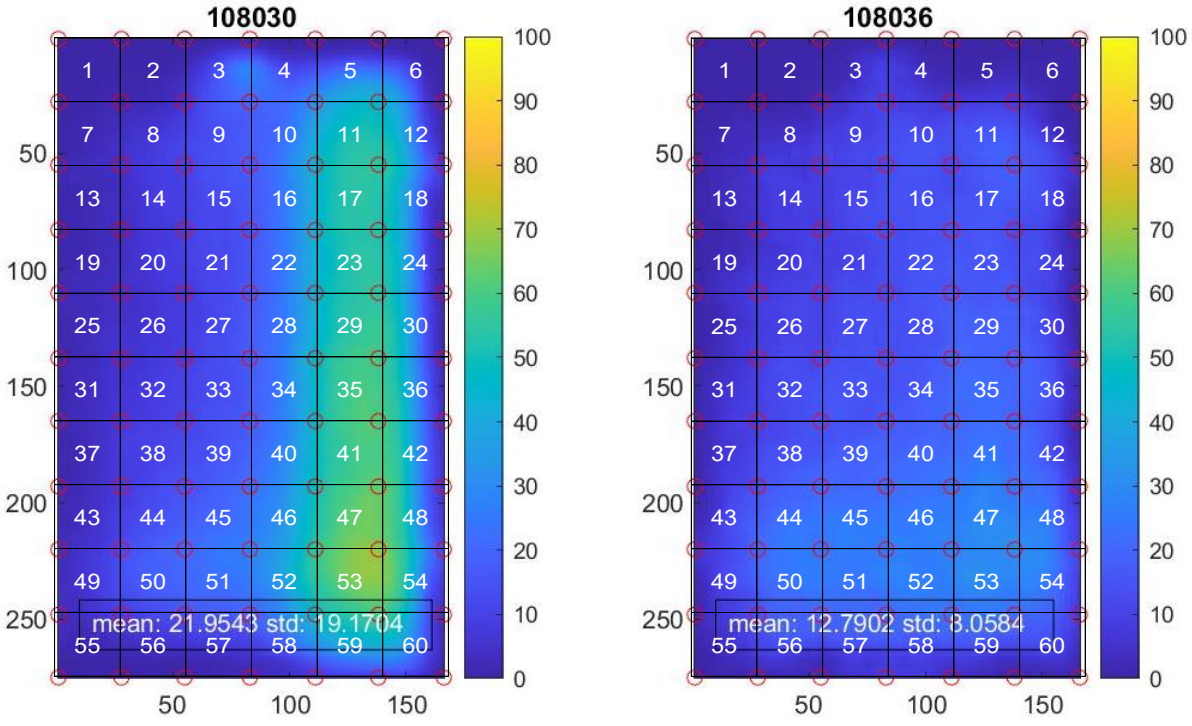

Figure 5.18: Module 108030 and 108036 with 6 x 10 grid representing the cell pattern

In figure fig. 5.20 the mean values of the intensities were plotted at the cell level. In total there are 60 cells. A closer look at the individual mean values shows that the mean values of the defective cell string are about 20 units higher than those of the normal cells.

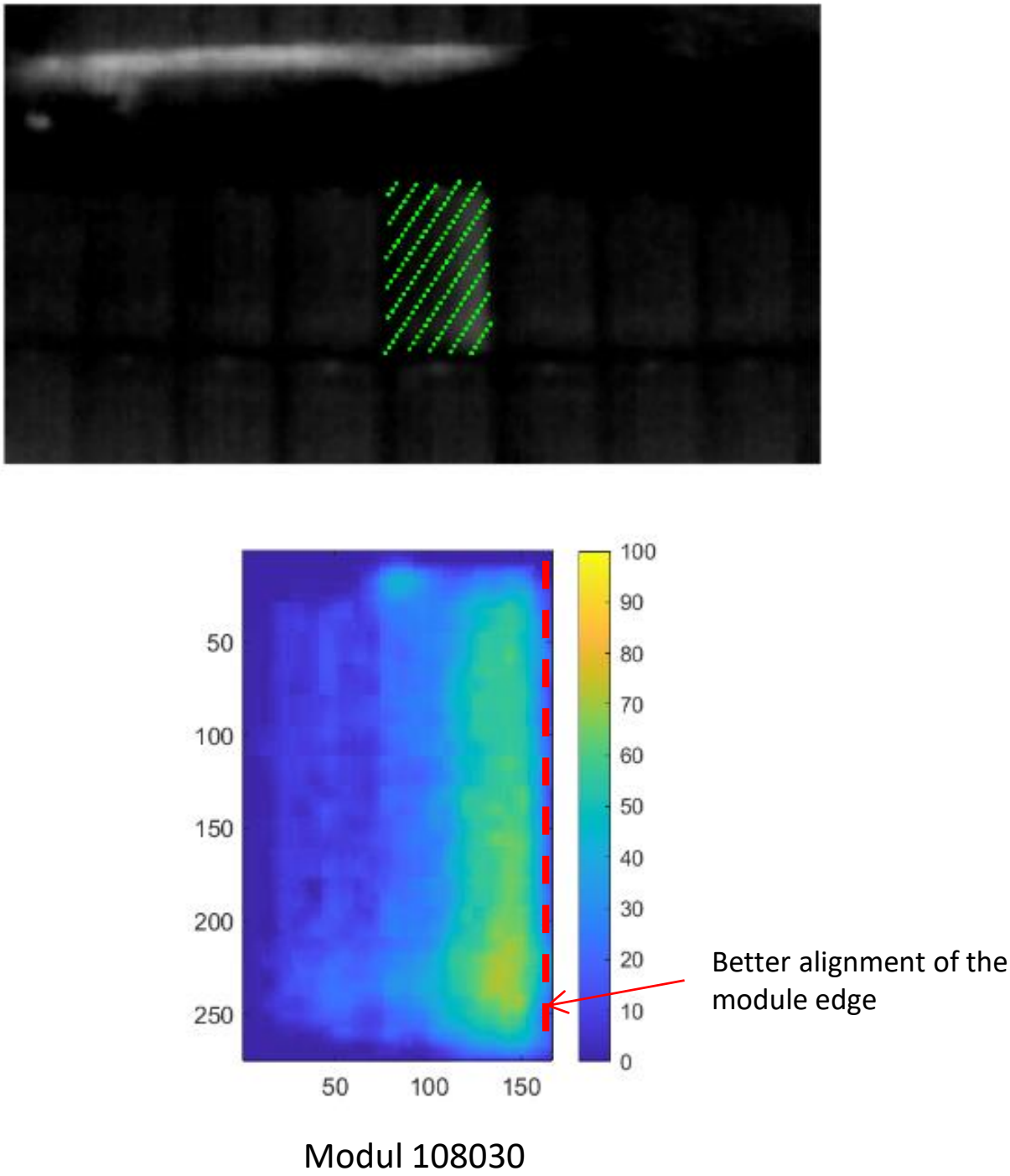

Figure 5.19: Orthoimage of Modul 108030 where the module is located in the center of the camera, the right edge of the module moves further to the right to the edge

The second diagram (below) shows the average values of the individual cells of module 108036, which are about the same order of magnitude as those of module 108030. This module shows a slight increase in temperature from left to right and from top to bottom.

Both diagrams show a linear increase of intensities from top to bottom, which was already discussed in section 5.1.

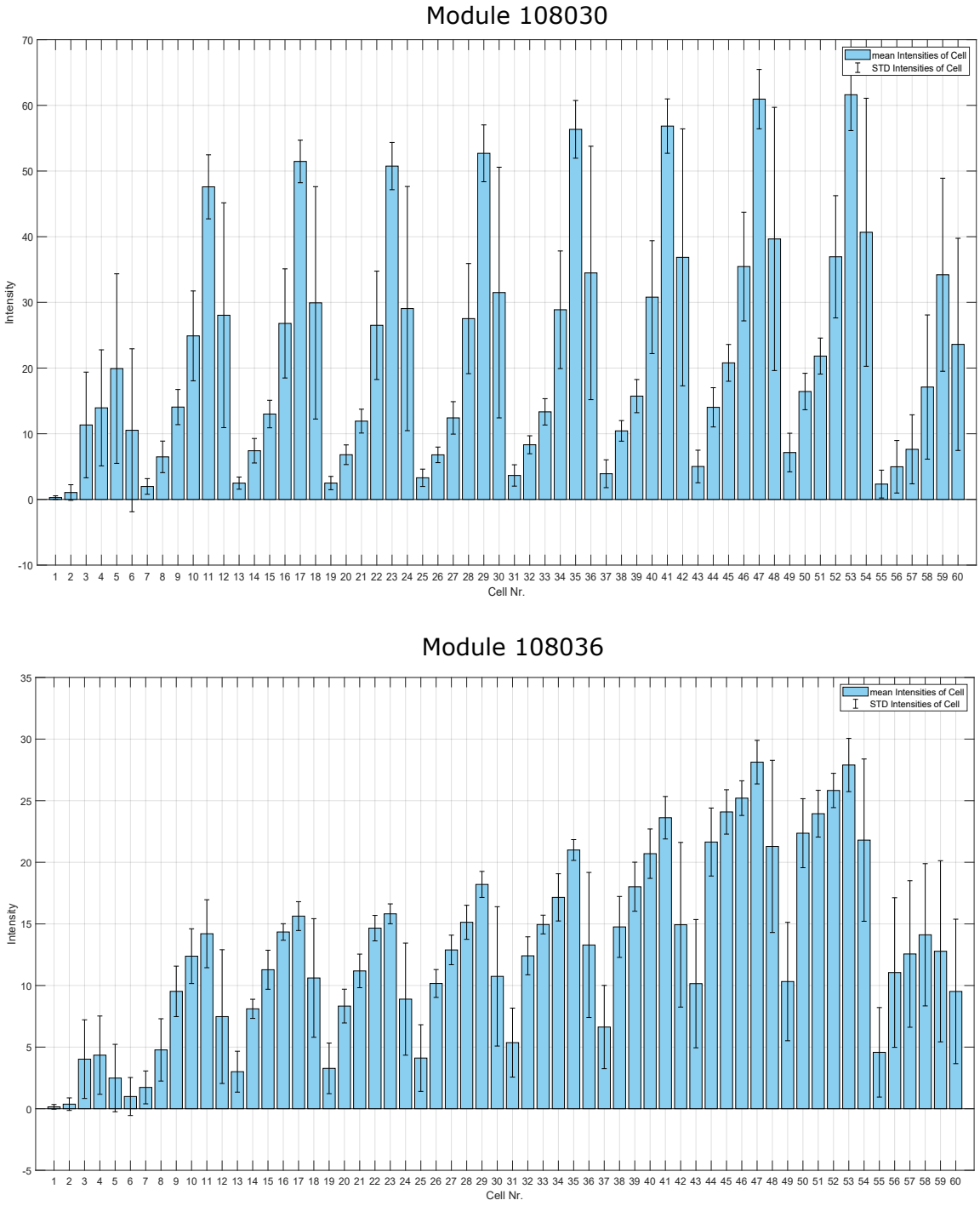

Figure 5.20: The mean values of the intensities were plotted at the cell level. The upper plot represents module 108030 and the lower plot represents module 108036.

At this point, suitable pattern recognition algorithms should be implemented, which, depending on the intensity magnitude and thermal pattern form, can assign corresponding fault types according to fig. 2.16.

6 Summary and outlook

A detailed analysis of the camera resolution has shown that the degree of detail depends on the flight altitude and the distance of the camera to the measured object. In the experimental dataset of the PV panels a distance of about 5.3 m allows to capture both module strings (upper and lower) in the camera image.

The calculated flight altitude results in a pixel resolution of 32.94 mm/pixel. Considering a size per cell of 165 x 165 mm, each cell can be displayed in a 5 x 5 pixel matrix by the given distance.

This resolution misses the required GSD of 30 $\pm$ 0.5 mm/pixel for a comprehensive inspection only by ΔGSD = 2.9 $\pm$ 0.5 mm/pixel. At the comprehensive level, accurate absolute temperature can be measured and meets the requirements by IEC TS 62446-3.

Since the IR camera used does not generate radiometric images, no absolute temperatures are recorded. Therefore, theoretically a resolution of 55 $\pm$ 0.5 mm/pixel would be sufficient, which would correspond to a distance to the measuring object of approximately 9m. This degree of resolution is classified as inspection type „standard“, which enables the successful detection of defective diodes and cells.

Finally, it can be concluded that the higher the resolution the larger the field of view and the more modules can be recorded at the same time. This means that the inspection time and the resolution of the IR camera are in constant relation to each other.

Considering the generated raw data of the PV system, it is noticeable that the upper modules have a significantly lower intensity than the lower modules. Several reasons for this effect are suggested, but none of them could be clearly verified with regard to cloud cover, wind speed and generator state of the respective module series. Therefore, further investigations should be carried out to clarify the exact relationship. The understanding is particularly important in order to be able to compare the different module strings with each other.

Furthermore, the QFly workflow could be automated to the extent that individual modules are correctly identified. Further issues have been identified and addressed regarding the QFly workflow. Among other aspects the synchronization of the time steps between RGB and IR camera with a mean time error of μ = 0.81e - 02s $\pm$ 0.49e - 02s could be implemented. With an average flight speed of 3 m/s a the average error is accordingly 24.3mm $\pm$ 14.7mm, while considering the resoultion of approx. 32.9 mm/pixel, therefore the absolute error is 4/3 of a pixel.

Moreover, a tool „TransMatrixTool“ was developed which allows to transform the orthoimages from the RGB images to the IR images. It has been concluded that the superposition of RGB

to IR orthoimages have an accuracy of 0.37 pixels as long as the targets are centered in the IR image. However, if the targets are farther away from the center, the maximum deviation will be greater. In the sample dataset a maximum average deviation of 3.99 pixel was measured. The reason for the increasing discrepancy is the radial-symmetric distortion and is caused by changes in refraction of the lens and is dependent on the current focus and the object distance. The implementation of a correction function that corrects radial-symmetric distortion should provide a significant improvement.

With regard to the defect detection in the PV system, a time range of 00:59:01 to 01:01:02 was extracted from the raw data. From this time span a total of 18 image pairs (IR/RGB) were extracted considering the minimum time difference. By means of the QFly post-processing algorithm a total of 26 modules could be successfully detected and mapped geographically. For each of the modules a multi perspective image consisting of several single orthoimages was generated.

It has been shown that some orthoimages are only partially extracted, which falsifies the measurement data. For this reason a filter function was established which filters out individual orthoimages which are not entirely extracted.

After re-running the QFly algorithm, only 16 of the previous 26 modules were used for further evaluation. From the 16 modules, a defective module (module no. 108030) could be identified by its thermal pattern. According to IEC/TS 62446-3 the reason for this IR thermal pattern is, that one substring of the module is operating in open circuit conditions due to a defective bypass diode. By closer inspection of the defective module it is noticeable that it has a significantly higher mean value $I_{mean_{108030}} = 21.95$ than the modules in the same module string $I_{mean} = 11.37 \pm 1.67$ (n=6). This results in a intensity difference of $\Delta I_{Diff} = 10.58 \pm 1.67$

In another module (module no. 108027) significantly higher intensity values of $I_{mean_{108027}} = 33$ compared to the other modules in the same row $I_{mean} = 23.30 \pm 1.98$ (n=8) which results in an intensity difference of $\Delta I_{Diff} = 9.69 \pm 1.98$. It is assumed that high values occur due to overexposure or sun reflection at the lower edge of the aluminum profile. Unlike in module 108030, this is not a defect of the module but rather an image distortion. At this point it is recommended to implement a filter function which allows to filter out unrealistically high-intensity profiles in order to avoid false positive results. At the same time, the implementation of a radial-symmetric correction function could lead to an improvement in this case, since this module is also located far outside the center of the image frame, and thus is not ideally cropped.The same problem exists with the modules no. 108028, 108027, and 108043, which are also located at the edge of the image and are therefore not cut out correctly. For this reason, the current analysis of the IR images is only limited to the middle modules, since the further away from the middle, the greater the deviation due to radial-symmetric disortion.

Another important aspect is that in this experiment, as already mentioned above, the modules in the lower string have higher intensity values than those in the upper string. The intensity difference of the upper module string regards the lower string considering only the modules with

homogeneous intensity distribution is $I_{lowerString} - I_{upperString} = \Delta I_{Diff} = 11.93 \pm 2.82$. One assumption is the non-orthogonal alignment of the IR camera to the module surface. Since the emission coefficient depends on the viewing angle to the measurement object, this could be the reason for the non-homogeneous intensity distribution and should be investigated further at this point.

Finally, the modules were analyzed at the cell level. At this point, the defect detection algorithms should be extended so that an automatic classification of the thermographic patterns to the respective defect type can take place. Furthermore, a larger amount of data with additional error types should be analyzed to further improve the error detection process.

Bibliography

[1] "Deutsches Zentrum für Luft- und Raumfahrt," Aug. 2020, page Version ID: 202802754. [Online]. Available: https://de.wikipedia.org/w/index.php?title=Deutsches_Zentrum_f%C3%BCr_Luft-_und_Raumfahrt&oldid=202802754

[2] T. Luhmann, *Nahbereichsphotogrammetrie*. Wichmann Verlag, 2000.

[3] "IEA-PVPS – IEA Photovoltaic Power Systems Programme TCP." [Online]. Available: https://iea-pvps.org/wp-content/uploads/2017/09/170515_IEA-PVPS-report_T13-09-2017_Internetversion_2.pdf

[4] J. A. Tsanakas, L. Ha, and C. Buerhop, "Faults and infrared thermographic diagnosis in operating c-Si photovoltaic modules: A review of research and future challenges," *Renewable and Sustainable Energy Reviews*, vol. 62, pp. 695–709, Sep. 2016. [Online]. Available: http://www.sciencedirect.com/science/article/pii/S1364032116301629

[5] Y. Zefri, A. ElKettani, I. Sebari, and S. Ait Lamallam, "Thermal infrared and visual inspection of photovoltaic installations by uav photogrammetry—application case: morocco," *Drones*, vol. 2, no. 4, p. 41, 2018.

[6] "IEC TS 62446-3:2017 | IEC Webstore." [Online]. Available: https://webstore.iec.ch/publication/28628

[7] G. Álvarez Tey, R. Jiménez-Castañeda, and J. Carpio, "Analysis of the configuration and the location of thermographic equipment for the inspection in photovoltaic systems," *Infrared Physics & Technology*, vol. 87, pp. 40–46, Dec. 2017. [Online]. Available: https://linkinghub.elsevier.com/retrieve/pii/S1350449517304437

[8] Z. Bayern eV, "Überprüfung der qualität von photovoltaik-modulen mittels infrarotaufnahmen," 2007.

[9] M. Aghaei, A. Dolara, S. Leva, and F. Grimaccia, "Image resolution and defects detection in pv inspection by unmanned technologies," in *2016 IEEE Power and Energy Society General Meeting (PESGM)*. IEEE, 2016, pp. 1–5.

[10] S. Gallardo-Saavedra, L. Hernández-Callejo, and O. Duque-Perez, "Technological review of the instrumentation used in aerial thermographic inspection of photovoltaic plants," *Renewable and Sustainable Energy Reviews*, vol. 93, pp. 566–579, 2018.

[11] K. Mertens, *Photovoltaik: Lehrbuch zu Grundlagen, Technologie und Praxis*, 4th ed. München: Carl Hanser Verlag GmbH & Co. KG, Aug. 2018. [Online]. Available: https://www.hanser-elibrary.com/doi/book/10.3139/9783446456174

[12] S. Beucker and K. Fichter, *Trends und Rahmenbedingungen für das Innovationssystem Farbstoffsolarzelle - Perspektive 2020.* Berlin: Borderstep Institut für Innovation und Nachhaltigkeit GmbH, 2007.

[13] "Photovoltaics Report - Fraunhofer ISE." [Online]. Available: https://www.ise.fraunhofer.de/de/veroeffentlichungen/studien/photovoltaics-report.html

[14] E. Rebhan, *Energiehandbuch: Gewinnung, Wandlung und Nutzung von Energie.* Springer-Verlag, 2013.

[15] I. J. Tsanakas and P. Botsaris, "On the detection of hot spots in operating photovoltaic arrays through thermal image analysis and a simulation model," *Materials Evaluation*, vol. 71, pp. 457–465, 04 2013.

[16] W. Herrmann, W. Wiesner, and W. Vaassen, "Hot-spot investigations on pv modules-new concepts for a test standard and consequences for module design with respect to bypass diodes," in *Conference Record of the Twenty Sixth IEEE Photovoltaic Specialists Conference-1997.* IEEE, 1997, pp. 1129–1132.

[17] M. Simon and E. L. Meyer, "Detection and analysis of hot-spot formation in solar cells," *Solar Energy Materials and Solar Cells*, vol. 94, no. 2, pp. 106–113, Feb. 2010. [Online]. Available: http://www.sciencedirect.com/science/article/pii/S0927024809003420

[18] O. Breitenstein, J. Bauer, and J. Rakotoniaina, "Material-induced shunts in multicrystalline silicon solar cells," *Semiconductors*, vol. 41, no. 4, pp. 440–443, 2007.

[19] J. Wohlgemuth and W. Herrmann, "Hot-spot tests for crystalline silicon modules," in *Conference Record of the Thirty-first IEEE Photovoltaic Specialists Conference, 2005.* IEEE, 2005, pp. 1062–1063.

[20] M. Köntges, S. Kurtz, C. Packard, U. Jahn, K. A. Berger, and K. Kato, *Performance and reliability of photovoltaic systems: subtask 3.2: Review of failures of photovoltaic modules: IEA PVPS task 13: external final report IEA-PVPS.* Sankt Ursen: International Energy Agency, Photovoltaic Power Systems Programme, 2014.

[21] J. A. Tsanakas, G. Vannier, A. Plissonnier, D. L. Ha, and F. Barruel, "Fault diagnosis and classification of large-scale photovoltaic plants through aerial orthophoto thermal mapping," in *Proceedings of the 31st European Photovoltaic Solar Energy Conference and Exhibition 2015*, 2015, pp. 1783–1788.

[22] S. Djordjevic, D. Parlevliet, and P. Jennings, "Detectable faults on recently installed solar modules in Western Australia," *Renewable Energy*, vol. 67, pp. 215–221, Jul. 2014. [Online]. Available: http://www.sciencedirect.com/science/article/pii/S0960148113006149

[23] D. C. Jordan and S. R. Kurtz, "Photovoltaic Degradation Rates—an Analytical Review," *Progress in Photovoltaics: Research and Applications*, vol. 21, no. 1, pp. 12–29, 2013. [Online]. Available: https://onlinelibrary.wiley.com/doi/abs/10.1002/pip.1182

[24] A. Peled and J. Appelbaum, "Minimizing the current mismatch resulting from different locations of solar cells within a pv module by proposing new interconnections," *Solar Energy*, vol. 135, pp. 840–847, 2016.

[25] E. Forniés, F. Naranjo, M. Mazo, and F. Ruiz, "The influence of mismatch of solar cells on relative power loss of photovoltaic modules," *Solar Energy*, vol. 97, pp. 39–47, 2013.

[26] M. Köntges, S. Kurtz, C. Packard, U. Jahn, K. Berger, K. Kato, T. Friesen, H. Liu, and M. Van Iseghem, "Performance and reliability of photovoltaic systems, subtask 3.2: review of failures of photovoltaic modules," *Report2014*, 2014.

[27] M. Köntges, S. Kajari-Schröder, and I. Kunze, "Crack statistic for wafer-based silicon solar cell modules in the field measured by uv fluorescence," *IEEE Journal of Photovoltaics*, vol. 3, no. 1, pp. 95–101, 2012.

[28] S. Meyer, S. Richter, S. Timmel, M. Gläser, M. Werner, S. Swatek, and C. Hagendorf, "Snail trails: root cause analysis and test procedures," *Energy Procedia*, vol. 38, pp. 498–505, 2013.

[29] P. B. Quater, F. Grimaccia, S. Leva, M. Mussetta, and M. Aghaei, "Light unmanned aerial vehicles (uavs) for cooperative inspection of pv plants," *IEEE Journal of Photovoltaics*, vol. 4, no. 4, pp. 1107–1113, 2014.

[30] C. Buerhop, D. Schlegel, M. Niess, C. Vodermayer, R. Weißmann, and C. Brabec, "Reliability of ir-imaging of pv-plants under operating conditions," *Solar Energy Materials and Solar Cells*, vol. 107, pp. 154–164, 2012.

[31] J. Muñoz, E. Lorenzo, F. Martínez-Moreno, L. Marroyo, and M. García, "An investigation into hot-spots in two large grid-connected pv plants," *Progress in Photovoltaics: Research and applications*, vol. 16, no. 8, pp. 693–701, 2008.

[32] K. Kato, "Pvressq!: a research activity on reliability of pv systems from an user's viewpoint in japan," in *Reliability of Photovoltaic Cells, Modules, Components, and Systems IV*, vol. 8112. International Society for Optics and Photonics, 2011, p. 81120K.

[33] C. Buerhop, D. Schlegel, C. Vodermayer, and M. Nieß, "Quality control of pv-modules in the field using infrared-thermography," in *26th European Photovoltaic Solar Energy Conference*, 2011, pp. 3894–3897.

[34] M. Köntges, S. Kurtz, C. Packard, U. Jahn, K. A. Berger, K. Kato, T. Friesen, H. Liu, M. Van Iseghem, J. Wohlgemuth *et al.*, "Review of failures of photovoltaic modules," 2014.

[35] M. Ebert, "Research group 'reliability of solar modules and systems'-r&d competencies," *unpublished paper*, 2015.

[36] J. Lopez-Garcia, A. Pozza, and T. Sample, "Long-term soiling of silicon pv modules in a moderate subtropical climate," *Solar Energy*, vol. 130, pp. 174–183, 2016.

[37] A. Sayyah, M. N. Horenstein, and M. K. Mazumder, "Energy yield loss caused by dust deposition on photovoltaic panels," *Solar Energy*, vol. 107, pp. 576–604, 2014.

[38] C. Schill, S. Brachmann, and M. Koehl, "Impact of soiling on iv-curves and efficiency of pv-modules," *Solar Energy*, vol. 112, pp. 259–262, 2015.

[39] M. Mani and R. Pillai, "Impact of dust on solar photovoltaic (pv) performance: Research status, challenges and recommendations," *Renewable and sustainable energy reviews*, vol. 14, no. 9, pp. 3124–3131, 2010.

[40] H. Pedersen, J. Strauss, and J. Selj, "Effect of soiling on photovoltaic modules in norway," *Energy Procedia*, vol. 92, pp. 585–589, 2016.

[41] M. Piliougine, J. Carretero, M. Sidrach-de Cardona, D. Montiel, and P. Sánchez-Friera, "Comparative analysis of the dust losses in photovoltaic modules with different cover glasses," in *Proceedings of 23rd European Solar Energy Conference*, vol. 2008, 2008, p. 2698e2700.

[42] M. Vumbugwa, J. Crozier McCleland, E. van Dyk, F. Vorster, and T. Serameng, "Effects of current mismatch due to uneven soiling on the performance of multi-crystalline silicon module strings," *Journal of Energy in Southern Africa*, vol. 31, no. 1, pp. 62–72, 2020.

[43] R. Prakash, *Infrared thermography*. BoD–Books on Demand, 2012.

[44] W. Minkina and S. Dudzik, *Infrared thermography: errors and uncertainties*. John Wiley & Sons, 2009.

[45] T. Williams, *Thermal imaging cameras: characteristics and performance*. CRC Press, 2009.

[46] "Lepton | FLIR Systems." [Online]. Available: https://www.flir.com/products/lepton/

[47] "ThermalCapture - Thermal Imaging Technology | Capture raw radiometric thermal data with drones." [Online]. Available: https://thermalcapture.com/wp-content/uploads/2019/08/pv-system-inspection-thermal-drones-07-15-19.pdf

[48] A. Coffin, "Introduction to Aerial Thermography: Comprehensive Aerial Inspection," Dec. 2019. [Online]. Available: https://raptormaps.com/introduction-to-aerial-thermography-comprehensive-aerial-inspection/

[49] ——, "Introduction to Aerial Thermography: Standard Aerial Inspection," Dec. 2019. [Online]. Available: https://raptormaps.com/introduction-to-aerial-thermography-standard-aerial-inspection/

[50] ——, "Introduction to Aerial Thermography: Overview Aerial Inspection," Dec. 2019. [Online]. Available: https://raptormaps.com/introduction-to-aerial-thermography-overview-aerial-inspection/

[51] I. f. S. i. DLR, "DLR - Institut für Solarforschung - QFly - Qualitätsüberprüfung ganzer Solarfelder aus der Luft." [Online]. Available: https://www.dlr.de/sf/desktopdefault.aspx/tabid-10228/17490_read-44857/

[52] P. C. Prahl, "Airborne measurement of the optical performance of parabolic trough solar fields," Technischen Hochschule Aachen, 2018.

[53] S. Erkner, "JPG, JPEG - was ist das?" IT + Medien GmbH, D-15537,. [Online]. Available: http://www.digitalfotografie.de/jpg-format/02-was-ist-jpg-jpeg

[54] A. F. Habib, E.-M. Kim, and C.-J. Kim, "New methodologies for true orthophoto generation," *Photogrammetric Engineering & Remote Sensing*, vol. 73, no. 1, pp. 25–36, 2007.

[55] "FLIR DELTA: What Can I See With My Thermal Drone?" [Online]. Available: https://www.flir.com/news-center/public-safety/flir-delta-what-can-i-see-with-my-thermal-drone/

[56] "FOV calculator." [Online]. Available: https://www.drone-thermal-camera.com/support/fov-calculator/

[57] "Online FoV Calculators." [Online]. Available: https://flir.custhelp.com/app/answers/detail/a_id/920/~/online-fov-calculators

[58] "Punkt-Pyrometer und Wärmebildkameras im Vergleich." [Online]. Available: https://www.flir.de/discover/rd-science/temperature-guns-versus-thermal-imaging-technology/

[59] "MATLAB Documentation." [Online]. Available: https://www.mathworks.com/help/matlab/

[60] B. Jaeckel, "Outdoor non-destructive infrared thermography of photovoltaic modules and plants for," in *32nd European Photovoltaic Solar Energy Conference and Exhibition*, 2016.

[61] G. Álvarez-Tey, R. Jiménez-Castañeda, and J. Carpio, "Analysis of the configuration and the location of thermographic equipment for the inspection in photovoltaic systems," *Infrared Physics & Technology*, vol. 87, pp. 40–46, 2017.

[62] "Thermal Imaging, Night Vision and Infrared Camera Systems | FLIR Systems." [Online]. Available: https://www.flir.com/globalassets/imported-assets/document/flir-lepton-engineering-datasheet.pdf

[63] "SubRip," Aug. 2020, page Version ID: 971741138. [Online]. Available: https://en.wikipedia.org/w/index.php?title=SubRip&oldid=971741138

[64] "Ba online | Home." [Online]. Available: https://www.ba-online.info/files/b20381zsh_flir.pdf

[65] "Emissionsgrad-Tabelle bei thermografie-xtra.de." [Online]. Available: https://www.thermografie-xtra.de/tipps-tricks/emissionsgrad-tabelle

[66] M. Mittag, C. Kutter, S. Hoffmann, P. Romer, A. J. Beinert, and T. Zech, "Electrical and thermal modeling of junction boxes," *33rd EUPVSEC, Amsterdam*, pp. 1501–1506, 2017.

A Task definition

FRIEDRICH-ALEXANDER UNIVERSITÄT ERLANGEN-NÜRNBERG
TECHNISCHE FAKULTÄT

Photonische Technologien

Feasibility study on the automatic detection of faults in photovoltaic plants with unmanned aerial vehicles using low resolution thermographic cameras

Master thesis no.:	2020/012
Student:	Vladimir Harwardt
Matriculation no.:	22298714
Course of studies:	International Production Engineering and Management
Supervisor:	Prof. Dr.-Ing. Michael Schmidt, Kerstin Schaumberger, M.Sc.

Definition of tasks:

Due to the growing trend in alternative energy production, an ever increasing number of photovoltaic (PV) systems are being installed worldwide. To ensure their efficient operation, they must be inspected and maintained regularly. Since traditional inspection methods such as electrical tests are time-consuming and costly, new methods are being developed.

A promising inspection method is the so-called inspection by using Unmanned Aerial Vehicles (UAVs) with dual camera systems (RGB and infrared). The inspection of PV modules using thermographic cameras has proven to be a suitable method for assessing the performance and condition of individual PV modules. The use of this technology offers a faster, autonomous and cost-effective inspection of large photovoltaic plants.

Although there is a trend towards higher resolutions and more expensive camera systems, this thesis aims to conduct a feasibility study for the automatic inspection of PV systems using low-cost, commercially available drones with lower camera resolution. The advantages are a high availability, easy handling, a flexible applicability and a huge price advantage compared to the expensive industrial drones.

The significantly lower camera resolution is a challenge in the detectability of defects by means of data accuracy. The aim of this study is thus to assess whether reliable statements about the quality and state of individual PV modules can be made employing thermography with low resolution camera systems. For this purpose, thermographic images are generated during the inspection process and subsequently verified by an automated algorithm.

For conducting this thesis the following is available:

- Dual camera system consumer drone (RGB and infrared)
- Photovoltaic test environment for data generation
- Qfly postprocessing algorithm

Start date: 01.04.2020

Due date: 01.10.2020

(Prof. Michael Schmidt)

Date of contribution:

The FAU acquires a free of charge right of use on the thesis mentioned above for all known and unknown kinds and without limitations regarding the content, duration and location. The right of use contains particularly the right to use the mentioned work in every possible way (e.g. in print, in digital form, in internet presentations, publications, etc.) as well as in – e.g. by means of digital image editing – modified form and to make it accessible to the public.

I acknowledge receipt of the task and agree with the arrangement on the right of use.

Erlangen, 01.04.2020

(student)

The journey of a thousand miles begins with one step.

LAO-TZU